III-V Quantum Structured Infrared Photodetectors Directly Grown on Silicon

Daqian Guo

A thesis submitted to University College London for the degree of

Doctor of Philosophy (PhD)

Department of Electrical and Electronic Engineering

University College London

October 2020

Declaration

I, Daqian Guo, confirm that the work presented in this thesis is my own. Where information has been derived from other sources, I confirm that this has been indicated in the thesis.

To my family

Abstract

Direct growth of III-V infrared photodetectors on silicon substrates is a promising solution for realising low-cost and large-format infrared focal plane arrays. However, this heteroepitaxial growth technique will generate various defects due to the dissimilarities between III-V materials and Si. These defects can severely damage the performance of a detector.

In this thesis, different III-V quantum structured infrared photodetectors directly grown on Si are investigated to understand how different structures react to the defects. The experimental chapters begin with reporting an InGaAs/GaAs quantum dot infrared photodetector (QDIP) on Si. By utilising a Si substrate with a high degree of offcut along with dislocation filter layers, antiphase domains have been eliminated and the threading dislocation density has been reduced by $\sim$4 orders of magnitude. The QDIP shows a dual-band photoresponse at 80 K.

To reduce the noise, a sub-monolayer QD quantum cascade photodetector on Si was designed. This structure has led to a distinct reduction of dark current and noise, achieving a high operating temperature of 160 K.

To further boost the quantum efficiency of infrared photodetectors on Si, InAs/GaSb type-II superlattice (T2SL) photodetectors were also studied in this thesis. Generally, T2SL photodiode structures are more sensitive to material defects than QDs. Moreover, the surface leakage current contributes to a high level of dark current. InAs/GaSb T2SL photodiodes and barrier detectors have been grown on GaAs and Si substrates. Trans-

mission electron microscopy and X-ray diffraction results confirm that the strain energy has been released at the heteroepitaxy interface and the threading dislocation density has been reduced by $\sim$3 orders of magnitude. The bulk dark current has been reduced by implementing an nBp barrier design. As a result, a T2SL nBp detector on GaAs with surface passivation has been shown to be capable of operating at 190 K without external bias. The work described in this thesis shows that there is great potential to improve the detector performance by using novel detector designs.

Future work should focus on structure optimisation, as well as material quality improvements, in order to achieve both low dark current and high quantum efficiency. High-operating temperature detectors on Si can be attempted to further explore the potential of III-V quantum structured infrared photodetectors. Specific recommendations are made for candidate structures. In order to be compatible with the mainstream Si micro-electronics industry, fabrication on (001) Si substrates will be required. Research towards this objective is therefore also proposed.

Impact Statement

Detecting and sensing infrared radiation is demanded in many activities, such as industrial production control, chemical analysis, clinical diagnosis, environmental monitoring, defence and night vision. Developing small-size, low-cost and low power consumption infrared detectors will stimulate the more extensive use of infrared detection technologies. Direct growth of III-V infrared photodetectors on Si substrates can provide high-performance and low-cost infrared photodetectors, assuming that the problems associated with the material defects can be effectively resolved or relieved. This research project aims to have a significant impact both inside and outside academia by demonstrating III-V quantum structured infrared photodetectors on Si substrates with performance which is competitive to III-V detectors on native substrates.

This thesis will have an impact in the infrared community by introducing new strategies and thoughts to boost the performance of infrared photodetectors on Si. Motivated by the potential economic and technological benefits of Si substrates, heteroepitaxy growth of III-V or II-VI infrared photodetectors on Si has been explored for several decades. Performance has improved as a result of optimisation of buffer layers and the resulting reduction in defects. However, previous efforts have rarely focused on investigating different detector structures on Si and how different structures withstand the defects. This thesis takes account of the detector structural design rather than focusing solely on the material quality. We have published eight peer-reviewed journal papers to discuss the performance of quantum structured infrared photodetectors on non-native substrates. In

addition, this thesis discusses the III-V buffer technologies for improving the material quality. It is hoped that the results presented here will encourage the future development of III-V infrared detectors grown directly on silicon, as well as other III-V devices on Si.

The potential economic impact of this project is to lower the economic barrier of using infrared photodetectors for civil applications. Small and cost-efficient infrared systems provide a technology platform for developing many applications. For instance, portable self-diagnostic infrared detection systems can be implemented based on cheap detector systems for diagnosing many kinds of disease, such as skin cancer. Moreover, research in infrared detectors with high operating temperature, e.g. room temperature or with thermoelectric cooling, can offer a further reduction in operational cost and in the dimensions of the infrared sensing system. It would be expected that the outcomes of this project will encourage the start-up of spin-off companies and stimulate the economy of scale for infrared systems.

Overall, this research project aims to address the problems related to the technologies that are currently available and demonstrate the potential to offer compact, cost-efficient infrared detection technologies to a wide range of communities.

Acknowledgements

I would like to express my sincere gratitude to my supervisor, Dr. Jiang Wu, for his support, encouragement and guidance throughout this project. I am grateful for the opportunities that he has given me. My gratitude goes to Prof. Mike Wale, who supervised me for the past year. His expertise expands my knowledge and vision. Without Jiang and Mike's help and insights, competing this thesis would not be possible. I feel so lucky that I have met them. I also would like to express thanks to my secondary supervisor, Prof. Alwyn Seeds, for his guidance.

Many thanks to all the previous and present members of the UCL MBE group for their help and friendships. Thanks to Prof. Huiyun Liu for gathering us as a team. Thanks to Dr. Siming Chen for sharing his knowledge of III-V devices and device fabrication with me. Thanks to Dr. Mingchu Tang, Dr. Dongyoung Kim and Dr. Hao Xu for training me in material characterisation and device fabrication equipment. Special thanks to Dr. Mengya Liao for all the things she did for me. I really appreciate her making my life easier and happier.

My acknowledgement also goes to our collaborators. Thanks to Prof. Baile Chen, Dr. Zhuo Deng, Mr Jian Huang, Mr Wei Chen and Mr Ningtao Zhang at ShanghaiTech University for their contributions to this project. Thanks to Baile for arranging my visit to ShanghaiTech University. Thanks to Prof. Gregory Salamo, Dr. Yuriy Mazur and their colleagues at the University of Arkansas for their work in transmission electron microscopy and Photoluminescence characterisations. Thanks to Prof. William Masselink

and Dr. Mykhaylo Semtsiv at Humboldt University of Berlin for their work on device characterisation.

Finally, I would like to express my thanks and love to my parents and sister. Thank you for believing in me and for your unconditional support. I appreciate everything you did, and I hope I make you proud.

Table of Contents

Abstract **I**

Impact Statement **III**

Acknowledgements **V**

List of Figures **XI**

List of Tables **XVII**

List of Abbreviations **XVIII**

List of Publications **XX**

Chapter 1: Thesis Introduction **1**

1.1 Background 1

1.2 Motivations 5

1.3 Objective 8

1.4 Thesis Outline 9

References 11

Chapter 2: Introduction to Direct Growth of III-V Quantum Structured Infrared Photodetectors on Si substrates **16**

2.1 Basic Principles of Infrared Detectors 16

2.2 III-V Quantum Structured Infrared Photodetector 18

2.2.1 Quantum Dot Infrared Photodetector 18

2.2.2 Quantum Cascade Detector 22

2.2.3 InAs/GaSb T2SL Photodetector . . . 25
2.3 Self-assembled Quantum Dot Fabrication Method . . . 31
2.3.1 Molecular Beam Epitaxy System . . . 31
2.3.2 Self-assembled QDs via Stranski-Krastanov Growth Mode . . . 32
2.3.3 QDs Fabrication with Sub-monolayer Deposition . . . 33
2.4 Direct Growth III-V Virtual Substrate on Si at UCL MBE Group . . . 34
2.4.1 Antiphase Domain Suppression . . . 34
2.4.2 Threading Dislocation Reduction . . . 35
2.4.3 Interfacial Misfit Growth Technique . . . 37
2.5 Chapter Summary . . . 38
2.6 Contribution Statement . . . 38
References . . . 38
Chapter 3: Experimental Methods 52
3.1 Material Characterisations . . . 52
3.1.1 Photoluminescence . . . 52
3.1.2 X-ray Diffraction . . . 54
3.1.3 Transmission Electron Microscope . . . 56
3.2 Device Fabrication . . . 57
3.2.1 Overall Fabrication Flow . . . 57
3.2.2 Cleaning . . . 57
3.2.3 Photolithography . . . 57
3.2.4 Wet Etching . . . 59
3.2.5 Surface Passivation . . . 60
3.2.6 Metallisation and Lift-off . . . 61
3.3 Device Characterisations . . . 61
3.3.1 Dark Current . . . 61
3.3.2 Relative Response . . . 62

3.3.3 Responsivity 63
References 65
Chapter 4: Direct Growth of $In_{0.5}Ga_{0.5}As$/GaAs Quantum Dot Infrared Photodetectors on Si Substrates **67**
4.1 Introduction 67
4.2 Material Growth and Device Fabrication 68
4.3 Material Characterisations 70
4.4 Device Characterisation 75
4.4.1 Dark Current 75
4.4.2 Photoresponse 78
4.5 Conclusion 82
4.6 Contribution Statement 83
References 83
Chapter 5: Sub-monolayer Quantum Dot Quantum Cascade Infrared Photodetectors on GaAs and Si substrates **88**
5.1 Introduction 88
5.2 Material Growth and Device Fabrication 89
5.3 Material Characterisations 92
5.4 Device Characterisations 94
5.5 Conclusion 102
5.6 Contribution Statement 102
References 102
Chapter 6: InAs/GaSb T2SL Detectors on Si and GaAs Substrates **105**
6.1 Introduction 105
6.2 InAs/GaSb T2SL Photodiode on Si Substrate 107
6.3 InAs/GaSb T2SL nBp Barrier Detector on GaAs 111
6.4 nBp Barrier Detector Device Characterisation 115

6.4.1 Dark Current . . . 115
6.4.2 Photoresponse and Detectivity . . . 117
6.5 Conclusion . . . 121
6.6 Contribution Statement . . . 122
References . . . 122
Chapter 7: Summary and Future Work **125**
7.1 Summary . . . 125
7.2 Future Work . . . 129
7.2.1 Surface Plasmons . . . 129
7.2.2 nBp Barrier Detector Growth and Simulation Optimisations . . . 129
7.2.3 Ga-free T2SL Barrier Detectors . . . 130
7.2.4 CMOS Compatible Si (001) Substrates . . . 130
References . . . 131

List of Figures

1.1 Overview of the thesis motivations and objectives. 9

2.1 (a) Generation of photoexcited electrons by (1) B-B, (2) B-QB and (3) B-C transitions. (b) QDIPs dark current generation mechanisms (4) thermionic emission, (5) field assisted tunnelling or phonon assisted tunnelling and (6) defect assisted tunnelling. E_C is the conduction band edge of the barrier material. 20

2.2 Schematic conduction band diagram of the QCD and the cascade transport [40]. Electron intersubband transition occurs in the absorber region after exposure to IR. The photoexcited electron can tunnel through the barrier into the next QW by releasing an LO phonon. By repeating the tunnelling process for several times, the electron cascade over the cascade stages resulting in measurable photocurrent. λ_p is the peak absorption wavelength. 23

2.3 Illustration of the T2SL effective mini bands [50]. CB, HH and LH represent the effective conduction band, effective heavy hole band and effective light hole band. E_c and E_V the are conduction band edge and valence band edge, respectively. The colour boxes are the forbidden bands of GaSb (blue) and InAs (green). The optical excitation energy is the energy separation between CB and HH. 26

2.4 Schematic of dark current generation mechanisms of the homojunction photodiode [54]. p+ and n- represent heavy p doping and light n doping, respectively. E_C, E_F and E_V are the conduction band edge, thermal equilibrium Fermi level and Valence band edge, respectively. SRH and TAT represent the SRH and trap assisted tunnelling processes, respectively. The band-to-band tunnelling process and the Auger generation processes are not included. 27
2.5 Schematics of (a) nBn unipolar barrier detector [73] and (b) nBp detector with hole blocking barrier [75]. The superscripts "+" and "-" stand for high doping density and low doping density, respectively; E_C, E_F and E_V are the conduction band edge, Fermi level and valence band edge, respectively. SCR indicates the of space charge region; V_{bias} is the external bias voltage. 30
2.6 Schematic diagram of an MBE growth Chamber. 32
2.7 (a) Cross-sectional view of the high resolution transmission electron microscopy image of a S-K QD and (b) atomic force microscopy image of the S-K QDs. 33
2.8 Schematic cross-sectional view of (a) GaAs on monoatomic stepped Si (001) with APDs and (b) GaAs on double atomic stepped Si (001) without APDs. The dotted red lines and solid red lines represent the GaAs/Si interfaces and the antiphase boundaries, respectively. 34
2.9 Schematics of (a) High temperature growth nucleation layer and (b) low temperature growth nucleation layer [101]. 36

3.1 Schematics of the radiative emission processes. 53
3.2 Illustration of PL experimental setup. 54

3.3 Illustrations of (a) Bragg's law and (b) the basic components of an X-ray diffractometer configuration. ω is the angle between the incident beam and sample surface. 55
3.4 The processes for fabricating a single-pixel infrared detector. (1) Exposure, (2) developing, (3) etching, (4) surface passivation (optional), (5) exposure and developing (optional), (6) bi-layer photoresist coating, (7) exposure and developing, (8) metal deposition and (9) lift-off. In this thesis, steps (4) and (5) are not applied to the GaAs based detector, since the surface current is negligible in comparison with the bulk current. In (6)–(9) we assume that the top and bottom contact metals are the same. . 58
3.5 Schematic diagram of dark current measurement setup. 62
3.6 Schematic diagram of measuring the photoresponse using an FTIR spectrometer [18]. 63
3.7 Illustration of the experimental setup for calibrating detector responsivity using a blackbody radiator [18]. 64

4.1 Schemtic of the InGaAs QDIP on Si substrate. LT = Low Temperature. . 70
4.2 Cross-sectional TEM images of (a) the III-V buffer region and (b) the QD region. 71
4.3 Statistics of the base width of the InGaAs QDs measured from the cross-sectional TEM image, Figure 4.2 (b). A total number of 84 QDs were counted. 72
4.4 Gaussian fittings of the InGaAs QDIP PL spectra with laser power density (a) ($3.7 \times 10{-}4$ $\mathrm{W/cm^2}$ (b) 29 $\mathrm{W/cm^2}$ and (c) A comparison of the PL spectra measured with laser power densities 29 $\mathrm{W/cm^2}$ and 5000 $\mathrm{W/cm^2}$. 73

4.5 (a) Time-resolved PL decay measured at 10 K for the emission wavelengths $\sim$ 1.42 eV, 1.31 eV, 1.28 eV and 1.22 eV corresponding to the wetting layer emission, excited state emission, group 3 ground state emission and group 1 ground state emission, resepectively. (b) PL decay time for all measured emission energies with reference to the continuous wave PL signal measured at 10 K with laser power dneisty 5000 $\mathrm{W/cm^{-2}}$. . . . 75
4.6 Temperature-dependent dark current-voltage measurement for the QDIP with a diameter of 1000 μm. 77
4.7 Natural logarithm of dark current density measured at +0.1 V as a function of reciprocal temperature (1/T). 78
4.8 Photoresponse spectra measured at 80 K with different bias voltages. . . . 79
4.9 Voltage-dependent photoresponse spectra measured at 80 K with different positive bias voltages from 0.05 V to 1 V.[1] 80
4.10 Voltage dependent integrated photocurrent for the MWIR (3-8 μm) (red) and the LWIR (8-18 μm) (black). 82

5.1 Schematic diagram of (a) the QCD-Si and (b) the heterostructure of the QCD active region. 90
5.2 Conduction band profile of the SML QD QCD structure. 91
5.3 Bright field TEM image showing the GaAs-on-Si virtual substrate. The threading dislocation density (TDD) is about 3 $\times$ 10^7 $\mathrm{cm^{-2}}$ after the second dislocation filter layer (DFL2). 92
5.4 Normalised power dependent PL spectra for the samples (a) QCD-GaAs and (b) QCD-Si at 10 K. 93
5.5 Dark current density-voltage results measured at the temperatures from 77 K to 300 K. (a) QCD-GaAs and (b) QCD-Si. 95
5.6 Calculated zero bias differential resistance-area products ($\mathrm{R_0A}$) of (a) QCD-GaAs and (b) QCD-Si at the temperatures from 77 to 300 K. 96

5.7 Normal-incidence zero-bias absolute responsivities of (a) QCD-GaAs and (b) QCD-Si measured at the temperatures of 77 K, 120 K and 160 K. Device diameter = 210 μm. 97
5.8 Natural logarithm $\mathrm{R_0A}$ products versus 1/temperature for (a) QCD-GaAs and (b) QCD-Si. The $\mathrm{R_0A}$ activation energies for QCD-GaAs and QCD-SI are fitted as $E_{a,QCD-GaAs} = 159.3\ \mathrm{meV}$ and $E_{a,QCD-Si} = 120\ \mathrm{meV}$, respectively. 99
5.9 Johnson noise-limited detectivity of QCD-GaAs (black line) and QCD-Si (red line) in the detectors measured at 77 K and 160 K. 100

6.1 Cross-sectional view of the InAs/GaSb SL p-i-n photodiode on Si substrate. n-i-d = non-intentionally doped. 108
6.2 Cross-sectional (220) bright-field TEM image of the AlSb/Si interface. The average space between the Moiré fringes is about 1.64$\pm$0.06 nm. . . 109
6.3 (a) Low temperature power dependent PL spectra for the T2SL on GaAs (solid lines) and the T2SL on Si (dash lines). (b) Integrated PL for the T2SL on Si (black) and T2SL on GaAs (red) under different excitation powers at 10 K. 110
6.4 Dark current density-voltage characterisations of the T2SL on GaAs and Si measured at 77 K. 111
6.5 Energy band diagram of the nBp barrier detector with zero bias voltage. From left to right, (a) n-type top contact, (b) hole barrier, (c) absorber and (d) bottom contact. E_C, E_F and E_V are the effective conduction band edge, Fermi level and effective valence band edge, respectively. 112

6.6 (a) Cross-sectional view of the T2SL barrier detector on GaAs substrates and (b) simulation of the an structure with 25 nm 10 ML GaSb/10 ML InAs and 30 nm 12 ML InAs/6 ML AlSb. CB and VB are the conduction band edge and valence band edge, respectively. $|\psi_{\mathrm{e}}|^2$ and $|\psi_{\mathrm{h}}|^2$ are the probability density for electrons and holes, respectively. 113
6.7 High-resolution XRD rocking curve of the nBp detector on GaAs substrate. The fitted FWHM of the rocking curve is $0.05°$. 114
6.8 Temperature dependent dark current density-voltage characteristics of the nBp barrier detector (solid lines) and the p-i-n reference photodiode (dash lines). 116
6.9 Natural logarithm dark current density measured at - 0.1 V as a function of the inverse temperature (1/T). 117
6.10 Temperature dependent photoresponsivity measurements of a nBp detector with the diameter of 130 μm.[1] 118
6.11 Johnson noise-limited detectivity of the nBp detector on GaAs measured at temperatures from 77 K to 190 K. 120

List of Tables

1.1 Comparisons between different infrared detector materials. 5

5.1 Summarised PL peak information. Peak positions and FWHM values of the PL measured under the excitation power density of 0.1 $\mathrm{W/cm^2}$ at 10 K. Bulk GaAs peaks are not included in the table. The fitting results were extracted by using OriginLab. 94

5.2 Comparison of reported QCDs with the QCDs in this work. N is the number of cascade period and λ_p is the peak response wavelength. 101

6.1 Comparisons of the T2SL detectors grown on different substrates with various structural design at liquid nitrogen temperature. λ_{cutoff} is the cut-off wavelength, J_d is the dark current density, and D^* is the peak detectivity. 121

7.1 Summary of the experimental sections. Est. TDD = Estimated Threading Dislocation Density, LN = Liquid Nitrogen, Max. Temp = Maximum Operating Temperature. 128

List of Abbreviations

AFM	Atomic Force Microscopy
APB	Antiphase Boundary
APD	Antiphase Domain
B-B	Bound-to-Bound
B-C	Bound-to-Continuum
BLIP	Background Limited Infrared Performance
B-QB	Bound-to-Quasibound
BTB	Band-to-Band Tunnelling
CMOS	Complementary Metal-Oxide-Semiconductor
DFL	Dislocation Filter Layer
DTGS	Deuterated Triglycine Sulfate
DWELL	Quantum Dots-in-a-Well
EQE	External Quantum Efficiency
FPA	Focal Plane Array
FTIR	Fourier-Transform Infrared Spectroscopy
FWHM	Full Width at Half Maximum
G-R	Generation-Recombination
HOT	High Operating Temperature
HRXRD	High Resolution X-ray Diffraction
IMF	Interfacial Misfit
IR	Infrared Radiation
LO	Longitudinal Optical
LT	Low Temperature
LWIR	Long Wavelength Infrared

MBE	Molecular Beam Epitaxy
MD	Misfit Dislocation
ML	Monolayer
MOCVD	Metal-organic Chemical Vapour Deposition
MWIR	Middle Wavelength Infrared
NL	Nucleation Layer
PC	Photoconductive
PL	Photoluminescence
PV	Photovoltaic
QCD	Quantum Cascade Detector
QD	Quantum Dot
QDIP	Quantum Dot Infrared Photodetector
QE	Quantum Efficiency
QWIP	Quantum Well Infrared Photodetector
RTP (RTA)	Rapid Thermal Processing (Rapid Thermal Annealing)
S-K	Stranski-Krastanov
SL	Superlattice
SLS	Strained-Layer Superlattice
SML QD	Sub-Monolayer Quantum Dot
SNR	Signal-to-Noise Ratio
SRH	Shockley-Read-Hall
SWIR	Short Wavelength Infrared
T2SL	Type-II Superlattice
TAT	Trap-Assisted Tunnelling
TD	Threading Dislocation
TEM	Transmission Electron Microscopy
UHV	Ultra-High Vacuum
XRD	X-ray Diffraction

List of Publications

C.G. Burguete, D. Guo, P. Jurczak, F. Cui, M. Tang, W. Chen, Z. Deng, Y. Chen, M. Gutierrez, B. Chen, H. Liu and J. Wu, "Direct growth of InAs/GaSb type II superlattice photodiodes on silicon substrates", *IET Optoelectronics*, vol. 12, no.1, pp. 2 - 4, 2017.

J. Huang*, D. Guo*, W. Chen, Z. Deng, Y. Bai, T. Wu, Y. Chen, H. Liu, J. Wu, and B. Chen, "Sub-monolayer quantum dot quantum cascade mid-infrared photodetector", *Applied Physics Letters*, vol. 111, no. 25, pp. 251104, 2017. (*equal contribution)

W. Chen, Z. Deng, D. Guo, Y. Chen, Y. Mazur, Y. Maidaniuk, M. Benamara, G.J. Salamo, H. Liu, J. Wu and B. Chen, "Demonstration of InAs/InGaAs/GaAs Quantum dots-in-a-well Mid-wave Infrared Photodetectors Grown on Silicon Substrate", *Journal of Lightwave Technology*, vol. 36, no. 13, pp. 2572 - 2581, 2018.

D. Guo, Q. Jiang, M. Tang, S. Chen, Y. Mazur, Y. Maidaniuk, M. Benamara, M.P. Semtsiv, W.T. Masselink, G.J. Salamo, H. Liu and J. Wu, "Two-colour $\mathrm{In_{0.5}Ga_{0.5}As}$ quantum dot infrared photodetectors on silicon", *Semiconductor Science and Technology*, vol. 33, no. 9, pp. 094009, 2018.

J. Huang*, D. Guo*, Z. Deng, W. Chen, H. Liu, J. Wu and B. Chen, "Midwave Infrared Quantum Dot Quantum Cascade Photodetector Monolithically Grown on Silicon Sub-

strate", *Journal of Lightwave Technology*, vol. 36, no. 18, pp. 4033 - 4038, 2018. (*equal contribution)

Z. Deng*, D. Guo*, J. Huang, H. Liu, J. Wu and B. Chen, "Mid-Wave Infrared InAs/GaSb Type-II Superlattice Photodetector With n-B-p Design Grown on GaAs Substrate", *IEEE Journal of Quantum Electronics*, vol. 55, no. 4, pp. 1-5, 2019. (*equal contribution)

Z. Deng*, D. Guo*, C. Burguete, Z. Xie, J. Huang, H. Liu, J. Wu and B. Chen, "Demonstration of Si based InAs/GaSb type-II superlattice p-i-n photodetectors", *Infrared Physics & Technology*, vol. 101, pp. 133-137, 2019. (*equal contribution)

Chapter 1

Thesis Introduction

1.1 Background

Infrared (IR) radiation is an electromagnetic radiation, which has a wavelength range from 0.75 to 1000 μm. The infrared spectrum is often divided into several sub-divisions, including near infrared (NIR) from 0.75 to 1 μm, short-wavelength infrared (SWIR) from 1 to 3 μm, mid-wavelength infrared (MWIR) from 3 to 8 μm, long-wavelength infrared (LWIR) from 8 to 15 μm, very long wavelength Infrared (VLWIR) from 15 to 30 μm and far infrared up to 1000 μm [1, 2]. Infrared signature detection and thermography have many important applications in the defence, security, surveillance, automotive, scientific research and medical diagnosis fields, such as missile tracking, night vision, chemical sensing and skin cancer diagnosis [3–5].

Current research and development activities in infrared thermal camera technology are particularly focused on multicolour detection, high frame rate, high pixel density, large format, and/or multiple on-chip functions for high-end applications [6–8]. Meanwhile, major opportunities exist for high operating temperature (HOT) imagers with moderate performance; research related to size, weight, power and ease-of-use problems would have high value in this segment [9, 10]. As the core of an infrared imaging system, the

infrared detector has to be upgraded to meet the increasing demands. Current mainstream infrared materials, such as VO_x, amorphous Si, DTGS[1], HgCdTe, InSb, III-V quantum wells (QWs) and Sb-based type-II superlattices (T2SLs), have shown their future-proof capabilities for the infrared market [11–14]. VO_x and amorphous Si are the most commonly used bolometer materials and DTGS is a pyroelectric detector material. Bolometers as well as other thermal detector technologies have advantages in uncooled operation, affordability and portability, which are useful qualities in expendable and price-sensitive applications [15]. Other materials belong to the photodetector category. A comparision will be given shortly in Table 1.1. Photodetectors have a better frame rate and sensitivity than thermal detectors, and are suitable for performance-driven applications [16].

HgCdTe is a benchmark material with many desirable characteristics for infrared detection, such as a tuneable bandgap, high absorption coefficient and long carrier lifetime [17]. The bandgap of HgCdTe is easily tuned with the ratio of constituent alloys, i.e. HgTe to CdTe ratio [18]. Detectors made from HgCdTe materials can cover the infrared window from 1 - 25 μm [19]. The high optical absorption coefficient of HgCdTe enables a high absorption quantum efficiency (QE) with a relatively thin absorber. The long carrier lifetime can translate to a long diffusion length, since the diffusion length is proportional to the square root of the carrier lifetime [20]. For the photon-excited carriers to be collected, carrier generation must take place within the diffusion length from the junction or collector, whereas carriers originating outside the diffusion length cannot be collected and make no contribution to the external QE [21]. The long carrier lifetime and high absorption coefficient allow the HgCdTe detectors to operate with a nearly ideal QE ($>$90% with anti-reflective coating) and low thermal dark current (reduced detector thickness due to high absorption). Despite the technology having been developed for many decades, HgCdTe detectors still remain expensive and the technologies are not as widely accessible as group IV and III-V semiconductor technologies. These issues are bottlenecks for

[1]DTGS = Deuterated Triglycine Sulfate

wide deployment of infrared systems in civil and other price-sensitive applications [22]. III-V quantum structured photodetectors have attracted increasing attention as they can offer a competitive performance at a lower price. The terminology *III-V quantum structured photodetectors* in this thesis refer to the detector medium that has a quantum size effect, such as quantum dot and quantum well.

III-V quantum well infrared photodetector (QWIP)-based infrared focal plane arrays (FPAs) have rapidly entered the commercial market owing to the mature III-V technology, high uniformity, high yield and low cost, and have rivalled HgCdTe FPAs in the LWIR regime since the 1990s. The response wavelength of a QW depends on the intersubband transition energy in the conduction band (n-type QWs) or valence band (p-type QWs), which is adjustable by the choice of material and well width. State-of-the-art QW FPAs are commonly made by stacking of multiple n-type QWs, rather than p-type QWs, due to the poor hole mobility and lifetime [23]. However, the polarisation selection rule states that the intersubband transition in the conduction band can only be valid when the infrared electric field has a non-zero component in the QW growth direction or z-direction [24]. In other words, n-type QWIPs cannot respond to normal infrared incidence, since the normal incidence polarises entirely in the x-y plane. To endow normal incidence operation, a light coupler, e.g. a 2D grating array, must be incorporated into the QWIP to redirect the normal incidence into z-polarisation [25], which is a costly and complex manufacturing step.

Another intersubband detector, the quantum dot infrared photodetector (QDIP), has the potential to solve the problems of the QWIPs, owing to its three-dimensional (3D) carrier confinement. For example, QDIPs have intrinsic normal incidence absorption and low thermionic dark current. The low thermionic dark current originates from the better carrier confinement in the QDs, allowing the QDIPs to operate at higher temperature. Experimental demonstrations revealed that a QDIP can outperform a QWIP of similar structure on a single pixel scale [26]. However, current QD FPAs do not provide sensitiv-

ity as high as that of QW FPAs, primarily due to the relatively low QE ($\sim 2\%$) and low uniformity of the QD FPAs [27]. Compared with interband detectors, intersubband detectors suffer from low absorption QE. This can be explained by comparing the 2D (QW) and 0D (QD) subband density of states with the band-to-band 3D density of states [28]. QWIPs and QDIPs have fewer available subband states to participate in the optical transitions compared with the interband detectors, thereby lowering the absorption QE [16]. In addition, the large dot size inhomogeneity, which results in a broadening of the absorption linewidth, and the low dot sheet density associated with current QD fabrication methods imply a further reduction of absorption and QE in QDIPs [29].

Sb-based interband T2SLs photodetectors, where the heterostructure has a type-II band alignment, have better QE than intersubband detectors. Analysis shows that T2SL detectors can have a similar or even better performance than HgCdTe detectors [30]. The optical transition energy is highly adjustable and covers a wide spectrum range from SWIR to VLWIR, depending on the material combination and layer thickness [31]. The carrier lifetime is expected to be long due to the suppressed Auger recombination [30]. Moreover, the band-to-band tunnelling current is lower compared with similar bandgap HgCdTe due to the larger electron effective mass of T2SLs [31]. Although companies such as Lynred (a joint venture by Sofradir and ULIS) and SemiConductor Devices have expanded their MWIR and LWIR product line with T2SL detectors, the potential of T2SLs is yet to be fully unleashed. Research efforts are focusing on better device design through deeper physical understanding, controlling surface leakage through better passivation and reducing junction-related dark current by improving the material quality to compete with state-of-the-art HgCdTe detectors [32]. Table 1.1 gives a summary of the different detector technologies.

Table 1.1: Comparisons between different infrared detector materials.

Type		Advantages	Disadvantages
Thermal	Bolometer Pyroelectric	Light, low cost and reliable Uncooled operation	Slow response Low detectivity Microphonic effect (Pyro)
Photon	InSb	Very mature technology	Fixed bandgap
	HgCdTe	Tunable bandgap Mature technology High absorption coefficient Low dark current	Expensive Low uniformity (VLWIR)
	QWs	Tunable bandgap Mature technology High uniformity	No normal incidence absorption High thermionic dark current
	QDs	Normal incidence operation Low thermionic dark current	Low QE ($\sim$2%)
	T2SLs	Tunable bandgap Good absorption coefficient Long Auger lifetime	Surface leakage Intermixing at SL interface

1.2 Motivations

Lattice-matched substrates are the preferred choice for epitaxial growth of high-quality semiconductor materials. However, the lattice-matched substrates for growing II-VI and III-V semiconductors are expensive and some of the substrates are small in size, e.g. CdZnTe (7×7 cm^2) and GaSb substrates (4 inches in diameter) [33]. Silicon (Si) is one of the most abundant elements on earth and Si semiconductor technology is the most ad-

vanced semiconductor technology. Direct growth of III-V photodetectors on Si substrates can bridge the gap between III-V detector and Si semiconductor technologies and enjoys the benefits of Si technology:

Time and processing cost can be saved by means of using large wafers, since more dies can be manufactured on a single wafer. High-quality Si substrates with diameter up to 300 mm are available at a very low cost per unit area, making them a good solution for manufacturing of infrared detectors and arrays at low cost and in high volume. Direct growth of III-V infrared photodetectors on industrially compatible Si substrates can benefit from manufacture in mature Si complementary metal-oxide-semiconductor (CMOS) foundries. Specifically, it is possible to integrate III-V infrared photodetectors with Si optoelectronic components for low-cost and high volume production. For example, a mid-infrared lab-on-a-chip sensor system for chemical sensing could be built up from the following components: a light source, sensing elements, photodetectors and read-out circuitry, on a monolithic Si platform. [34].

A more ambitious motivation is to realise the integration of III-V detectors with Si readout integrated circuits. At present, the detector array and its readout circuit (sensor-chip assembly) are typically interconnected by using the flip-chip bonding method [35]. Since the III-V array and the Si chip have different thermal expansion coefficients, temperature cycling between ambient and operating temperature can generate thermal stress and cause fatigue to the interconnects (solder balls) [36]. This will restrict the maximum size of the sensor-chip assembly in order to maintain its performance and challenges the development of large-format arrays. Direct growth of III-V detector arrays on Si substrates with pre-patterned readout circuitry will no longer require the flip-chip bonding steps, thus eliminating the interconnect fatigue issue. Monolithic integration of III-V photodetectors on Si via the direct growth method has the potential to improve the cost-efficiency, functionality and reliability of the infrared system. However, there are several technology and economic barriers to commercialisation and practical usage. First and

foremost, the performance of III-V photodetectors on Si is behind the III-V detectors on native substrates, due to the defects associated with the III-V on Si heteroepitaxy:

- Si is nonpolar material and III-V materials are polar materials. Direct growth III-Vs on Si (001) substrates tend to produce antiphase domains. The antiphase domains are bulk imperfections which can cause reduction in performance or failure of the device.

- The lattice constant mismatch between GaAs and Si is about $\sim 4\%$ and for GaSb on Si it is about $\sim 12\%$. Introduction of dislocations is inevitable in order to accommodate the excess strain energy. Threading dislocations, which propagate along the growth direction, can enter the device activation region, acting as recombination centres and reducing the carrier lifetime.

- The thermal expansion coefficient mismatch between the III-Vs and Si limits the maximum thickness of the III-V epitaxy layers without thermal cracks. The calculated maximum thickness of GaAs epi-layer on Si is about 7 μm at the growth temperature of $\sim 575^{\circ}\mathrm{C}$ and this value reduces with increasing temperature [37]. In the real world, the thickness can be even smaller when other factors, such as the strain, thermal annealing temperatures, etc. are considered, and may become a restriction for the device design.

These challenges will be further discussed in the next chapter, which addresses the generation and mitigation mechanisms of the defects.

From the industry perspective, epitaxial growth currently takes place in a high temperature environment (e.g. the Si substrate pre-treatment temperature $\sim 900^{\circ}\mathrm{C}$), which can cause damage to the pre-existing functional components. This is a fundamental difficulty of the integration prospect. Additionally, the market volume of III-V infrared system is significantly smaller than the Si integrated circuits market. Reducing the cost barriers and

diversifying the applications of infrared systems are essential in order to attract the attention of the semiconductor market and industry. Addressing these challenges will require substantial innovation effort and capital investments in epitaxy techniques, device design, manufacturing techniques, market expansion, etc. This thesis will focus on device design based on recent advancements in III-V on Si heteroepitaxy techniques.

1.3 Objective

As will be seen in following chapters, although the defect density can be effectively reduced by using an optimised III-V buffer, the remaining defect density is still higher than for the materials on native or lattice-matched substrates. Previous work has rarely focused on improving detector performance by optimising the device design above the III-V buffer. In order to further boost the performance, **this thesis aims to explore quantum structured detectors to mitigate the performance degradation associated with material defects**. There are four types of III-V quantum structured infrared photodetectors that will be covered, namely QDIPs, sub-monolayer QD quantum cascade detectors (SML QD QCDs), T2SL p-i-n photodiodes and T2SL barrier detectors.

The study of QDIPs is motivated by the high defect tolerance characteristic of QDs [38]. In QWs and bulk materials, the carriers are free to move in non-confined dimensions and can easily diffuse to the defect states [38], while in QDs, since the carriers are localised inside the QDs and immobilised, only the defects created inside or near the QDs will have an effect on the carriers [38, 39]. Thus, it would be expected that the III-V QDIPs will have better defect tolerance than the III-V QWIPs or III-V bulk detectors.

The study of QCDs is motivated by their photovoltaic (PV) operation, which offers low device noise and low power dissipation (no bias requirement), compared with the QDIPs [40]. Using an SML QD absorber instead of a QW absorber would take advantage of the 3D carrier confinement of QDs, e.g. normal incidence operation and low thermal

generation rate.

The study of T2SL based photodetectors is motivated by their higher absorption QE than intersubband detectors. This thesis compares the performance of T2SL p-i-n photodiodes and the T2SL nBp barrier detector. With a low level of generation-recombination current, the nBp barrier detectors show lower dark current than the p-i-n photodiodes. Compared with p-i-n photodiodes, the barrier detectors have the capability to eliminate or reduce the generation-recombination (G-R) dark current, which is good for low dark current and high temperature operation. More detail related to the device design will be covered in chapter 2. The chart in Figure 1.1 gives a brief presentation of the research motivations and objectives.

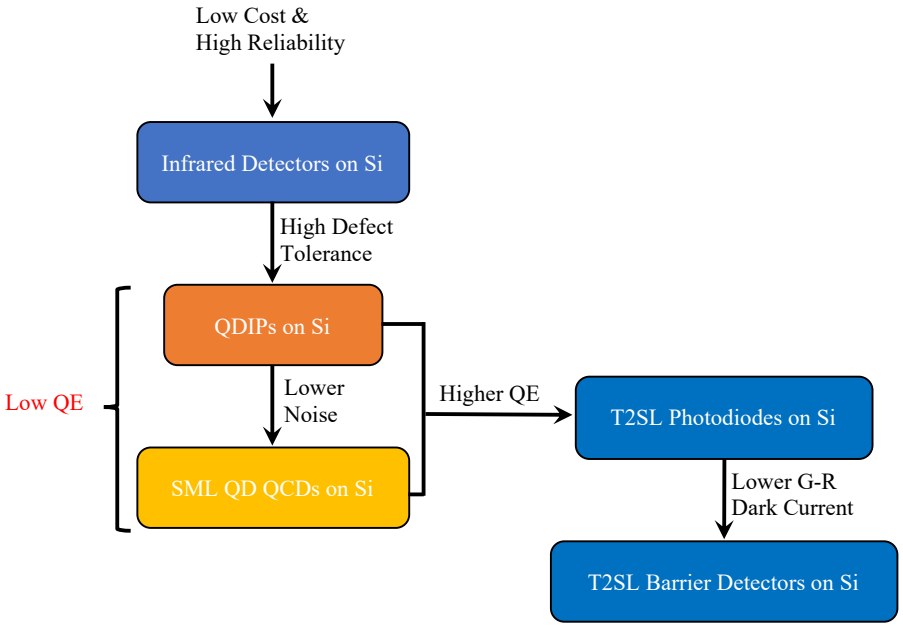

Figure 1.1: Overview of the thesis motivations and objectives.

1.4 Thesis Outline

This thesis has seven chapters.

The first chapter introduces the background and objectives of the thesis. The second

chapter introduces the quantum structured infrared photodetectors that will be studied in this thesis. Chapter 2 also discusses the III-V buffer technologies that are available for minimising the impact of the direct growth of III-V compounds on Si. The challenges to the epitaxy growth and the device design are introduced in chapters 1 and 2.

The third chapter introduces the experimental work, including detector fabrication, material characterisation equipment and device characterisation techniques.

As a proof of concept, the fourth chapter reports on the direct growth of $\mathrm{In_{0.5}Ga_{0.5}As}$ /GaAs QDIPs on Si. By using an optimised III-V buffer, the threading dislocation density is reduced by about 3-4 orders of magnitude. Time-resolved PL measurements show that the PL lifetime of the InGaAs QDIPs on Si is close to that of similar InGaAs QDIPs on GaAs substrates. As a consequence of the improved material quality, the InGaAs QDIPs on Si operate successfully at 77 K with two-colour photoresponse.

In order to obtain a better noise performance of the infrared detectors on Si, the fifth chapter studies the SML QD QCD structure. The SML QD QCD on GaAs has similar photoresponse performance characteristics to the SML QD QCD on Si, but shows lower thermal noise at 77 K. This is attributed to the lower diagonal transition energy of the SML QD QCD on Si. At higher temperatures, the thermal noise performance differences become smaller as the detector resistance reduces rapidly with temperature. Both the detectors operate up to 160 K, regardless of the higher defect density of the SML QD QCD on Si.

To improve the QE performance of the infrared detectors on Si, chapter 6 studies T2SL-based infrared photodetectors. Chapter 6 begins with a discussion of direct growth of InAs/GaSb T2SL photodiodes on Si and GaAs substrates. Due to the high defect density in the materials, a high dark current is observed in both photodiodes. In order to reduce the junction-related dark current, a nBp T2SL barrier detector is studied in the second part of the chapter 6. The nBp barrier detector shows a lower dark current than the reference p-i-n photodiode, which indicates that the barrier design reduces the generation

of G-R current effectively. By taking the benefits of the barrier design, the nBp detectors on GaAs can operate at temperatures as high as 190 K under 0 V.

Finally, the seventh chapter concludes the work described in chapters 4-6 and makes suggestions based on the findings of this thesis for further improvements to the performance of III-V infrared photodetectors on Si.

All contributions from our collaborators are mentioned in the contribution statement sections.

References

[1] F. Zhuge *et al.*, "Nanostructured materials and architectures for advanced infrared photodetection," *Advanced Materials Technologies*, vol. 2, no. 8, p. 1700005, 2017.

[2] A. Rogalski, *Infrared and Terahertz Detectors, Third Edition*. Taylor & Francis Ltd, 2018.

[3] S. Bagavathiappan *et al.*, "Infrared thermography for condition monitoring – a review," *Infrared Physics & Technology*, vol. 60, pp. 35–55, 2013.

[4] V. Farley *et al.*, "Chemical agent detection and identification with a hyperspectral imaging infrared sensor," in *Electro-Optical Remote Sensing, Detection, and Photonic Technologies and Their Applications* (G. W. Kamerman, O. K. Steinvall, K. L. Lewis, K. A. Krapels, J. C. Carrano, and A. Zukauskas, eds.), SPIE, 2007.

[5] B. Lahiri *et al.*, "Medical applications of infrared thermography: A review," *Infrared Physics & Technology*, vol. 55, no. 4, pp. 221–235, 2012.

[6] W. Cabanski *et al.*, "Third generation focal plane array IR detection modules and applications (invited paper)," in *Infrared Technology and Applications XXXI* (B. F. Andresen and G. F. Fulop, eds.), SPIE, 2005.

[7] P. R. Norton *et al.*, "Third-generation infrared imagers," in *Infrared Technology and Applications XXVI* (B. F. Andresen, G. F. Fulop, and M. Strojnik, eds.), SPIE, 2000.

[8] A. Rogalski, J. Antoszewski, and L. Faraone, "Third-generation infrared photodetector arrays," *Journal of Applied Physics*, vol. 105, no. 9, p. 091101, 2009.

[9] P. Martyniuk and A. Rogalski, "HOT infrared photodetectors," *Opto-Electronics Review*, vol. 21, no. 2, 2013.

[10] D. A. Reago *et al.*, "Third-generation imaging sensor system concepts," in *Infrared Imaging Systems: Design, Analysis, Modeling, and Testing X* (G. C. Holst, ed.), SPIE, 1999.

[11] A. Rogalski, "Recent progress in third generation infrared detectors," *Journal of Modern Optics*, vol. 57, no. 18, pp. 1716–1730, 2010.

[12] W. A. Radford *et al.*, "Third generation FPA development status at Raytheon Vision Systems (invited paper)," in *Infrared Technology and Applications XXXI* (B. F. Andresen and G. F. Fulop, eds.), SPIE, 2005.

[13] A. Rogalski, "Recent progress in infrared detector technologies," *Infrared Physics & Technology*, vol. 54, no. 3, pp. 136–154, 2011.

[14] A. Rogalski, "Next decade in infrared detectors," in *Electro-Optical and Infrared Systems: Technology and Applications XIV* (D. A. Huckridge, R. Ebert, and H. Bürsing, eds.), SPIE, 2017.

[15] M. Vollmer and K.-P. Möllmann, *Infrared Thermal Imaging*. Wiley-VCH Verlag GmbH & Co. KGaA, 2017.

[16] A. Rogalski, "Infrared detectors: status and trends," *Progress in Quantum Electronics*, vol. 27, no. 2-3, pp. 59–210, 2003.

[17] W. Lei, J. Antoszewski, and L. Faraone, "Progress, challenges, and opportunities for HgCdTe infrared materials and detectors," *Applied Physics Reviews*, vol. 2, no. 4, p. 041303, 2015.

[18] G. L. Hansen, J. L. Schmit, and T. N. Casselman, "Energy gap versus alloy composition and temperature in $\mathrm{Hg_{1-x}Cd_xTe}$," *Journal of Applied Physics*, vol. 53, no. 10, pp. 7099–7101, 1982.

[19] A. Rogalski, "HgCdTe infrared detector material: history, status and outlook," *Reports on Progress in Physics*, vol. 68, no. 10, pp. 2267–2336, 2005.

[20] C. Canedy *et al.*, "Controlling dark current in type-II superlattice photodiodes," *Infrared Physics & Technology*, vol. 52, no. 6, pp. 326–334, 2009.

[21] L. Höglund *et al.*, "Manufacturability of type-II InAs/GaSb superlattice detectors for infrared imaging," *Infrared Physics & Technology*, vol. 84, pp. 28–32, 2017.

[22] J. Wu *et al.*, "Monolithically integrated InAs/GaAs quantum dot mid-infrared photodetectors on silicon substrates," *ACS Photonics*, vol. 3, no. 5, pp. 749–753, 2016.

[23] B. F. Levine, "Quantum-well infrared photodetectors," *Journal of Applied Physics*, vol. 74, no. 8, pp. R1–R81, 1993.

[24] H. C. Liu, M. Buchanan, and Z. R. Wasilewski, "How good is the polarization selection rule for intersubband transitions?," *Applied Physics Letters*, vol. 72, no. 14, pp. 1682–1684, 1998.

[25] A. Rogalski, "Quantum well photoconductors in infrared detector technology," *Journal of Applied Physics*, vol. 93, no. 8, pp. 4355–4391, 2003.

[26] A. Barve *et al.*, "Review of current progress in quantum dot infrared photodetectors," *Laser & Photonics Reviews*, vol. 4, no. 6, pp. 738–750, 2009.

[27] S. D. Gunapala *et al.*, "640 × 512 pixels long-wavelength infrared (LWIR) quantum-dot infrared photodetector (QDIP) imaging focal plane array," *IEEE Journal of Quantum Electronics*, vol. 43, no. 3, pp. 230–237, 2007.

[28] M. Liao *et al.*, "III-V quantum-dot lasers monolithically grown on silicon," *Semiconductor Science and Technology*, vol. 33, no. 12, p. 123002, 2018.

[29] J. Phillips, "Evaluation of the fundamental properties of quantum dot infrared detectors," *Journal of Applied Physics*, vol. 91, no. 7, pp. 4590–4594, 2002.

[30] D. L. Smith and C. Mailhiot, "Proposal for strained type-II superlattice infrared detectors," *Journal of Applied Physics*, vol. 62, no. 6, pp. 2545–2548, 1987.

[31] A. Rogalski, P. Martyniuk, and M. Kopytko, "InAs/GaSb type-II superlattice infrared detectors: Future prospect," *Applied Physics Reviews*, vol. 4, no. 3, p. 031304, 2017.

[32] I. Vurgaftman, "Analysis and performance of type-II superlattice infrared detectors," *Optical Engineering*, vol. 50, no. 6, p. 061007, 2011.

[33] S. Simingalam, B. L. VanMil, Y. Chen, *et al.*, "Development and fabrication of extended short wavelength infrared HgCdTe sensors grown on CdTe/Si substrates by molecular beam epitaxy," *Solid-State Electronics*, vol. 101, pp. 90–94, 2014.

[34] V. Singh *et al.*, "Mid-infrared materials and devices on a Si platform for optical sensing," *Science and Technology of Advanced Materials*, vol. 15, no. 1, p. 014603, 2014.

[35] J. Jiang *et al.*, "Advanced monolithic quantum well infrared photodetector focal plane array integrated with silicon readout integrated circuit," *Infrared Physics & Technology*, vol. 46, no. 3, pp. 199–207, 2005.

[36] J. Jiang *et al.*, "Fabrication of indium bumps for hybrid infrared focal plane array applications," *Infrared Physics & Technology*, vol. 45, no. 2, pp. 143–151, 2004.

[37] V. K. Yang *et al.*, "Crack formation in GaAs heteroepitaxial films on Si and SiGe virtual substrates," *Journal of Applied Physics*, vol. 93, no. 7, pp. 3859–3865, 2003.

[38] S. Marcinkevičius *et al.*, "Changes in luminescence intensities and carrier dynamics induced by proton irradiation in $\mathrm{In_xGa_{1-x}As/GaAs}$ quantum dots," *Physical Review B*, vol. 66, no. 23, 2002.

[39] X.-Q. Li and Y. Arakawa, "Ultrafast energy relaxation in quantum dots through defect states: A lattice-relaxation approach," *Physical Review B*, vol. 56, no. 16, pp. 10423–10427, 1997.

[40] J. Huang *et al.*, "Sub-monolayer quantum dot quantum cascade mid-infrared photodetector," *Applied Physics Letters*, vol. 111, no. 25, p. 251104, 2017.

Chapter 2

Introduction to Direct Growth of III-V Quantum Structured Infrared Photodetectors on Si substrates

2.1 Basic Principles of Infrared Detectors

Depending on the response mechanism, infrared detectors can be classified into two groups: thermal detectors and photodetectors. Thermal detectors are made of temperature-sensitive materials whose material properties change after absorbing the heat energy of the infrared radiation. Since this response mechanism does not depend on the photonic nature of the infrared radiation, thermal detectors can respond to a wide range of the infrared spectrum and do not cutoff at a specific wavelength. In a photodetector, an incident photon can excite an electron from a less conductive state to a conductive state resulting in an essentially instantaneous change in the electrical property of the detector. Since the electrical property changes very rapidly after the photon absorption, photodetectors are faster in response speed than thermal detectors. A fundamental requirement for photodetectors is that the photon energy must be equal to or larger than the energy gap between

the two electronic states, otherwise, the photon cannot be absorbed by the detector. Therefore, photodetectors have a well-defined cutoff wavelength, which is equal to the energy gap. Because of the narrow energy gap, infrared photodetectors are usually operated under an active cooling system in order to minimise the influence of thermally generated noise and thus achieve a better signal-to-noise ratio (SNR).

The infrared photodetector can convert incident infrared radiation into a measurable electrical current or voltage. The parameter that describes the conversion efficiency between the incident power and output photocurrent is called responsivity. The current responsivity is given by the equation [1],

$$R_i = \frac{I_{ph}}{P_{inc}} = \frac{q\lambda}{hc}\eta g_{ph} \quad (\mathrm{A/W}) \tag{2.1}$$

where h, c and q are the Planck constant, the speed of light, and the elementary charge, respectively. λ is the wavelength of incident infrared radiation, η is the absorption QE and g_{ph} is the photoconductive gain which equals to the carrier lifetime divided by carrier transit time.[1] For a signal to be detectable by a detector, the minimum signal power is the power that produces a SNR of one, or noise equivalent power (NEP) [2],

$$NEP_1 = \frac{I_n}{R_i} \quad (\mathrm{W}) \tag{2.2}$$

or sometimes it can be normalised to 1 Hz output bandwidth, giving an another expression of NEP [3],

$$NEP_2 = \frac{S_n}{R_i} \quad (\mathrm{W}/\sqrt{\mathrm{Hz}}) \tag{2.3}$$

where $S_n = I_n/\sqrt{\Delta f}$ is the noise current density and Δf is noise bandwidth. I_n is a sum of all types of noise current sources, e.g. generation-recombination (G-R) noise, thermal noise, shot noise, flicker noise. The G-R noise, thermal noise and shot noise

[1] In photodiodes, since the carrier lifetime equals carrier transit time, gain is generally considered as 1.

will be covered in the following sections. The flicker noise or $1/f$ noise is the noise typically related to material imperfections, and exhibits a spectrum where its intensity is inversely proportional to the frequency. The limitation of equation 2.2 is that it does not include detector area and noise bandwidth (included in equation 2.3), which are the variables for comparing the performance among different detectors. A normalised figure of merit, specific detectivity or D^*, is more frequently mentioned in research papers. The specific detectivity allows detectors in different technology systems to be compared and the mathematical expression of D^* is [2, 3],

$$D^* = R_i \frac{\sqrt{A\Delta f}}{I_n} = R_i \frac{\sqrt{A}}{S_n} \quad (\mathrm{cm} \cdot \sqrt{\mathrm{Hz}}/\mathrm{W}) \tag{2.4}$$

where A is the detector area. From the equation, one can see that the optimal detector design is to maximise the responsivity and minimise the noise.

2.2 III-V Quantum Structured Infrared Photodetector

2.2.1 Quantum Dot Infrared Photodetector

The idea of using QDs for optoelectronic applications can be traced back to 1982, when Arakawa and Sakaki reported that reducing the freedom of dimensionalities of carriers can lead to a reduction in the temperature sensitivity of a laser device [4]. The detection of infrared light in QWIPs and QDIPs relies on the intersubband transition of carriers from a confined energy level to a higher energy level entering/escaping into the continuum and thus contributing a photocurrent. QD based infrared photodetectors have several performance improvements compared with the QWIPs:

(i) the intersubband selection rules no longer restrict the normal incident light absorption in QDs, which avoids the need for complex grating structures when fabricating imaging devices [5];

(ii) in a QD, if the energy separation between two confined energy levels is greater than the energy of a longitudinal-optical (LO) phonon, the electron relaxation process will be suspended, resulting in the so-called phonon-bottleneck effect. The phonon-bottleneck effect in QDs allows the electrons to remain excited for longer before relaxing to the ground state. The extended carrier lifetime can translate to high photoconductive gain, and thus high responsivity [6];

(iii) the thermionic dark current is low, owing to the 3D carrier confinement and the discrete density of states [7].

There are three types of intersubband transitions, as depicted in Figure 2.1(a): the bound-to-bound (B-B), bound-to-continuum (B-C) and bound-to-quasi-bound (B-QB) transitions. The B-B transition has the highest absorption efficiency but requires the highest bias voltage for extracting the excited electrons, which increases the power requirement; the B-C transition is more suitable for low bias operation due to the high extraction probability; the B-QB transition, which combines the advantages of the other two types of transitions, is the optimal operation mode for high responsivity and low noise operation [8]. It is worth mentioning here that QDIP can operate in two or multiple colour mode, since several excited states (or intersubband transition energies) can coexist in a QD. For QDIPs, the photocurrent density can be modelled by the equation [1],

$$J_{ph} = q\eta\Phi_s g_{ph} \tag{2.5}$$

where Φ_s is signal photon flux per unit area. The carrier lifetime in QDIPs can be 100-1000 times longer than that in QWIPs, due to the photon-bottleneck effect as previously mentioned [9]. The long carrier lifetime increases the photoconductive gain as well as the responsivity.

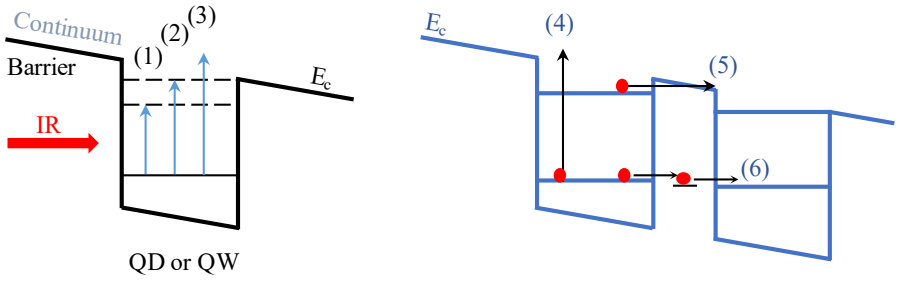

(a) Photoexcitation (b) Dark current generation

Figure 2.1: (a) Generation of photoexcited electrons by (1) B-B, (2) B-QB and (3) B-C transitions. (b) QDIPs dark current generation mechanisms (4) thermionic emission, (5) field assisted tunnelling or phonon assisted tunnelling and (6) defect assisted tunnelling. E_C is the conduction band edge of the barrier material.

G-R noise is the main source of noise in QDIPs, which is caused by the fluctuation in the rates of carrier trapping by and emission from the QDs [10],

$$I_{n,G-R} = \sqrt{4qg_nI_d\Delta f} \tag{2.6}$$

where g_n is the noise gain, which is usually the same as the photoconductive gain, Δf is the noise bandwidth and I_d is the dark current. Dark current is an important measure of detector performance, since its fluctuation generates noise and influences the SNR. Figure 2.1 (b) illustrates the main dark current generation mechanisms in QDIPs. Thermionic emission and field-assisted tunnelling currents are the main components of the dark current in QDIPs, while other tunnelling mechanisms, e.g. defect-assisted tunnelling and sequential resonant tunnelling [11], are the other dark current generation mechanisms.

There are several ways to reduce the dark current. Some research groups have incorporated wide bandgap AlGaAs into In(Ga)As/GaAs QDIPs as a current blocking layer(s) to suppress the transport of dark current [12–14]. Since the photocurrent and dark current share the same path, a reduction in photocurrent is inevitable with this approach. Resonant tunnelling barriers, which are designed to allow the escape of carriers with the same

energy as the resonant energy (i.e. the peak detection wavelength) and inhibit others, have been adopted in QDIPs to block the dark current and maintain the photocurrent [15, 16]. Doping is a crucial design consideration, since it influences both the dark current and photocurrent. Theoretical calculation suggested the optimal doping density is twice the QD sheet density or two electrons per dot, thereby filling the QD ground state and preventing the electrons from occupying the excited states [17]. However, considering the size inhomogeneity and the random nucleation sites of QDs, uniform doping is hard to realise. Various electron-to-dot ratios have been used to find the highest QDIP performance, for example non intentionally doped QDs [18], one electron per dot [19] and two electrons per dot [20].

QDIPs with a quantum dots-in-a-well (DWELL) active region were proposed to improve the wavelength tunability, barrier carrier confinement and multicolour operation [21]. The detection wavelength can be controlled by the material selection and the width of the well [22]. Raghavan et al. reported an InAs/InGaAs/GaAs DWELL detector with a high responsivity of 3.58 A/W owing to its high conversion efficiency (QE$\times$ gain) [23]. The dark current measured was much lower than the QWIPs with similar response wavelength due to the better electron confinement of the QDs [23]. Krishna et al. showed that the DWELL detector is capable of operating in three-colour mode covering the MWIR, LWIR and VLWIR regions [24]. Lim et al. reported a coupled InAs QDs layer with a highly doped InGaAs QWs DWELL design reaching a maximum QE of 35% [25].

Since the initial experimental demonstrations in 1998 [26–28], the performance of QDIPs has been significantly improved [7, 9]. QD based infrared FPAs have been realised in the laboratory, but their performance is inferior to that of state-of-the art QW FPAs due to the relatively low QE, high dark current and low spatial uniformity [29–31]. The inhomogeneous broadening of the QDs and relatively low QD sheet density are the main constraints of the current QDIP and QD FPAs. Recently, the UCL MBE group demonstrated the first QDIP on Si substrate by the direct growth method. The

threading dislocation density was reduced by about 4-5 orders of magnitude by using an optimised GaAs buffer and four sets of dislocation filter layers (DFLs) [32]. Both the dark current and carrier lifetime mentioned in this paper are comparable with those of InAs QDIPs on III-V native substrates, which indicates a good quality of material. With the improved material quality, the photocurrent was measured at 80 K over a range of wavelengths covering the 5 – 8 μm spectral region. Using the same buffer techniques, we reported InGaAs/GaAs QDIPs with two response peaks at ~ 6 μm and ~ 15 μm at 80 K [33]. Our collaborators from ShanghaiTech University reported an InAs/InGaAs/GaAs DWELL photodetector on Si [34]. With the designed B-QB transition and low device dark current, the reported detectivity is comparable to that of early reported GaAs based DWELL photodetectors. Optimisation should focus on improving the III-V buffers and QD size distribution.

2.2.2 Quantum Cascade Detector

Exploiting the advancements in the III-V semiconductor technology, scientists from the AT&T Bell Laboratories demonstrated a unipolar semiconductor laser called the quantum cascade laser (QCL) [35]. The emission energy is adjustable from the mid-infrared region to the submillimetre wave ($\sim$ 100 μm). Hofstetter et al. studied the photovoltaic behaviour of the QCL structures as detectors [36], and their study has inspired the development of bi-functional quantum cascade laser and detector structures to make an extremely compact chemical sensing system [37] and quantum cascade detectors (QCD) for thermal imaging. Gendron et al. optimised the quantum cascade structure [38], which can be viewed as the first QCD dedicated to infrared FPA applications. The QCD was able to operate without applying bias voltage, i.e. in photovoltaic (PV) mode. PV operation offers several benefits, including low noise, high operating temperature and low power dissipation [39]. Figure 2.2 illustrates a simplified conduction band diagram of the QCD. One period of the QCD activation region contains an absorber and several cascade QWs,

i.e. the extractor. The electrons in the absorber region can be excited from the ground state to the excited state after absorption of infrared light. The extractor region comprises several QWs with carefully adjusted energy levels. The energy separation between two adjacent QWs is about the energy of one LO phonon (e.g. GaAs: $\mathrm{E_{LO}} = 36\ \mathrm{meV}$) [40]. Photoexcited electrons entering the extractor can rapidly relax to the ground states of the next period and contribute to photocurrent.

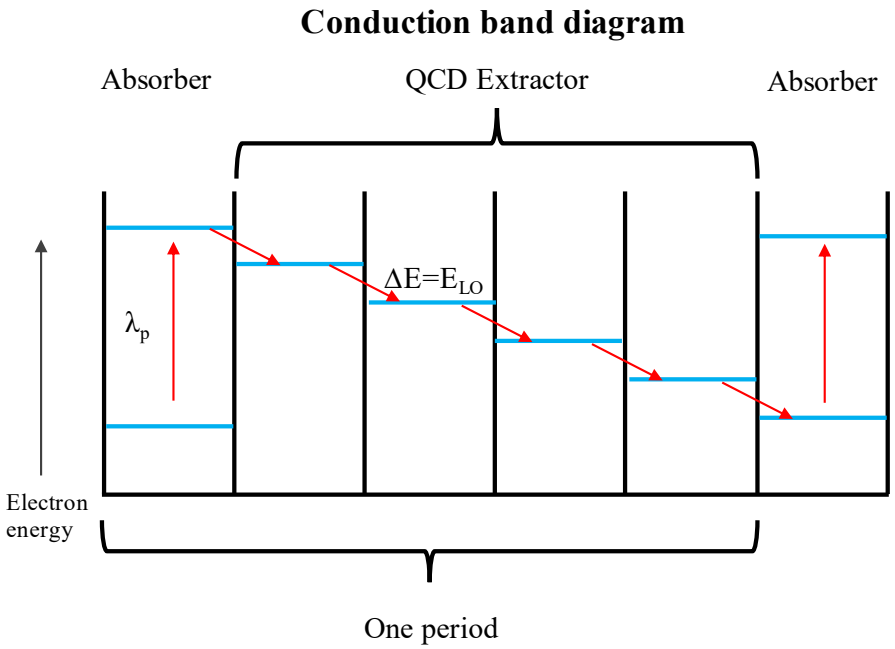

Figure 2.2: Schematic conduction band diagram of the QCD and the cascade transport [40]. Electron intersubband transition occurs in the absorber region after exposure to IR. The photoexcited electron can tunnel through the barrier into the next QW by releasing an LO phonon. By repeating the tunnelling process for several times, the electron cascade over the cascade stages resulting in measurable photocurrent. λ_p is the peak absorption wavelength.

According to the equation 2.1, the responsivity of a detector is proportional to the conversion efficiency, ηg_{ph}. The photoconductive gain of a QCD is expressed as [40],

$$g_{ph} = \frac{p_e}{N p_c} \tag{2.7}$$

where p_e is the escape probability of excited electrons entering the extractor and p_c is the capture probability of electrons cascading to the ground state of the next absorber. Designing well-aligned "phonon-stairs" and maximising the oscillator strength between the absorber excited state and the first extraction QW ground state are crucial factors in achieving high photoconductive gain [41]. In addition, the g_{ph} is proportional to 1/N, meaning that the more cascade periods, the smaller the photoconductive gain. Since η increases roughly in proportion to the number of cascade periods, N should be carefully determined in order to obtain the optimal conversion efficiency.

The noise characteristics of the QCD depend on whether its performance is external noise-limited or internal-noise limited. For detectors operating at temperatures where the device dark current is smaller than the photocurrent generated by the background flux, the detector performance is limited by the external noise source or the background limited infrared performance (BLIP). Kinch formalised the BLIP condition as $\Phi_{\mathrm{B}} > \mathrm{n_{th}}/\alpha t$ [42], where Φ_{B} is background photon flux, $\mathrm{n_{th}}$ is a function of temperature representing the density of thermal carriers, and α and t are the absorption coefficient and absorber thickness, respectively. Above the BLIP temperature, i.e. at temperatures where $\Phi_{\mathrm{B}} < \mathrm{n_{th}}/\alpha t$, the internal noise overtakes the external noise and the detector performance is limited by the device noise. The main device internal noise of a PV QCD is the thermal or Johnson noise, which is caused by the random thermal motion of charge carriers. The mathematical expression for the Johnson noise current is [10],

$$I_{n,J} = \sqrt{\frac{4k_B T \Delta f}{R}} \tag{2.8}$$

where R is the differential resistance of the device and Δf is the noise bandwidth. The Johnson noise limited detectivity of the QCDs in PV mode can be expressed as [43],

$$D_J^* = R_i \sqrt{\frac{R_0 A}{4k_B T}} \tag{2.9}$$

where R_0A is the zero-bias differential resistance-area product, which is a commonly mentioned figure of merit for PV detectors, since it relates to the thermal noise. Conventional QW QCDs using QWs as the absorber layer cannot respond to normal-incident light. By replacing the QW absorber by a QD absorber, we can regain the normal incident operation. Barve and Krishna demonstrated a MWIR QD QCD on GaAs with a DWELL absorber, which had a great flexibility in adjusting the position of excited states inside the QWs [44]. Wang et al. reported an InP based MWIR QD QCD enjoying a broad selection of materials that matched with the InP substrate [45]. The detector performed with a BLIP temperature of 134 K for a 300 K background and a hemispherical field of view [45]. Huang et al. used the sub-monolayer QDs as the absorber and demonstrated an SML QD QCD with a peak response wavelength at 6 μm [46]. Later, Huang et al. reported the first SML QD QCD on Si substrates with the same activation region design [47]. With a high R_0A value, the performance was comparable to that in the work of Brave and Krishna [44].

2.2.3 InAs/GaSb T2SL Photodetector

InAs and GaAs have typical type-II band alignments, where the conduction band edge of InAs is lower than the valence band edge of GaSb, or broken gap band alignment. This band alignment is preferred for electrons and holes to reside in the InAs layer and GaSb layers, respectively, in order to minimise the energy, as shown in Figure 2.3 [48]. The InAs/GaAs SLs are formed by alternate deposition of InAs and GaSb with hundreds of iterations. Each constituent layer is as thin as a few nanometres, thus the electrons and holes can tunnel through the SLs, forming effective minibands as shown in Figure 2.3 [49]. The energy separation between the conduction miniband and the heavy hole miniband mainly depends on the quantisation energy of the electrons, which is a function of the InAs thickness. The quantisation energy of holes is less sensitive to the layer thickness than the electron quantisation energy, owing to the large hole effective mass.

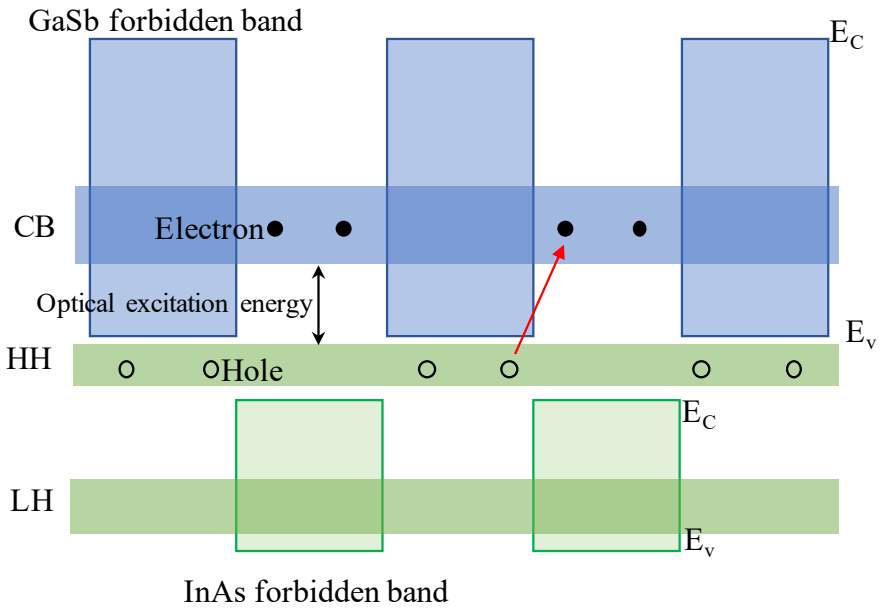

Figure 2.3: Illustration of the T2SL effective mini bands [50]. CB, HH and LH represent the effective conduction band, effective heavy hole band and effective light hole band. E_c and E_V the are conduction band edge and valence band edge, respectively. The colour boxes are the forbidden bands of GaSb (blue) and InAs (green). The optical excitation energy is the energy separation between CB and HH.

As the parts of the "6.1 Å family", the differences in lattice constant among InAs (6.0584 Å), GaAs (6.0959 Å), AlSb (6.1355 Å) and their alloys are relatively small [51]. The nearly lattice-matched materials fulfil the layer-by-layer growth of one material on top of another without generating uncontrollable strain. On the other hand, strained layer superlattices (SLSs) enable the separation of HH and LH bands [52]. If the energy separation between the HH and the LH bands is more than the effective bandgap, the Auger recombination in p-type T2SLs can be suppressed. Auger recombination is a three-particle recombination process, where the electron and hole recombine and excite a third particle (electron or hole) to a higher energy state. For n-type T2SLs, the conduction miniband can be engineered to become narrower than the effective bandgap to reduce the conduction band Auger transitions [53]. Moreover, the spatial separation of electron and hole wavefunctions hinders the band-to-band transitions, which results in a further reduction

of the Auger recombination rate and increase in carrier lifetime. Apart from the Auger recombination, the Shockley-Read-Hall (SRH) process is another important recombination mechanism in a photodiode. The defect states in the bandgap are responsible for the SRH recombination, and the recombination rate reaches a maximum value as the defect states approach the mid-gap. At present, the HgCdTe detectors clearly win with respect to SRH recombination, mainly due to the high material quality [48]. Overall, the carrier lifetime of T2SL detectors is still behind HgCdTe detectors in practical devices.

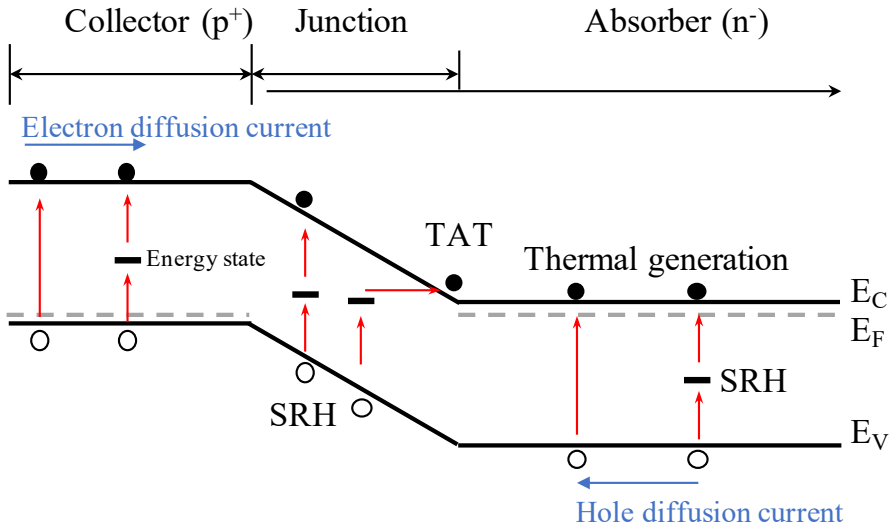

Figure 2.4: Schematic of dark current generation mechanisms of the homojunction photodiode [54]. p+ and n- represent heavy p doping and light n doping, respectively. E_C, E_F and E_V are the conduction band edge, thermal equilibrium Fermi level and Valence band edge, respectively. SRH and TAT represent the SRH and trap assisted tunnelling processes, respectively. The band-to-band tunnelling process and the Auger generation processes are not included.

Dark currents in the T2SL photodiodes originate from the bulk and the surface. The primary bulk dark currents include diffusion, G-R, trap-assisted tunnelling (TAT) and band-to-band (BTB) tunnelling currents [54, 55]. Figure 2.4 illustrates the dark current mechanisms of a p-i-n photodiode, where the collector (or contact) is heavily doped with acceptors and the absorber is lightly doped with donors. The G-R current is caused by

generating electrons and holes associated with the SRH process within the p-n junction and drifting towards their respective sides. The BTB tunnelling current appears under high reverse bias conditions, where the electron directly tunnels through the junction into the conduction band. The TAT current is caused by the electron tunnelling through the junction indirectly through the trap states inside the junction. The diffusion current is due to the diffusion of minority carriers in the neutral regions generated via the SRH, Auger and radiative generation processes. For MWIR photodiodes operating at low temperatures, the major dark current is the G-R current, while diffusion current gradually becomes the dominant dark current at high temperatures ($\sim$ 130 -150 K) [56]. This is because the G-R dark current has a thermal activation energy equal to half of the bandgap energy, while the diffusion current has a thermal activation energy equal to the full bandgap energy. The surface current is due to the sudden termination of the periodic crystal structure at the semiconductor-air interface, resulting in a pinned Fermi level at the surface state level and band bending [57]. The band bending causes accumulation or type inversion of carriers, which produces a conductive path at the detector surface [58]. The surface current can have a very small activation energy (nearly independent of the temperature) and becomes more pronounced when the detector surface-to-volume ratio becomes larger [55].

Barrier detectors represent an important branch of the infrared photodetector technologies and can be embedded in many photodetector material systems for controlling the dark current. This thesis covers only a few examples of the unipolar barrier detector family, and more comprehensive introductions can be found in Refs. [59, 60] and references therein. An ideal barrier (B) should have a large band offset on the blocking side (e.g. conduction band offset for the electron barrier), and zero band offset on the other side. Early demonstrations of barrier detectors used the bulk ternary alloy, for example AlAsSb or AlGaSb [61, 62], as the electron barrier, and the composition and doping density must be carefully determined in order to minimise the valence band offset and band bending at the heterojunction interface [63]. Later, SL based barriers were adopted as

they have more tools for aligning the band offsets on both sides of the InAs/GaSb SLs, including InAs/GaAs SLs, GaSb/AlSb SLs, InAs/AlSb/GaSb SLs for electron blocking [64, 65] and InAs/AlSb SLs for hole blocking [66]. More hole blocking barriers, SL supercells, like InAs/InGaSb/InAs/AlInGaSb W-structure [65] and GaSb/InAs/GaSb/AlSb M-structure [67], named after the "W" shape and "M" shape band alignments, have been used in fabricating T2SL barrier detectors.

The unipolar barrier design implements an electron barrier (or a hole barrier) to impede the flow of electrons (or holes), while leaving the other unobstructed. The nBn barrier detector is a representative example of a unipolar barrier detector. In the case of the nBn design, an electron barrier is placed in between the n-type top contact and a lightly n-doped absorber, as shown in Figure 2.5 (a) [68]. This design aims to block the majority carrier flow (electrons) between the electrodes acting as a minority carrier (holes) device (conduction through minority carrier diffusion) [69]. Compared with the conventional pin photodiode, the nBn unipolar barrier detector has no depletion region, thus the G-R current occurring at the junction region is suppressed [70, 71]. With the reduced G-R current, the nBn detector can offer a similar performance at higher temperature to the conventional photodiodes. Replacing the n-type top contact with a p-type contact forms the pBn barrier photodiode. The barrier doping type determines the location of the depletion region. If the barrier doping type is the same as the absorber, the depletion region is located at the contact/barrier interface, otherwise, the depletion region can extend to the narrow bandgap absorber [72]. In the latter case, the doping density of the absorber has to be increased to reduce the width of depletion in the absorber region [73]. A common shortcoming of these detectors is the low QE due to the relatively low hole mobility [74].

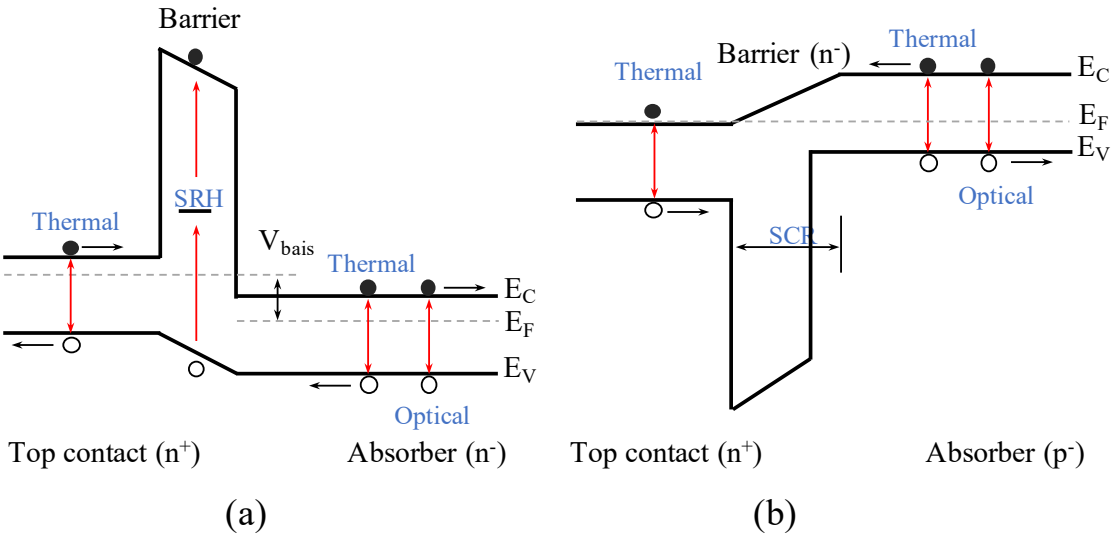

Figure 2.5: Schematics of (a) nBn unipolar barrier detector [73] and (b) nBp detector with hole blocking barrier [75]. The superscripts "+" and "-" stand for high doping density and low doping density, respectively; E_C, E_F and E_V are the conduction band edge, Fermi level and valence band edge, respectively. SCR indicates the of space charge region; V_{bias} is the external bias voltage.

To overcome the low hole mobility and the high power dissipation associated by the need for high external bias voltage, nBp photodiodes with a hole blocking barrier have been proposed [76]. The detector region was grown by the following sequence: a p-doped contact layer, a lightly p-doped absorber (i), a lightly n-doped hole barrier and a n-doped top contact, as partially displayed in Figure 2.5 (b). The absorber is intentionally p-doped to reduce the diffusion current ($\mathrm{J_{diff}} \propto 1/\mathrm{N_A}$) [77], as well as increase the electron mobility [78]. The barrier region is n-doped to reduce the band bending in the barrier and enable zero bias operation. However, the detector dark current still dominated by the G-R mechanism at low temperatures, since the p-n junction extends from the barrier into the narrow bandgap absorber [79].

The UCL MBE group published the first directly grown T2SL detector on a Si substrate, using a design based on an InAs/GaSb SL p-i-n photodiode [80]. The active region contains a 2 μm thick 10 monolayer (ML) InAs/10ML GaSb SLs, having a 50% cut-

off wavelength $\lambda_c \sim 5.5\ \mu$m (70 K) and corresponding to a peak detectivity of 1.3×10^9 $\mathrm{cm} \cdot \mathrm{Hz}^{1/2}/\mathrm{W}$ at -0.1 V. Recently, researchers from Lancaster University and Coventry University demonstrated an InAs/InAsSb SL based nBn detector with a 100 nm bulk AlGaAsSb electron barrier [81]. The detector ($\lambda_c \sim 5.5\ \mu$m) exhibited an external QE of $\sim$25.6% and a peak detectivity $3.65 \times 10^{10}\ \mathrm{cm} \cdot \mathrm{Hz}^{1/2}/\mathrm{W}$ at 200 K [81].

2.3 Self-assembled Quantum Dot Fabrication Method

2.3.1 Molecular Beam Epitaxy System

Epitaxy refers to deposition of material on a crystalline substrate with the same crystal lattice orientation. There are several epitaxy technologies, for example, molecular beam epitaxy (MBE), metal-organic chemical vapour deposition (MOCVD), liquid phase epitaxy, etc. Figure 2.6 is a simplified illustration of the MBE chamber. The effusion cells, facing towards the substrate, are heated by the heating coils generating molecular beam flux by evaporation. The growth chamber is constantly maintained at ultra-high vacuum conditions ($\sim 10^{-10}$ Torr depending on the system manufacturer). Under ultra-high vacuum conditions, particles can travel a long distance before collisions (mean free path), so it is possible to implement a mechanical shutter to accurately control the beam flux [82]. Through manipulation of beam fluxes by shutters, in association with the operational temperature of the cells, the composition and doping of the deposited layers can be precisely controlled. In addition, the ultra-high vacuum also ensures a low level of contamination by residual species, like carbon and oxygen, and growth of high-purity materials [83]. A reflection high energy electron diffraction (RHEED) system can be used to monitor the growth rate and surface structure with atomic-level accuracy.

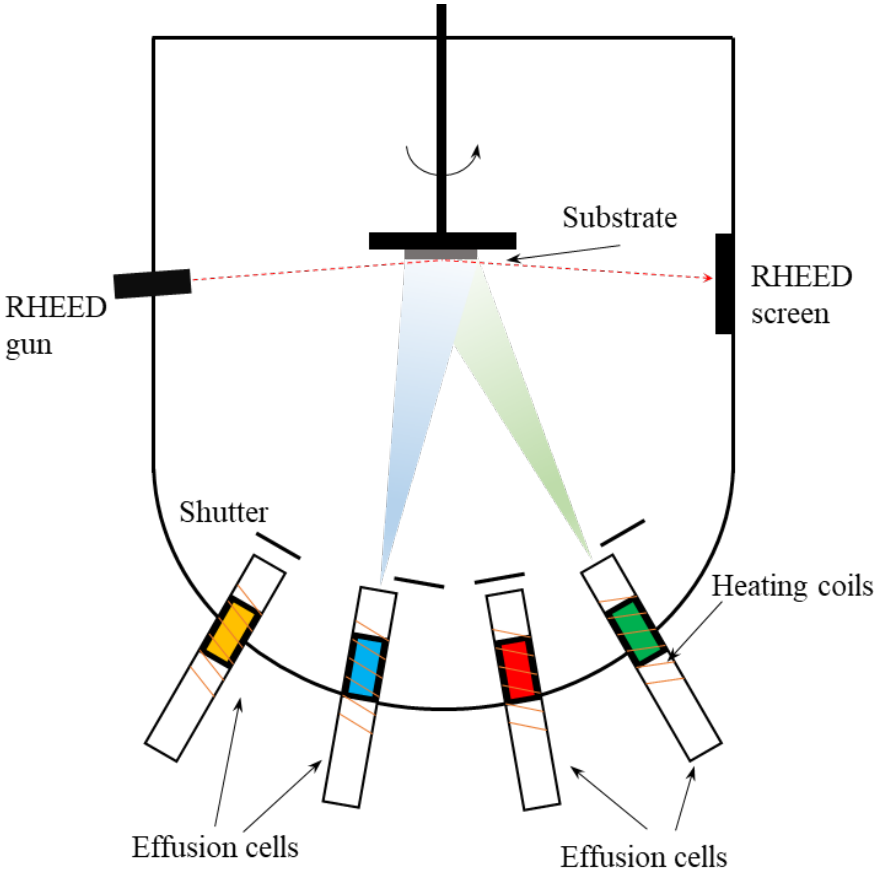

Figure 2.6: Schematic diagram of an MBE growth Chamber.

2.3.2 Self-assembled QDs via Stranski-Krastanov Growth Mode

Early QD fabrication techniques, such as electron beam lithography followed by dry etching, selective area growth, etc., failed due to poor QD quality. In contrast, self-assembled QDs through the Stranski-Krastanov (S-K) growth mode offer a defect-free and highly reliable approach to fabricating the QDs [84]. The S-K growth mode, also known as the layer-plus-islands growth mode, involves heteroepitaxial growth of the QD material on a lattice-mismatched substrate material. The initial layers of QD material form a 2D wetting layer. After the thickness of the wetting layer reaches a critical value, the onset of 3D islands (or QDs) growth occurs in order to release the accumulated strain energy [84].

Figure 2.7 (a) shows a cross-section view of an S-K QD. The QD has a lens or pyramid shape with a height of about 5 nm and a base diameter about 25 nm. The S-K QDs can produce 3D quantum confinement to the carriers with appropriate material selection, for example narrow bandgap InAs QDs buried in wide bandgap GaAs matrix [85]. Figure 2.7 (b) shows the surface morphology of the S-K QDs without capping. The QDs are randomly distributed with various heights on the surface.

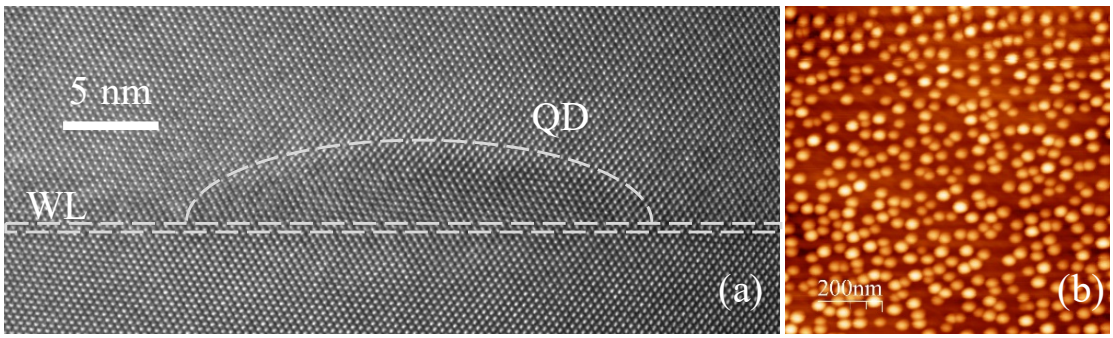

Figure 2.7: (a) Cross-sectional view of the high resolution transmission electron microscopy image of a S-K QD and (b) atomic force microscopy image of the S-K QDs.

2.3.3 QDs Fabrication with Sub-monolayer Deposition

QDs formed by sub-monolayer deposition are one of the alternatives to S-K QDs. SML QDs are formed by alternating deposition of less than one ML of a dot material and more than one ML of barrier (spacing) material. The SML QD is formed by the composition nonuniformity during the SML deposition [86]. The sheet density of SML QDs can exceed 10^{11} dots/cm^2 and even reach the level of 10^{12} dots/cm^2, which is more than 10 times higher than the sheet density of SK QD [87]. SML QDs have been demonstrated in laser [88], solar cell [89] and SML QDIP [90] devices.

2.4 Direct Growth III-V Virtual Substrate on Si at UCL MBE Group

2.4.1 Antiphase Domain Suppression

Conventional Si substrates cut along the (001) facet contain monoatomic (one atomic layer height) steps [91]. Direct growth of polar III-V materials on monoatomic stepped Si substrates tends to lead to the formation of antiphase domains (APDs), as illustrated in Figure 2.8 (a). The red solid lines represent the antiphase boundaries, which separate the antiphase domains. Surrounding each antiphase boundary, there are two different domains with opposite sub-lattice orientations. APD formation is not a special case initiated at the

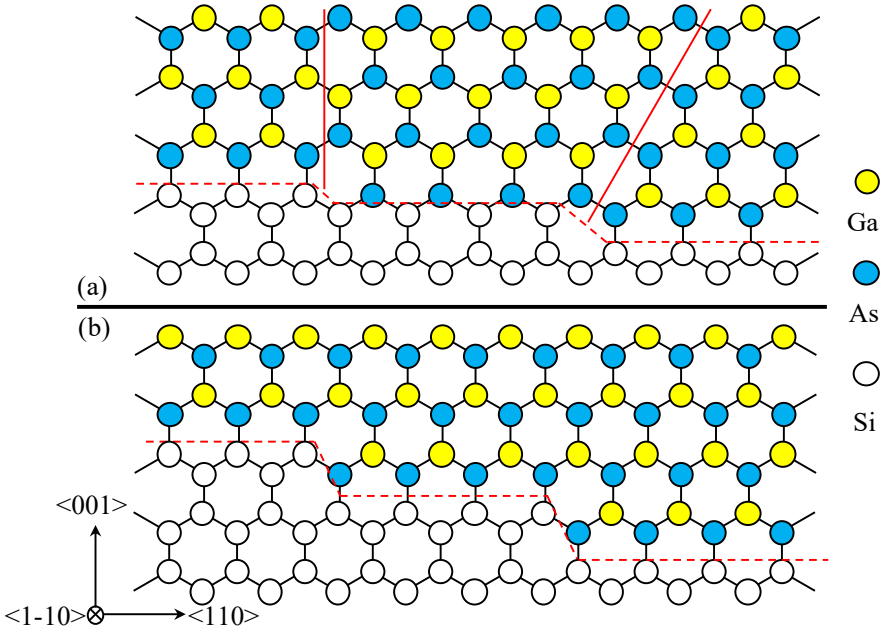

Figure 2.8: Schematic cross-sectional view of (a) GaAs on monoatomic stepped Si (001) with APDs and (b) GaAs on double atomic stepped Si (001) without APDs. The dotted red lines and solid red lines represent the GaAs/Si interfaces and the antiphase boundaries, respectively.

III-V and monoatomic Si (001) interface; it appears at any Si (001) surface with an odd

number of atomic steps [92]. A double atomic stepped (or step doubling) Si (001) surface can effectively suppress the formation of APDs. The suppression mechanism of double atomic stepped Si is to create the same Si sub-lattices at the Si (001) surface, and hence suppress the inversion of sub-lattices in the GaAs layer. To create the double atomic steps on the Si (001) surface, an intentional 2-6° offcut is made when cutting the Si ingot. Figure 2.8 (b) depicts the deposition of GaAs on a double atomic stepped Si (001) surface, resulting in a layer that is free of APDs. Many groups have reported APD-free III-Vs on mis-orientated Si (001) substrates, for example, a 4° offcut towards the [011] direction [93] and a 6° offcut towards the [111] direction [94]. However, the mis-orientated Si wafer is not compatible with the CMOS industry. APD-free III-V devices on exact Si (001) have been reported in recent years, such as MOCVD assisted GaP on Si (001) [95], GaAs on Si (001) [96, 97] and other examples [98].

2.4.2 Threading Dislocation Reduction

Another problem originating from the GaAs/Si interface is the presence of misfit dislocations (MDs) and threading dislocations (TDs) due to the $\sim$4% lattice mismatch between GaAs and Si. MDs are localised at the GaAs/Si interface, while TDs can propagate along the growth direction and enter the device region, thereby introducing defect states in the forbidden gap. A proper GaAs buffer design can help in reducing the TD density. At the UCL MBE group, the GaAs buffer is grown in two steps with different temperatures, a thin nucleation layer grown at low temperature followed by a thick 1000 nm buffer grown at high temperature. Due to the lattice mismatch, the onset of GaAs islands occurs at the early stage of the growth. With high-temperature nucleation (around 590 °C for GaAs or AlAs), high-mobility GaAs tends to coalesce and form inhomogeneous defective islands. The coalescing of these islands can introduce additional defects and a rough surface, Figure 2.9 (a). With low temperature nucleation growth (around 400 °C for GaAs or AlAs), the diffusion length of adatoms is small and the growth tends to form smaller but dense

islands, which can lead to a relatively smooth surface and leads to fewer defects in the subsequent layers, Figure 2.9 (b). Lee et al. found a 5 nm AlAs initial layer can lead to even smoother nucleation surface and provide better material quality and device performance than the GaAs initial layer [99]. This could be attributed to the shorter diffusion length of Al than Ga [100].

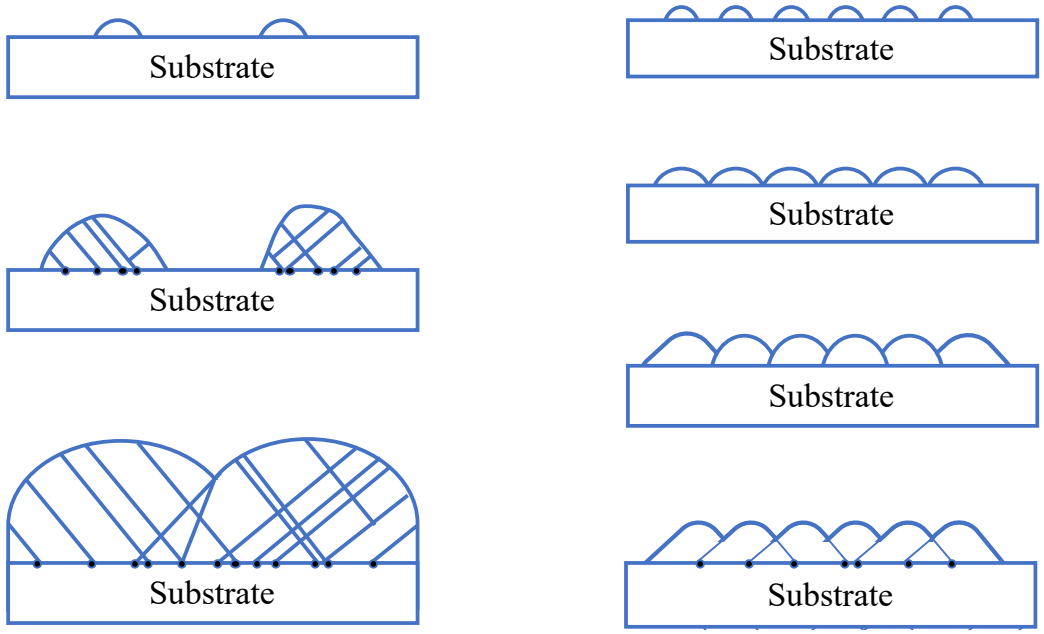

(a) Nucleation at high temperature (b) Nucleation at low temperature

Figure 2.9: Schematics of (a) High temperature growth nucleation layer and (b) low temperature growth nucleation layer [101].

After the surface is covered with the thin nucleation layer, high-temperature growth of a thick GaAs buffer is preferred in order to obtain a high-quality, single-crystal GaAs epitaxial layer (epi-layer). Moreover, the high-temperature growth conditions enhance the movement of TDs and increase the interaction between the TDs. Two TDs with opposite Burgers vectors[2] tend to attract and annihilate. After the GaAs buffer layer, further TD reduction can be achieved by implementing SLSs as the dislocation filter-

[2]Burgers vector is a vector representing the atomic displacement that occurs when a dislocation moves.

ing layers (DFLs) [32]. The SLSs DFLs are grown by alternating the deposition of two slightly lattice-mismatched semiconductors, for example, $\mathrm{In_{0.15}Ga_{0.85}As}$ and GaAs, with the same thickness, so that the layers alternate between compressive and tensile strains; in the meantime, the thickness of each constituent layer is required not to exceed the critical thickness for generating new TDs. The SLSs DFL can enhance the horizontal motions of TDs. The enhanced horizontal motion increases the interactions between the TDs as well as the annihilation probability. During the growth, a series of thermal annealing processes is performed to enhance the dislocation motion for dislocation reduction.

2.4.3 Interfacial Misfit Growth Technique

The lattice constant mismatch between the 6.1 Å family, e.g. AlSb, GaSb, and Si (GaAs) is about 13% ($\sim$7.8%) [102], which is larger than the lattice mismatch between GaAs and Si ($\sim$4%). Such high strain energy can be accommodated by using a thick metamorphic buffer or interfacial misfit (IMF) dislocation array [103]. The IMF growth technique, which is driven by strain energy minimisation [102] and depends on growth conditions, has been studied by several groups. Experimental measurement has shown that using the IMF growth technique can offset about 98.5% of the strain energy with a thin GaSb layer on GaAs substrate [104]. IMF contains 90° MDs spreading along the [110] and [1-10] directions at the substrate/epi-layer interface, which do not trigger vertically propagated threading dislocations [105]. However, depending on the growth condition, 60° MDs can co-exist with 90° MDs [106]. Unlike the "harmless" 90° MDs, the 60° MDs can evolve into TDs. Wang et al. explained that the origin of 60° MDs is mainly due to imperfections in the periodicity [107]. A similar explanation by Kang et al. pointed out that the abnormally large and irregularly shaped islands are responsible for the 60° MDs [108]. Huang et al. measured the IMF periodicity to be $\sim$ 3.46 nm at the AlSb/Si interface, which corresponds to 8 AlSb lattice sites overlaying with 9 Si lattice sites [109]. For a GaSb/GaAs system, if the periodicity is about 5.51 nm, corresponding to 13 GaSb

lattice sites on 14 GaAs lattice sites, the strain can be fully relaxed [102]. III-Sb devices on Si have been reported using the IMF technique, such as an InGaAsSb/AlGaAsSb laser [110], an InSb detector [111] and the previously mentioned T2SL detectors [80, 81].

2.5 Chapter Summary

This chapter has given a brief introduction to the photodetector technologies that will be studied in this thesis, and the challenges to further improving the performance. For the QD based intersubband photodetectors, the major challenges will be the low absorption associated with the QDs. Improving the QD uniformity is desired to increase absorption QE. For T2SL based detectors, improving material quality, e.g. preventing SL intermixing, and controlling surface leakage current are key factors to obtain further improvement. In addition, the III-V buffer techniques on Si employed by the UCL MBE group were also introduced at the end of this chapter. Later we will see that by utilising optimal buffer growth, the TD density will be reduced to $\sim 10^6 - 10^7\ \mathrm{cm}^{-2}$.

2.6 Contribution Statement

Figure 2.7 (a) was provided by Dr. Yuriy Mazur, University of Arkansas.

References

[1] P. Martyniuk and A. Rogalski, "Quantum-dot infrared photodetectors: Status and outlook," *Progress in Quantum Electronics*, vol. 32, no. 3-4, pp. 89–120, 2008.

[2] A. Ren *et al.*, "Recent progress of III-V quantum dot infrared photodetectors on silicon," *Journal of Materials Chemistry C*, vol. 7, no. 46, pp. 14441–14453, 2019.

[3] C.-C. Chang *et al.*, "A Surface Plasmon Enhanced Infrared Photodetector Based on InAs Quantum Dots," *Nano Letters*, vol. 10, no. 5, pp. 1704–1709, 2010.

[4] Y. Arakawa and H. Sakaki, "Multidimensional quantum well laser and temperature dependence of its threshold current," *Applied Physics Letters*, vol. 40, no. 11, pp. 939–941, 1982.

[5] H. C. Liu *et al.*, "Quantum dot infrared photodetectors," *Applied Physics Letters*, vol. 78, no. 1, pp. 79–81, 2001.

[6] Z. Ye *et al.*, "Noise and photoconductive gain in InAs quantum-dot infrared photodetectors," *Applied Physics Letters*, vol. 83, no. 6, pp. 1234–1236, 2003.

[7] J. Wu, S. Chen, A. Seeds, and H. Liu, "Quantum dot optoelectronic devices: lasers, photodetectors and solar cells," *Journal of Physics D: Applied Physics*, vol. 48, no. 36, p. 363001, 2015.

[8] A. V. Barve *et al.*, "High temperature operation of quantum dots-in-a-well infrared photodetectors," *Infrared Physics & Technology*, vol. 54, no. 3, pp. 215–219, 2011.

[9] A. Barve, S. Lee, S. Noh, and S. Krishna, "Review of current progress in quantum dot infrared photodetectors," *Laser & Photonics Reviews*, vol. 4, no. 6, pp. 738–750, 2009.

[10] S. Wolde *et al.*, "Noise, gain, and capture probability of p-type InAs-GaAs quantum-dot and quantum dot-in-well infrared photodetectors," *Journal of Applied Physics*, vol. 121, no. 24, p. 244501, 2017.

[11] J.-Y. Duboz, H. C. Liu, Z. R. Wasilewski, M. Byloss, and R. Dudek, "Tunnel current in quantum dot infrared photodetectors," *Journal of Applied Physics*, vol. 93, no. 2, pp. 1320–1322, 2003.

[12] A. D. Stiff, S. Krishna, P. Bhattacharya, and S. Kennerly, "High-detectivity, normal-incidence, mid-infrared ($\lambda \sim 4\ \mu m$)InAs/GaAs quantum-dot detector operating at 150 K," *Applied Physics Letters*, vol. 79, no. 3, pp. 421–423, 2001.

[13] S. Y. Wang, S. D. Lin, H. W. Wu, and C. P. Lee, "Low dark current quantum-dot infrared photodetectors with an AlGaAs current blocking layer," *Applied Physics Letters*, vol. 78, no. 8, pp. 1023–1025, 2001.

[14] S.-F. Tang, S.-Y. Lin, and S.-C. Lee, "Near-room-temperature operation of an InAs/GaAs quantum-dot infrared photodetector," *Applied Physics Letters*, vol. 78, no. 17, pp. 2428–2430, 2001.

[15] X. Su, S. Chakrabarti, P. Bhattacharya, G. Ariyawansa, and A. Perera, "A resonant tunneling quantum-dot infrared photodetector," *IEEE Journal of Quantum Electronics*, vol. 41, no. 7, pp. 974–979, 2005.

[16] A. Barve *et al.*, "Resonant Tunneling Barriers in Quantum Dots-in-a-Well Infrared Photodetectors," *IEEE Journal of Quantum Electronics*, vol. 46, no. 7, pp. 1105–1114, 2010.

[17] J. Phillips, "Evaluation of the fundamental properties of quantum dot infrared detectors," *Journal of Applied Physics*, vol. 91, no. 7, pp. 4590–4594, 2002.

[18] E.-T. Kim, A. Madhukar, Z. Ye, and J. C. Campbell, "High detectivity InAs quantum dot infrared photodetectors," *Applied Physics Letters*, vol. 84, no. 17, pp. 3277–3279, 2004.

[19] R. S. Attaluri, S. Annamalai, K. T. Posani, A. Stintz, and S. Krishna, "Effects of Si doping on normal incidence InAs/$\mathrm{In_{0.15}Ga_{0.85}As}$ dots-in-well quantum dot infrared photodetectors," *Journal of Applied Physics*, vol. 99, no. 8, p. 083105, 2006.

[20] S. Chakrabarti *et al.*, "High-Temperature Operation of InAs/GaAs Quantum-Dot Infrared Photodetectors With Large Responsivity and Detectivity," *IEEE Photonics Technology Letters*, vol. 16, no. 5, pp. 1361–1363, 2004.

[21] S. Krishna, "Quantum dots-in-a-well infrared photodetectors," *Journal of Physics D: Applied Physics*, vol. 38, no. 13, pp. 2142–2150, 2005.

[22] S. Krishna *et al.*, "Two color InAs/InGaAs dots-in-a-well detector with background-limited performance at 91 K," *Applied Physics Letters*, vol. 82, no. 16, pp. 2574–2576, 2003.

[23] S. Raghavan *et al.*, "High-responsivity, normal-incidence long-wave infrared ($\lambda \sim 7.2\mu$m) InAs/$\mathrm{In_{0.15}Ga_{0.85}As}$ dots-in-a-well detector," *Applied Physics Letters*, vol. 81, no. 8, pp. 1369–1371, 2002.

[24] S. Krishna *et al.*, "Three-color ($\lambda_{p1} \sim 3.8\ \mu m$,$\lambda_{p2} \sim 8.5\ \mu m$,$\lambda_{p3} \sim 23.2\ \mu m$) InAs/InGaAs quantum-dots-in-a-well detector," *Applied Physics Letters*, vol. 83, no. 14, pp. 2745–2747, 2003.

[25] H. Lim, S. Tsao, W. Zhang, and M. Razeghi, "High-performance InAs quantum-dot infrared photodetectors grown on InP substrate operating at room temperature," *Applied Physics Letters*, vol. 90, no. 13, p. 131112, 2007.

[26] J. Phillips, K. Kamath, and P. Bhattacharya, "Far-infrared photoconductivity in self-organized InAs quantum dots," *Applied Physics Letters*, vol. 72, no. 16, pp. 2020–2022, 1998.

[27] D. Pan, E. Towe, and S. Kennerly, "Normal-incidence intersubband (In, Ga)As/GaAs quantum dot infrared photodetectors," *Applied Physics Letters*, vol. 73, no. 14, pp. 1937–1939, 1998.

[28] S. Kim, H. Mohseni, M. Erdtmann, E. Michel, C. Jelen, and M. Razeghi, "Growth and characterization of InGaAs/InGaP quantum dots for midinfrared photoconductive detector," *Applied Physics Letters*, vol. 73, no. 7, pp. 963–965, 1998.

[29] S. Krishna *et al.*, "Demonstration of a 320 $\times$ 256 two-color focal plane array using InAs/InGaAs quantum dots in well detectors," *Applied Physics Letters*, vol. 86, no. 19, p. 193501, 2005.

[30] S. D. Gunapala *et al.*, "640$\times$512 pixels long-wavelength infrared (LWIR) quantum-dot infrared photodetector (QDIP) imaging focal plane array," *IEEE Journal of Quantum Electronics*, vol. 43, no. 3, pp. 230–237, 2007.

[31] S. Tsao, H. Lim, W. Zhang, and M. Razeghi, "High operating temperature 320 $\times$ 256 middle-wavelength infrared focal plane array imaging based on an InAs/InGaAs/InAlAs/InP quantum dot infrared photodetector," *Applied Physics Letters*, vol. 90, no. 20, p. 201109, 2007.

[32] J. Wu *et al.*, "Monolithically Integrated InAs/GaAs Quantum Dot Mid-Infrared Photodetectors on Silicon Substrates," *ACS Photonics*, vol. 3, no. 5, pp. 749–753, 2016.

[33] D. Guo *et al.*, "Two-colour $\mathrm{In_{0.5}Ga_{0.5}As}$ quantum dot infrared photodetectors on silicon," *Semiconductor Science and Technology*, vol. 33, no. 9, p. 094009, 2018.

[34] W. Chen *et al.*, "Demonstration of InAs/InGaAs/GaAs Quantum Dots-in-a-Well Mid-Wave Infrared Photodetectors Grown on Silicon Substrate," *Journal of Lightwave Technology*, vol. 36, no. 13, pp. 2572–2581, 2018.

[35] J. Faist *et al.*, "Quantum cascade laser," *Science*, vol. 264, no. 5158, pp. 553–556, 1994.

[36] D. Hofstetter, M. Beck, and J. Faist, "Quantum-cascade-laser structures as photodetectors," *Applied Physics Letters*, vol. 81, no. 15, pp. 2683–2685, 2002.

[37] B. Schwarz *et al.*, "Watt-level continuous-wave emission from a bifunctional quantum cascade laser/detector," *ACS Photonics*, vol. 4, no. 5, pp. 1225–1231, 2017.

[38] L. Gendron, M. Carras, A. Huynh, V. Ortiz, C. Koeniguer, and V. Berger, "Quantum cascade photodetector," *Applied Physics Letters*, vol. 85, no. 14, pp. 2824–2826, 2004.

[39] A. Delga *et al.*, "Performances of quantum cascade detectors," *Infrared Physics & Technology*, vol. 59, pp. 100–107, 2013.

[40] F. R. Giorgetta *et al.*, "Quantum cascade detectors," *IEEE Journal of Quantum Electronics*, vol. 45, no. 8, pp. 1039–1052, 2009.

[41] T. Dougakiuchi *et al.*, "High photoresponse in room temperature quantum cascade detector based on coupled quantum well design," *Applied Physics Letters*, vol. 109, no. 26, p. 261107, 2016.

[42] M. A. Kinch, "Fundamental physics of infrared detector materials," *Journal of Electronic Materials*, vol. 29, no. 6, pp. 809–817, 2000.

[43] J. Liu *et al.*, "High resistance AlGaAs/GaAs quantum cascade detectors grown by solid source molecular beam epitaxy operating above liquid nitrogen temperature," *Semiconductor Science and Technology*, vol. 25, no. 7, p. 075011, 2010.

[44] A. V. Barve and S. Krishna, "Photovoltaic quantum dot quantum cascade infrared photodetector," *Applied Physics Letters*, vol. 100, no. 2, p. 021105, 2012.

[45] X.-J. Wang *et al.*, "Quantum dot quantum cascade infrared photodetector," *Applied Physics Letters*, vol. 104, no. 17, p. 171108, 2014.

[46] J. Huang *et al.*, "Sub-monolayer quantum dot quantum cascade mid-infrared photodetector," *Applied Physics Letters*, vol. 111, no. 25, p. 251104, 2017.

[47] J. Huang *et al.*, "Midwave Infrared Quantum Dot Quantum Cascade Photodetector Monolithically Grown on Silicon Substrate," *Journal of Lightwave Technology*, vol. 36, no. 18, pp. 4033–4038, 2018.

[48] A. Rogalski, P. Martyniuk, and M. Kopytko, "InAs/GaSb type-II superlattice infrared detectors: Future prospect," *Applied Physics Reviews*, vol. 4, no. 3, p. 031304, 2017.

[49] M. Razeghi and B.-M. Nguyen, "Advances in mid-infrared detection and imaging: a key issues review," *Reports on Progress in Physics*, vol. 77, no. 8, p. 082401, 2014.

[50] A. K. Sood *et al.*, "Design and development of two-dimensional strained layer superlattice (SLS) detector arrays for IR applications," in *Two-dimensional Materials for Photodetector*, InTech, 2018.

[51] D. Z.-Y. Ting *et al.*, "Type-II superlattice infrared detectors," in *Advances in Infrared Photodetectors*, pp. 1–57, Elsevier, 2011.

[52] D. L. Smith and C. Mailhiot, "Proposal for strained type-II superlattice infrared detectors," *Journal of Applied Physics*, vol. 62, no. 6, pp. 2545–2548, 1987.

[53] E. R. Youngdale *et al.*, "Auger lifetime enhancement in InAs/$\mathrm{Ga_{1-x}In_xSb}$ superlattices," *Applied Physics Letters*, vol. 64, no. 23, pp. 3160–3162, 1994.

[54] D. R. Rhiger, "Performance comparison of long-wavelength infrared type-II superlattice devices with HgCdTe," *Journal of Electronic Materials*, vol. 40, no. 8, pp. 1815–1822, 2011.

[55] B. T. Marozas *et al.*, "Surface dark current mechanisms in III-V infrared photodetectors [invited]," *Optical Materials Express*, vol. 8, no. 6, p. 1419, 2018.

[56] J. Wang *et al.*, "Temperature dependence characteristics of dark current for arsenic doped LWIR HgCdTe detectors," *Infrared Physics & Technology*, vol. 61, pp. 157–161, 2013.

[57] E. Plis *et al.*, "Passivation of long-wave infrared InAs/GaSb strained layer superlattice detectors," *Infrared Physics & Technology*, vol. 54, no. 3, pp. 252–257, 2011.

[58] G. Chen, B.-M. Nguyen, A. M. Hoang, E. K. Huang, S. R. Darvish, and M. Razeghi, "Elimination of surface leakage in gate controlled type-II InAs/GaSb mid-infrared photodetectors," *Applied Physics Letters*, vol. 99, no. 18, p. 183503, 2011.

[59] P. Martyniuk, M. Kopytko, and A. Rogalski, "Barrier infrared detectors," *Opto-Electronics Review*, vol. 22, no. 2, 2014.

[60] D. Z. Ting *et al.*, "Antimonide-based barrier infrared detectors," in *Infrared Technology and Applications XXXVI* (B. F. Andresen, G. F. Fulop, and P. R. Norton, eds.), SPIE, 2010.

[61] J. B. Rodriguez *et al.*, "nBn structure based on InAs/GaSb type-II strained layer superlattices," *Applied Physics Letters*, vol. 91, no. 4, p. 043514, 2007.

[62] S. Maimon and G. W. Wicks, "nBn detector, an infrared detector with reduced dark current and higher operating temperature," *Applied Physics Letters*, vol. 89, no. 15, p. 151109, 2006.

[63] A. D. Hood, A. J. Evans, A. Ikhlassi, D. L. Lee, and W. E. Tennant, "LWIR Strained-Layer Superlattice Materials and Devices at Teledyne Imaging Sensors," *Journal of Electronic Materials*, vol. 39, no. 7, pp. 1001–1006, 2010.

[64] B.-M. Nguyen, D. Hoffman, E. K. Huang, P.-Y. Delaunay, and M. Razeghi, "Background limited long wavelength infrared type-II InAs/GaSb superlattice photodiodes operating at 110 K," *Applied Physics Letters*, vol. 93, no. 12, p. 123502, 2008.

[65] C. Canedy *et al.*, "Antimonide type-II W photodiodes with long-wave infrared $\mathrm{R_0A}$ comparable to HgCdTe," *Journal of Electronic Materials*, vol. 36, no. 8, pp. 852–856, 2007.

[66] N. Gautam *et al.*, "Three color infrared detector using InAs/GaSb superlattices with unipolar barriers," *Applied Physics Letters*, vol. 98, no. 12, p. 121106, 2011.

[67] B.-M. Nguyen, D. Hoffman, P.-Y. Delaunay, and M. Razeghi, "Dark current suppression in type-II InAs/GaSb superlattice long wavelength infrared photodiodes with M-structure barrier," *Applied Physics Letters*, vol. 91, no. 16, p. 163511, 2007.

[68] G. R. Savich, J. R. Pedrazzani, D. E. Sidor, S. Maimon, and G. W. Wicks, "Use of unipolar barriers to block dark currents in infrared detectors," in *Infrared Technology and Applications XXXVII* (B. F. Andresen, G. F. Fulop, and P. R. Norton, eds.), SPIE, 2011.

[69] A. Khoshakhlagh *et al.*, "Bias dependent dual band response from InAs/Ga(In)Sb type-II strain layer superlattice detectors," *Applied Physics Letters*, vol. 91, no. 26, p. 263504, 2007.

[70] A. Khoshakhlagh *et al.*, "Mid-wavelength InAsSb detectors based on nBn design," in *Infrared Technology and Applications XXXVI* (B. F. Andresen, G. F. Fulop, and P. R. Norton, eds.), SPIE, 2010.

[71] D. Z. Ting *et al.*, "Development of InAs/InAsSb type-II strained-layer superlattice unipolar barrier infrared detectors," *Journal of Electronic Materials*, vol. 48, no. 10, pp. 6145–6151, 2019.

[72] P. Klipstein, "XB n barrier photodetectors for high sensitivity and high operating temperature infrared sensors," in *Infrared Technology and Applications XXXIV* (B. F. Andresen, G. F. Fulop, and P. R. Norton, eds.), SPIE, 2008.

[73] P. Klipstein, "XBn barrier photodetectors based on InAsSb with high operating temperatures," *Optical Engineering*, vol. 50, no. 6, p. 061002, 2011.

[74] B.-M. Nguyen, S. Bogdanov, S. A. Pour, and M. Razeghi, "Minority electron unipolar photodetectors based on type-II InAs/GaSb/AlSb superlattices for very long wavelength infrared detection," *Applied Physics Letters*, vol. 95, no. 18, p. 183502, 2009.

[75] Z. Deng *et al.*, "Mid-wave infrared InAs/GaSb type-II superlattice photodetector with n-b-p design grown on GaAs substrate," *IEEE Journal of Quantum Electronics*, vol. 55, no. 4, pp. 1–5, 2019.

[76] Z. Taghipour *et al.*, "Extraction of minority carrier diffusion length of MWIR type-II superlattice nBp detector," in *Infrared Sensors, Devices, and Applications VII* (P. D. LeVan, A. K. Sood, P. Wijewarnasuriya, and A. I. D'Souza, eds.), SPIE, 2017.

[77] J. Huang *et al.*, "Defect Characterization of InAs/InGaAs Quantum Dot p-i-n Photodetector Grown on GaAs-on-V-Grooved-Si Substrate," *ACS Photonics*, vol. 6, no. 5, pp. 1100–1105, 2019.

[78] M. Kopytko and A. Rogalski, "HgCdTe barrier infrared detectors," *Progress in Quantum Electronics*, vol. 47, pp. 1–18, 2016.

[79] A. Kazemi *et al.*, "Mid-wavelength infrared unipolar nBp superlattice photodetector," *Infrared Physics & Technology*, vol. 88, pp. 114–118, 2018.

[80] C. G. Burguete *et al.*, "Direct growth of InAs/GaSb type-II superlattice photodiodes on silicon substrates," *IET Optoelectronics*, vol. 12, no. 1, pp. 2–4, 2018.

[81] E. Delli *et al.*, "Mid-infrared InAs/InAsSb superlattice nBn photodetector monolithically integrated onto silicon," *ACS Photonics*, vol. 6, no. 2, pp. 538–544, 2019.

[82] H. Asahi, *Molecular beam epitaxy : materials and applications for electronics and optoelectronics*. Hoboken, NJ: John Wiley & Sons, Inc, 2019.

[83] R. F. C. Farrow, *Molecular beam epitaxy : applications to key materials*. Park Ridge, N.J: Noyes Publications, 1995.

[84] D. J. Eaglesham and M. Cerullo, "Dislocation-free Stranski-Krastanow growth of Ge on Si(100)," *Physical Review Letters*, vol. 64, no. 16, pp. 1943–1946, 1990.

[85] G. Medeiros-Ribeiro, D. Leonard, and P. M. Petroff, "Electron and hole energy levels in InAs self-assembled quantum dots," *Applied Physics Letters*, vol. 66, no. 14, pp. 1767–1769, 1995.

[86] S. Krishna *et al.*, "Structural and luminescence characteristics of cycled submonolayer InAs/GaAs quantum dots with room-temperature emission at 1.3 μm," *Journal of Applied Physics*, vol. 86, no. 11, pp. 6135–6138, 1999.

[87] Z. Xu *et al.*, "Structure and optical anisotropy of vertically correlated submonolayer InAs/GaAs quantum dots," *Applied Physics Letters*, vol. 82, no. 22, pp. 3859–3861, 2003.

[88] F. Hopfer *et al.*, "Single-mode submonolayer quantum-dot vertical-cavity surface-emitting lasers with high modulation bandwidth," *Applied Physics Letters*, vol. 89, no. 14, p. 141106, 2006.

[89] P. Lam *et al.*, "Submonolayer InGaAs/GaAs quantum dot solar cells," *Solar Energy Materials and Solar Cells*, vol. 126, pp. 83–87, 2014.

[90] D. Z.-Y. Ting *et al.*, "Submonolayer quantum dot infrared photodetector," *Applied Physics Letters*, vol. 94, no. 11, p. 111107, 2009.

[91] B. Kunert, I. Németh, S. Reinhard, K. Volz, and W. Stolz, "Si (001) surface preparation for the antiphase domain free heteroepitaxial growth of GaP on Si substrate," *Thin Solid Films*, vol. 517, no. 1, pp. 140–143, 2008.

[92] H. Kroemer, "Polar-on-nonpolar epitaxy," *Journal of Crystal Growth*, vol. 81, no. 1-4, pp. 193–204, 1987.

[93] S. Chen *et al.*, "Electrically pumped continuous-wave III-V quantum dot lasers on silicon," *Nature Photonics*, vol. 10, no. 5, pp. 307–311, 2016.

[94] A. Y. Liu *et al.*, "High performance continuous wave 1.3 μm quantum dot lasers on silicon," *Applied Physics Letters*, vol. 104, no. 4, p. 041104, 2014.

[95] D. Jung, P. G. Callahan, B. Shin, K. Mukherjee, A. C. Gossard, and J. E. Bowers, "Low threading dislocation density GaAs growth on on-axis GaP/Si (001)," *Journal of Applied Physics*, vol. 122, no. 22, p. 225703, 2017.

[96] S. Chen *et al.*, "Electrically pumped continuous-wave 1.3 μm InAs/GaAs quantum dot lasers monolithically grown on on-axis Si (001) substrates," *Optics Express*, vol. 25, no. 5, p. 4632, 2017.

[97] R. Alcotte *et al.*, "Epitaxial growth of antiphase boundary free GaAs layer on 300 mm Si(001) substrate by metalorganic chemical vapour deposition with high mobility," *APL Materials*, vol. 4, no. 4, p. 046101, 2016.

[98] L. Desplanque *et al.*, "Monolithic integration of high electron mobility InAs-based heterostructure on exact (001) silicon using a GaSb/GaP accommodation layer," *Applied Physics Letters*, vol. 101, no. 14, p. 142111, 2012.

[99] A. D. Lee *et al.*, "InAs/GaAs Quantum-Dot Lasers Monolithically Grown on Si, Ge, and Ge-on-Si Substrates," *IEEE Journal of Selected Topics in Quantum Electronics*, vol. 19, no. 4, pp. 1901107–1901107, 2013.

[100] S. H. Vajargah, S. Ghanad-Tavakoli, J. S. Preston, R. N. Kleiman, and G. A. Botton, "Growth mechanisms of GaSb heteroepitaxial films on Si with an AlSb buffer layer," *Journal of Applied Physics*, vol. 114, no. 11, p. 113101, 2013.

[101] Y. B. Bolkhovityanov and O. P. Pchelyakov, "GaAs epitaxy on si substrates: modern status of research and engineering," *Physics-Uspekhi*, vol. 51, no. 5, pp. 437–456, 2008.

[102] A. Jallipalli, G. Balakrishnan, S. Huang, A. Khoshakhlagh, L. Dawson, and D. Huffaker, "Atomistic modeling of strain distribution in self-assembled interfacial misfit dislocation (IMF) arrays in highly mismatched III-Vsemiconductor materials," *Journal of Crystal Growth*, vol. 303, no. 2, pp. 449–455, 2007.

[103] P. E. Hopkins *et al.*, "Effect of dislocation density on thermal boundary conductance across GaSb/GaAs interfaces," *Applied Physics Letters*, vol. 98, no. 16, p. 161913, 2011.

[104] S. H. Huang, G. Balakrishnan, A. Khoshakhlagh, A. Jallipalli, L. R. Dawson, and D. L. Huffaker, "Strain relief by periodic misfit arrays for low defect density GaSb on GaAs," *Applied Physics Letters*, vol. 88, no. 13, p. 131911, 2006.

[105] S. H. Huang *et al.*, "Epitaxial growth and formation of interfacial misfit array for tensile GaAs on GaSb," *Applied Physics Letters*, vol. 90, no. 16, p. 161902, 2007.

[106] C. J. Reyner *et al.*, "Characterization of GaSb/GaAs interfacial misfit arrays using x-ray diffraction," *Applied Physics Letters*, vol. 99, no. 23, p. 231906, 2011.

[107] Y. Wang, P. Ruterana, S. Kret, S. E. Kazzi, L. Desplanque, and X. Wallart, "The source of the threading dislocation in GaSb/GaAs hetero-structures and their propagation mechanism," *Applied Physics Letters*, vol. 102, no. 5, p. 052102, 2013.

[108] J. M. Kang, S.-K. Min, and A. Rocher, "Asymmetric tilt interface induced by 60° misfit dislocation arrays in GaSb/GaAs(001)," *Applied Physics Letters*, vol. 65, no. 23, pp. 2954–2956, 1994.

[109] S. H. Huang, G. Balakrishnan, A. Khoshakhlagh, L. R. Dawson, and D. L. Huffaker, "Simultaneous interfacial misfit array formation and antiphase domain suppression on miscut silicon substrate," *Applied Physics Letters*, vol. 93, no. 7, p. 071102, 2008.

[110] J. B. Rodriguez, L. Cerutti, P. Grech, and E. Tournié, "Room-temperature operation of a 2.25 μm electrically pumped laser fabricated on a silicon substrate," *Applied Physics Letters*, vol. 94, no. 6, p. 061124, 2009.

[111] B. W. Jia *et al.*, "Integration of an InSb photodetector on Si via heteroepitaxy for the mid-infrared wavelength region," *Optics Express*, vol. 26, no. 6, p. 7227, 2018.

Chapter 3

Experimental Methods

3.1 Material Characterisations

3.1.1 Photoluminescence

Photoluminescence (PL) is a widely adopted characterisation technique to examine the optical and electronic properties of semiconductor materials. It is the process of photon re-emission after absorbing incident photons. Figure 3.1 shows the processes involved in PL in a quantum confined structure. A continuous-wave (c.w.) laser shining on the material excites an electron to the conduction band and leaves a hole in the valence band. The electron and hole tend to relax very rapidly to the lowest possible states in their respective bands by releasing phonons to the material. The electrons and holes then recombine through radiative recombination and emit photons. Under a low excitation power intensity, the emitted photons primarily originate from the ground state emissions, i.e. the electrons at the ground electron states recombine with the holes at the ground hole states. The energy of the emitted photons is equal to the energy difference between the two ground states. At a high excitation power intensity, the ground states are saturated, and some of the electrons and holes are able to recombine at the excited states instead of

relaxing to the ground states. The energy of the excited state transition is higher than the energy of the ground state transition. In the intensity-wavelength (or energy) spectrum, an additional high-energy peak will appear due to the excited state transition [1].

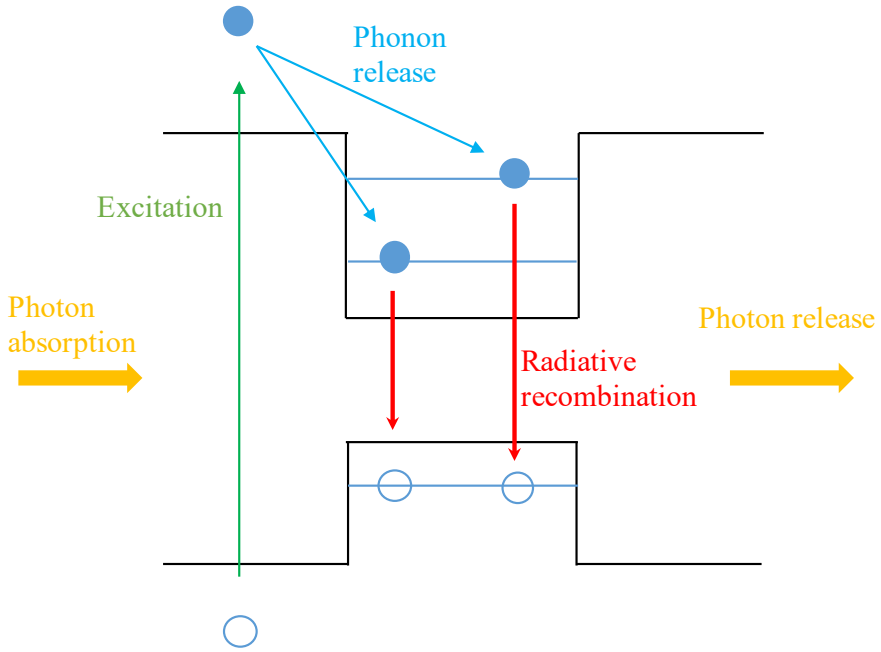

Figure 3.1: Schematics of the radiative emission processes.

Figure 3.2 illustrates a simplified schematic diagram of the PL experimental setup in our laboratory. The sample is typically mounted in a cryo-cooled vacuum chamber (cryostat) for measuring low-temperature PL performance. A c.w. laser source is used to provide continuous optical excitations in the material. The chopper modulates the PL signal producing a periodic (or reference) signal waveform. The monochromator decomposes the PL signal by wavelength, in which only a specific narrow spectrum is allowed to pass through at once. The modulated signal goes through the monochromator and is recorded by the detector. The lock-in amplifier is able to reduce the noise bandwidth and amplify the modulated PL signal from the noisy background to produce a better signal-to-noise ratio.

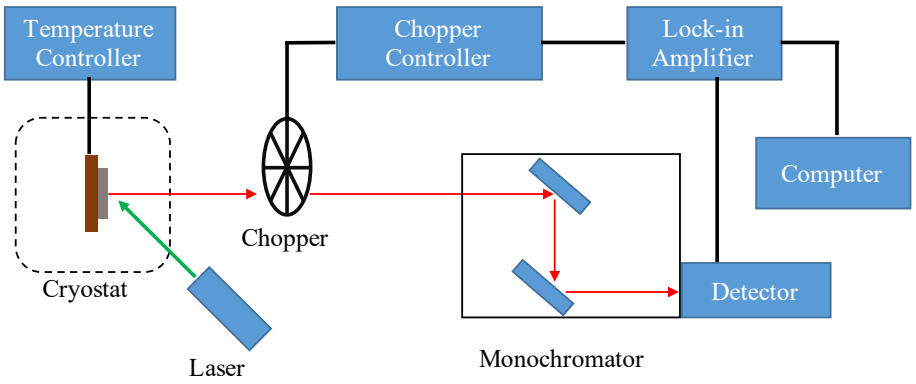

Figure 3.2: Illustration of PL experimental setup.

Apart from the conventional PL measurement, time-resolved PL is often used to characterise the decay lifetime of the PL. In the time-resolved PL measurement, a mode-locked laser is used to produce a very short laser beam pulse and a high-speed streak detector is used to measure the variation of the PL intensity as a function of time. By fitting the intensity-time spectrum, the carrier lifetime can be obtained. In QDs, the PL decay lifetime is typically longer than in bulk materials due to the phonon bottleneck effect [2].

3.1.2 X-ray Diffraction

X-ray diffraction (XRD) is a technique that can be used to identify and characterise the crystal quality of a material. It is based on the interaction of incident X-rays with a crystalline material to produce constructive interference, Figure 3.3 (a). The condition of constructive interference is given by Bragg's law [3],

$$2\mathrm{d}_{hkl}\sin\theta = \mathrm{n}\lambda \tag{3.1}$$

where d_{hkl} is the interplanar spacing, h,k and l are the Miller indices of the reflection planes, θ is the angle of incidence, λ is the wavelength of the incident X-ray and n is an

integer. Figure 3.3 (b) illustrates the configuration of a simplified X-ray diffractometer. X-rays are generated by bombarding a metal target with a beam of electrons. The X-rays are then conditioned by a filter and a monochromator to produce a monochromatic beam for material characterisation. The wavelength of the X-ray is determined by the choice of target material and filter material. Considering the $K\alpha$ peak, the x-ray wavelengths are 1.54 Å for Cu target and Ni filter and 0.71 Å for the Mo target and Co filter [4]. The detector is used to measure the intensity of the X-ray signal. In a typical "$\omega - 2\theta$" scan, the X-ray source and monochromator remain stationary. The sample holder and the detector are arranged to rotate, with the angular speed of the detector twice that of the angular speed of the sample holder. In an "ω" scan, the detectors is set to the Bragg's angle and stays constant, while the sample rotates. The XRD spectra contain a great deal of useful information, such as SL thickness, dislocation density, the crystalline quality, etc. In the following chapters, we will use these XRD measurements to examine the quality of the III-V buffer on Si.

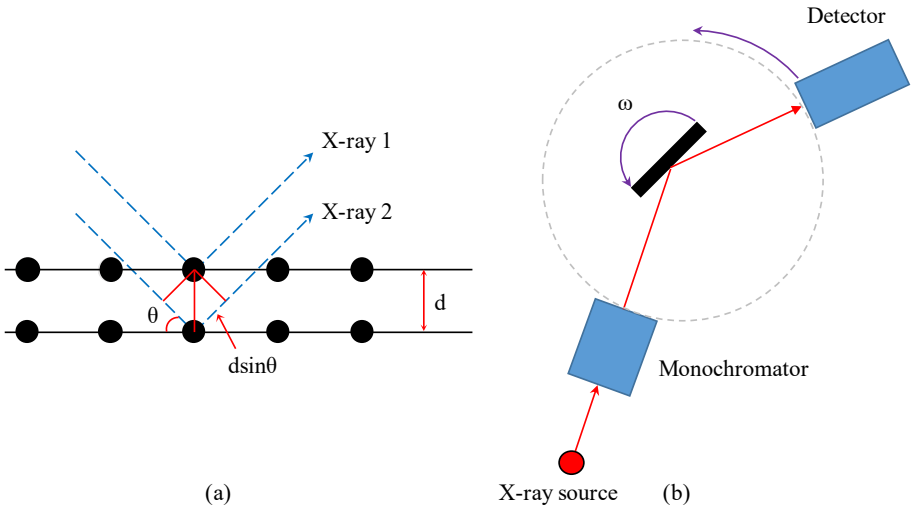

Figure 3.3: Illustrations of (a) Bragg's law and (b) the basic components of an X-ray diffractometer configuration. ω is the angle between the incident beam and sample surface.

3.1.3 Transmission Electron Microscope

The transmission electron microscope (TEM) is another useful tool to characterise the quality of a semiconductor material. In a TEM, the electron beam is accelerated to a relatively high energy (typically 80 keV to 400 keV) in an electric field, thereby providing unprecedented nanoscale resolving power. When capturing a nanoscale image, high resolution and sufficient contrast are the essential requirements. TEM contrast principles depend on the deflected electron beams from the transmitted electron beams [5]. There are three contrast modes: mass-density contrast, diffraction contrast and phase contrast [6]. The mass-density contrast is a straightforward contrast mode where the electrons scattered by the nucleus will be blocked by the aperture, reducing the intensity of transmitted beam. The diffraction contrast works in a similar way to the mass-density contrast. However, rather than blocking the electrons scattered by the large mass nucleus, the diffraction contrast blocks the electrons which satisfy the Bragg's law condition (bright field) or blocks the transmitted electrons (dark field), resulting in reduced intensity of detected electrons. The phase contrast mechanism is often referred to the high-resolution TEM and it must involve at least a transmitted beam and a diffraction beam. The total phase difference ($\Delta = -\pi$) is generated by the diffraction of periodic crystalline material and the objective lens generating interference patterns (amplitude change) with the transmitted electrons.

Scanning TEM (STEM) uses a fine beam of electrons to scan the material surface in a raster pattern. STEM images can be used to estimate the density of TDs. The density of TDs can be estimated by using grids and the equation [6],

$$\rho_{TD} = \frac{2n}{Lt} \tag{3.2}$$

where ρ_{TD} is the density of TDs, n is number of dislocations crossing a set of referencing grid lines, L is the length of grid lines and t is the specimen thickness.

3.2 Device Fabrication

3.2.1 Overall Fabrication Flow

The fabrication flow follows the standard operating procedures developed by members of UCL MBE group at London Centre for Nanotechnology. Figure 3.4 shows the steps for fabricating a single-pixel infrared detector. Steps (1) and (2) are the photolithography procedures. Step (3) is etching or mesa isolation. Steps (4) and (5) are the procedures for surface passivation. Steps (6)–(9) are the procedures for metallisation and lift-off. A detailed description of each procedure is in the following subsections.

3.2.2 Cleaning

Device fabrication processes need to be carried out in a cleanroom as even a small dust particle may influence the device performance significantly. Once the sample was grown, the sample was cleaved into the desired size. The cleaning process was carried out by immersing the sample in acetone and 2-propanol solvents to remove the surface contamination. Since Si substrates have relatively good mechanical properties [7], an ultrasonic bath may be used in order to remove the surface contamination more effectively.

3.2.3 Photolithography

Photolithography is the process of transferring a pattern from the photomask to the photoresist which is pre-coated on the sample surface. The photomask is made of silica and patterned with a thin layer of chromium. A spin coater was used to coat a thin layer of photoresist uniformly on the sample surface. The thickness of the photoresist varies with the viscosity of the photoresist, spin speed and spin time. In our case, the photoresist used was a positive photoresist S1818 [8], which had a thickness of around 2 μm after spin coating at a speed of 4000 revolutions per minute for 30 seconds. After the spin coat-

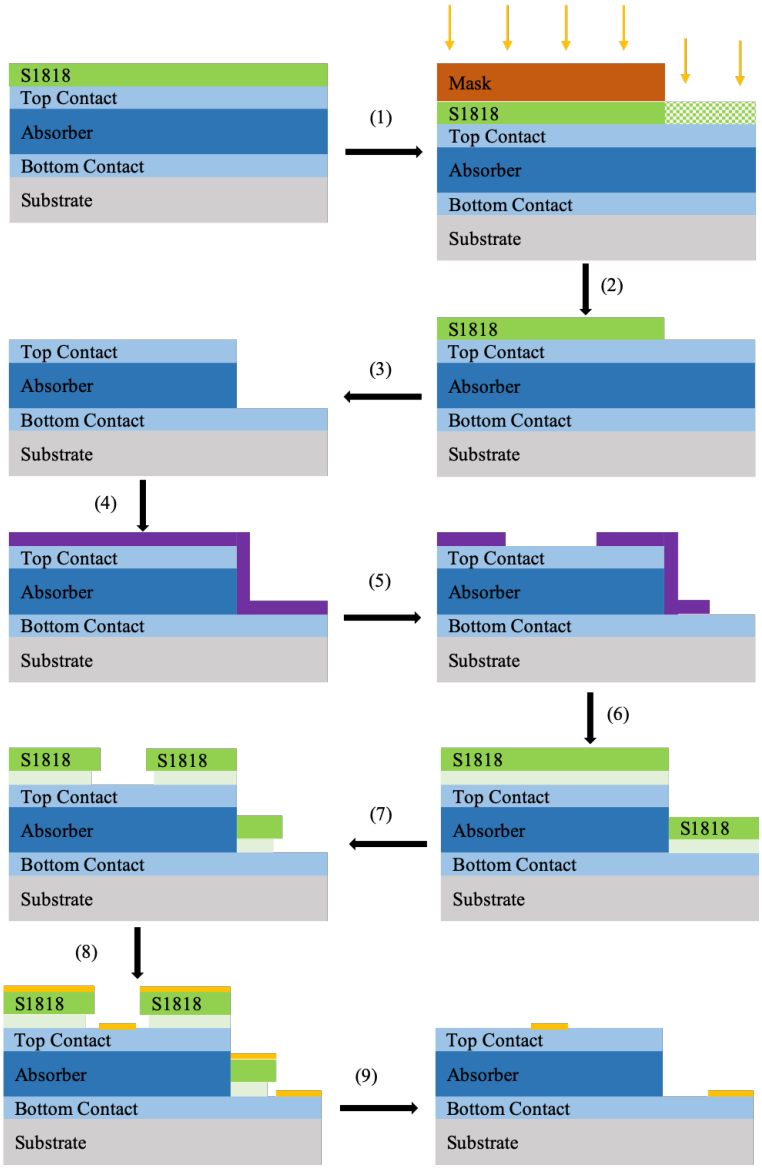

Figure 3.4: The processes for fabricating a single-pixel infrared detector. (1) Exposure, (2) developing, (3) etching, (4) surface passivation (optional), (5) exposure and developing (optional), (6) bi-layer photoresist coating, (7) exposure and developing, (8) metal deposition and (9) lift-off. In this thesis, steps (4) and (5) are not applied to the GaAs based detector, since the surface current is negligible in comparison with the bulk current. In (6)–(9) we assume that the top and bottom contact metals are the same.

ing, a soft bake is required to improve the photoresist adhesion and stiffness. Although the photoresist is generally uniform in thickness over the sample surface after spin coat-

ing, some photoresist may accumulate at the edge of the sample and form so-called edge beads [9]. For direct contact exposure, the edge beads can cause uneven contact between the sample surface and the photomask, hence reducing the pattern quality. The edge beads can be removed by selectively exposing the area with edge beads and stripping with the developer.

For the exposure step, a mask aligner (Karl Suss MJB3, $\lambda_{\mathrm{UV}} = 365$ nm) was used to align the mask pattern accurately with the sample. The exposure time is related to the photoresist selection, the photoresist film thickness and the UV lamp power. Overexposure and underexposure may reduce the quality of the pattern. In my experiments, 2 seconds of exposure yielded the best pattern transfer quality. The UV spectrum selection is another factor that influences the pattern transfer quality. Generally, high-frequency UV light provides high resolution but limits the thickness of the photoresist due to the low penetration depth.

After exposure of a positive photoresist, the area that is exposed to the UV light will become soluble to the developer, leaving the chromium shielded area on the sample surface. In contrast, a negative photoresist will become insoluble to the developer after exposure to the UV light. The selection of positive or negative photoresist mainly depends on the pattern that is being transferred. The final step of photolithography is to develop the pattern with the developer.

3.2.4 Wet Etching

After the pattern is successfully written on the sample surface, the geometry profile (mesa) of the detector can be obtained by etching. There are two general classes of etching techniques: wet etching and dry etching. In this thesis, a wet etching technique was used, owing to its relatively simple steps and ease of use. For etching the GaAs-based device, the etchant used was a mixture of $\mathrm{H_2SO_4}$:$\mathrm{H_2O_2}$:$\mathrm{H_2O}$ = 1:10:80. For etching the InAs/GaSb T2SLs, the etchant used was a mixture of citric acid:$\mathrm{H_3PO_4}$:$\mathrm{H_2O_2}$:$\mathrm{H_2O}$

with the volume ratio 1:1:4:16. Based on our observations, these etching solutions will cause undercut to the detector sidewall. The undercut can reduce the strength of the mesa and cause damage to the detector, especially when fabricating narrow trench and small pixel III-V detector arrays. Dry etching can be used if the undercut issue persists with optimised wet etching recipes and cannot be tolerated [10–12]. Considering that the size of our detectors falls within the range from few hundreds of micrometres to one millimetre, the undercut is acceptable. Furthermore, wet etching steps are simple and do not require a complex and expensive etching system, e.g. the ICP plasma etching system for dry etching. Therefore, we use wet etching method to fabricate our detectors.

3.2.5 Surface Passivation

The interruption of the lattice periodicity at the surface of the semiconductor results in surface dangling bonds. Once the material is exposed to ambient atmosphere, the unsatisfied bonds react with oxygen forming native oxides very rapidly. These native oxides introduce surface trap states within the forbidden band, leading to surface leakage current. As the detector size shrinks, the surface-to-volume ratio increases, and the surface leakage current becomes more and more pronounced. Moreover, the native oxide of indium further increases the surface leakage due to its good electrical conductivity [13]. Surface passivation can protect the surface from erosion by the ambient atmosphere. There is a wide selection of passivation materials, such as SiO_2, SiN_x, SU-8, etc [14]. Since SU-8, a polymer material, has standardised instructions and is easy to apply, this thesis uses SU-8 to passivate the T2SL detectors. It is worth to noting that before applying the passivation layer, surface damage, native oxides and etching by-products should be removed, and the time interval between surface treatment and surface passivation should be kept as short as possible. Surface treatment can be done by immersing the detector into ammonium polysulphide, citric acid-based or hydrochloric acid-based solutions [15, 16]. This thesis uses citric acid-based solution for surface for surface treatment.

3.2.6 Metallisation and Lift-off

Metallisation involves depositing contact metal/alloy on the heavily doped contact layers to form low resistance ohmic contacts. Before depositing the contact metals, the sample has to be patterned with photoresist to avoid coating of the mesa sidewall and the absorbing area. In this step, LOR 10B resist was used as an intermediate between the photoresist (S1818) and the sample. The LOR 10B resist is not a photosensitive resist and it can dissolve in standard developers. As the S1818 pattern develops, the LOR 10B underlayer creates an undercut below the S1818 After metal deposition, the unwanted metals and resists can be removed by lift-off.

The material selection for metallisation depends on the III-V contact layers. For the n-doped GaAs contact layer, 10 nm Ni, 100 nm GeAu (12% Au) alloy, 30 nm Ni and 300 nm Au were used. The metals and alloy then require thermal annealing at 380 $^{\circ}\mathrm{C}$ for 60 s, which allows the Ge element diffuse into the n-doped GaAs layer to form an ohmic contact. In terms of the InAs/GaAs T2SLs photodiodes and nBp barrier detectors, Ti/Pt/Au (50 nm/50 nm/300 nm) are deposited on both top and bottom contacts for metallisation.

3.3 Device Characterisations

3.3.1 Dark Current

Dark current is the device current measured in the absence of light. Figure 3.5 shows a schematic diagram of the dark current measurement setup. A cryogenic probe station with a radiation shield chamber is used to isolate the detector from the ambient environment and radiation. A refrigeration system using either liquid nitrogen or liquid helium and a temperature-controlling system are used to provide different operating temperatures. Once the desired temperature has been reached, the dark current-voltage curve can be measured with the semiconductor device analyser.

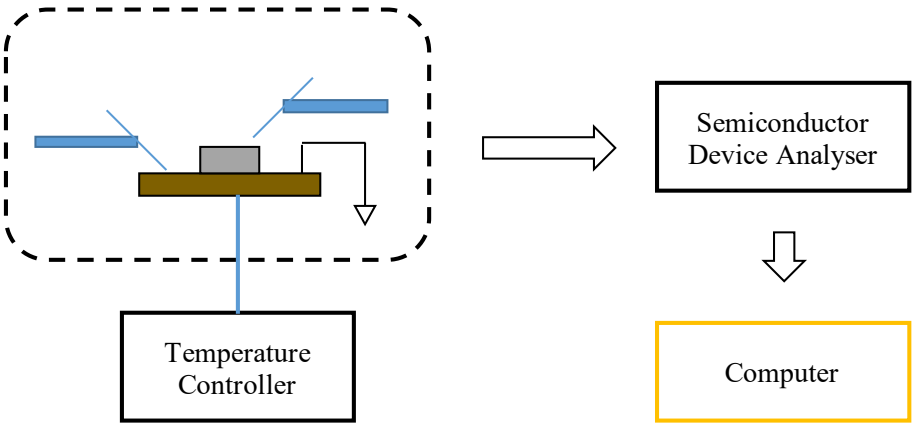

Figure 3.5: Schematic diagram of dark current measurement setup.

3.3.2 Relative Response

The spectral response of an infrared photodetector can be measured by using a Fourier transform infrared (FTIR) spectrometer [17]. The core component of the FTIR spectrometer is the Michelson interferometer, which consists of a moving mirror, a fixed (stationary) mirror and a beamsplitter, Figure 3.6. The beamsplitter splits the infrared radiation into two directions: one beam goes to the fixed mirror and the other beam goes to the moving mirror. Constructive interference occurs during the displacement of the moving mirror. The constructive interference of a specific wavelength of the infrared source corresponds to a specific position of the moving mirror. The two beams that are reflected by the mirrors recombine at the beamsplitter and strike the detector surface. The system creates an interferogram by recording the detector output intensity and time and the Fourier transform of the interferogram produces the response spectrum. To eliminate the influence of the background, for example, infrared attenuation in the atmosphere, the measured detector response spectrum requires normalising to the background spectrum. The background spectrum can be obtained by measuring the spectral response of the FTIR built-in detector, for example, a DTGS detector. The DTGS detector is a thermal detector, which has a nearly constant spectral response over a wide range of the infrared spectrum.

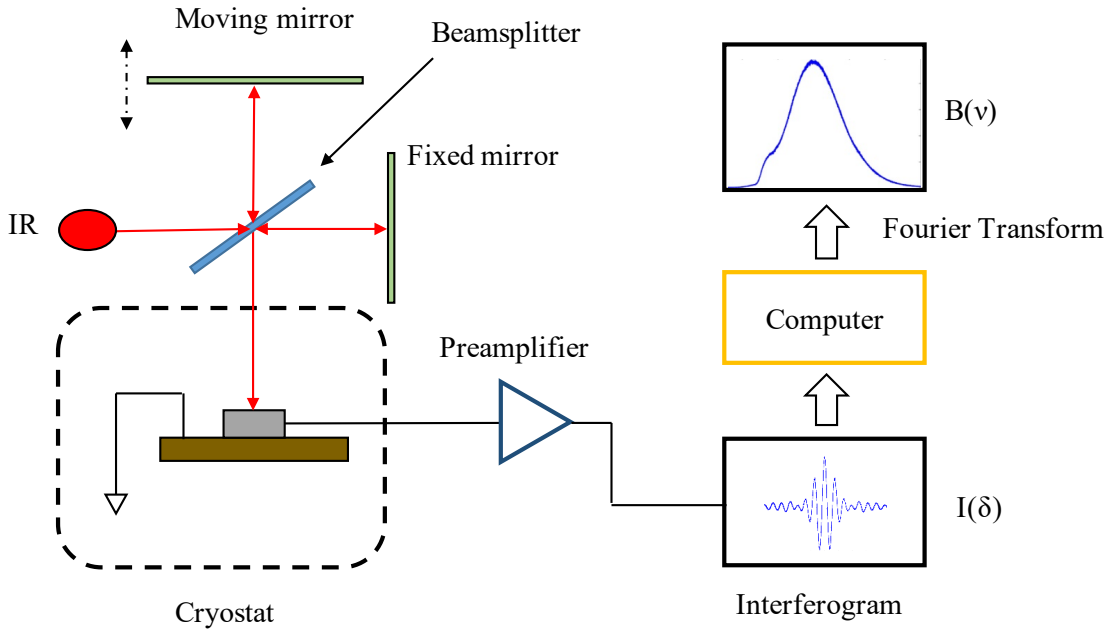

Figure 3.6: Schematic diagram of measuring the photoresponse using an FTIR spectrometer [18].

Therefore, the response spectrum of the DTGS can reflect the fluctuation of the infrared source. Once the background spectrum and detector response spectrum are obtained, the relative response spectrum can be calculated by [18],

$$R_{rel}(\lambda) = \frac{R_{external}(\lambda)}{R_{DTGS}(\lambda)} \tag{3.3}$$

where $R_{rel}(\lambda)$ is the relative response spectrum, $R_{external}(\lambda)$ is the response spectrum of the experimental detector and $R_{DTGS}(\lambda)$ is the background spectrum measured by the built-in detector.

3.3.3 Responsivity

Once the relative response is obtained, the absolute responsivity can be calibrated by using a blackbody radiator. Figure 3.7 illustrates the experimental setup of the blackbody calibration. A CI Systems SR-200N cavity blackbody [19] at 700 °C is used to generate a

standard radiation source as the detector input incident power. A chopper is set to 170 Hz to modulate the incidence into a reference frequency. A low-noise current preamplifier is used to amplify the detector output signal current. The fast Fourier transform (FFT) network analyser converts the input electrical signal from the time domain into the frequency domain. The detector output signal current can be extracted from the frequency domain. With the detector output current, the spectral responsivity can be calculated by using the

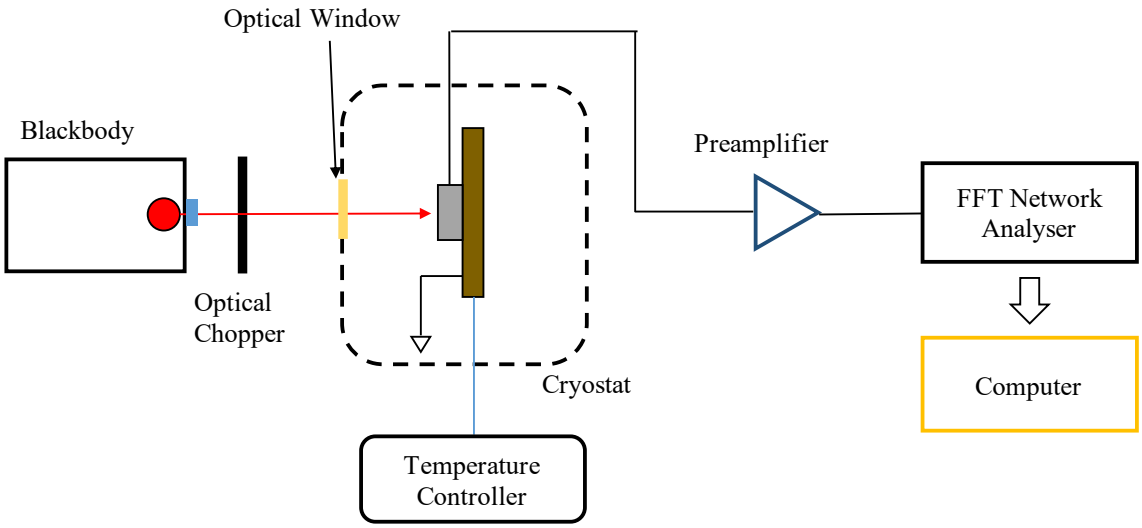

Figure 3.7: Illustration of the experimental setup for calibrating detector responsivity using a blackbody radiator [18].

following equation [20],

$$R_\lambda = \frac{I_{total}}{\int M_{e,\lambda} \times \frac{A_{ap}}{r^2} \times A_d \times T \times MF \times R_{rel}(\lambda) d\lambda} \tag{3.4}$$

where I_{total} is the current output from the detector, $M_{e,\lambda}$ is the spectral radiant exitance of the blackbody, A_{ap} is the area of the blackbody aperture, r is the distance between the detector and the centre of the blackbody, A_d is the sensitive area of the experimental detector, T is the transmissivity of the ZnSe optical window, MF is the modulation factor of the optical chopper, which is 0.45, and $R_{rel}(\lambda)$ is the relative response spectrum.

References

[1] J. Wu *et al.*, "Monolithically Integrated InAs/GaAs Quantum Dot Mid-Infrared Photodetectors on Silicon Substrates," *ACS Photonics*, vol. 3, no. 5, pp. 749–753, 2016.

[2] J. Urayama, T. B. Norris, J. Singh, and P. Bhattacharya, "Observation of phonon bottleneck in quantum dot electronic relaxation," *Physical Review Letters*, vol. 86, no. 21, pp. 4930–4933, 2001.

[3] T. Kanai, S. Nakashima, and T. Oki, "Protection against a wide UV wavelength range by Bragg reflection from polycrystalline colloidal photonic crystals," *Journal of Materials Chemistry C*, vol. 7, no. 25, pp. 7512–7515, 2019.

[4] R. Guinebretière, *X-ray Diffraction by Polycrystalline Materials*. ISTE, 2007.

[5] "Transmission electron microscopy," in *Materials Characterization*, pp. 83–126, Wiley-VCH Verlag GmbH & Co. KGaA, 2013.

[6] W. Li, *Characterization of InGaAs QDs grown on GaAs and Si substrate*. PhD thesis, University of Sheffield, 2017.

[7] A. Rogalski, "Recent progress in infrared detector technologies," *Infrared Physics & Technology*, vol. 54, no. 3, pp. 136–154, 2011.

[8] $\mathrm{Microposit}^{\mathrm{TM}}\ \mathrm{S1800}^{\mathrm{TM}}$ *G2 Series photoresists*.

[9] I. Jekauc, M. Watt, T. Hornsmith, and J. Tiffany, "Necessity of chemical edge bead removal in modern-day lithographic processing," in *Advances in Resist Technology and Processing XXI* (J. L. Sturtevant, ed.), SPIE, 2004.

[10] M. Huang *et al.*, "ICP etching for InAs-based InAs/GaAsSb superlattice long wavelength infrared detectors," *Infrared Physics & Technology*, vol. 90, pp. 110–114, 2018.

[11] K. Miura *et al.*, "High performance type II superlattice focal plane array with 6 μm cutoff wavelength," in *Infrared Technology and Applications XLII* (B. F. Andresen, G. F. Fulop, C. M. Hanson, J. L. Miller, and P. R. Norton, eds.), SPIE, 2016.

[12] A. Dehzangi *et al.*, "nBn extended short-wavelength infrared focal plane array," *Optics Letters*, vol. 43, no. 3, p. 591, 2018.

[13] A. Gin *et al.*, "Passivation of type- II InAs/GaSb superlattice photodiodes," *Thin Solid Films*, vol. 447-448, pp. 489–492, 2004.

[14] O. Salihoglu, A. Muti, and A. Aydinli, "A comparative passivation study for InAs/GaSb pin superlattice photodetectors," *IEEE Journal of Quantum Electronics*, vol. 49, no. 8, pp. 661–666, 2013.

[15] K. Banerjee, S. Ghosh, E. Plis, and S. Krishna, "Study of short- and long-term effectiveness of ammonium sulfide as surface passivation for InAs/GaSb superlattices using x-ray photoelectron spectroscopy," *Journal of Electronic Materials*, vol. 39, no. 10, pp. 2210–2214, 2010.

[16] E. Plis, M. Kutty, S. Myers, H. Kim, N. Gautam, L. Dawson, and S. Krishna, "Passivation of long-wave infrared InAs/GaSb strained layer superlattice detectors," *Infrared Physics & Technology*, vol. 54, pp. 252–257, may 2011.

[17] A. P. Thorne, *Spectrophysics*. Springer Netherlands, 1988.

[18] Z. Ye, *Design, fabrication and characterization of quantum dot infrared photodetectors*. PhD thesis, The University of Texas at Austin, 2003.

[19] *SR-200N High Emissivity Blackbody, CI Systems*.

[20] H. Mohseni *et al.*, "Growth and characterization of InAs/GaSb photoconductors for long wavelength infrared range," *Applied Physics Letters*, vol. 71, no. 10, pp. 1403–1405, 1997.

Chapter 4

Direct Growth of $In_{0.5}Ga_{0.5}As$/GaAs Quantum Dot Infrared Photodetectors on Si Substrates

4.1 Introduction

The advantages of 3D confinement have been introduced in the first two chapters. The localisation of electrons in QDs can lead to good defect tolerance. Wu and co-workers demonstrated the first direct growth InAs/GaAs QDIPs on Si substrates, operating in the mid-infrared spectral range 5-8 μm [1]. Chen et al. demonstrated InAs/InGaAs/GaAs DWELL QDIPs on Si with a peak response wavelength at 6.4 μm [2]. This chapter will introduce work following on from Wu and co-workers' InAs QDIPs on Si to study the behaviour and performance of $In_{0.5}Ga_{0.5}As$ /GaAs QDIPs on Si. To some extent, InGaAs QDIPs can be tailored into longer wavelength response than InAs QDIPs due to the relatively small conduction band offset in InGaAs QDs. However, growth parameters, e.g. growth temperature, amount of deposition, etc., can play a significant role in determining the actual response wavelength [3]. By analysing the dark current results, we have found

that the dark current is dominated by phonon-assisted tunnelling current at low temperatures with a bias voltage -0.1 V. Phonon-assisted tunnelling is a phonon-mediated dark current generation mechanism from the upper states [4]. At high temperatures, thermionic current becomes the main source of dark current.

In terms of photoresponse, our InGaAs QDIPs show two photoresponse peaks at 77 K in the MWIR and LWIR bands as the result of band-to-continuum and band-to-band transitions, respectively, which indicates the QDIPs have the potential to operate in two-colour mode. Two-colour infrared imagers can offer enhanced sensing functionalities compared with single colour imagers, e.g. measuring the absolute temperature of a greybody target with unknown emissivity, sensing the unique infrared signatures in different spectral bands, and a better distinction between the target and the background [5, 6]. QD-based two-colour photodetectors have been reported previously. Chapter 2 has mentioned the work done by Krishna et al., as they used the InAs/InGaAs DWELL structure to achieve three-colour photoresponse [7]. Lin et al. reported two-colour QDIPs by stacking of five periods of InAs QDs with five periods of InGaAs QDs [8]. Researchers from University of Southern California reported voltage-tunable two-colour QDIPs employing intersubband transitions in small and large QDs [9, 10].

In terms of material characterisations, low temperature PL studies reveal that the size distribution of the dot falls is non-unimodal. Good quality of QDIPs on Si has been confirmed, with low TD density ($\sim 10^6$ cm^{-2}) measured by cross-sectional TEM and long PL decay lifetime ($>$ 1 ns).

4.2 Material Growth and Device Fabrication

The $\mathrm{In_{0.5}Ga_{0.5}As}$/GaAs n-i-n QDIPs were grown on a Si (001) substrate with 4° offcut to the [01-1] direction using a solid-source Veeco Gen 930 MBE system. Figure 4.1 illustrates the structure of the InGaAs QDIPs on Si. Before the epitaxy growth, the substrate

was pre-treated for 30 minutes at 900 $^{\circ}\mathrm{C}$. The initiation of growth started with a 5 nm AlAs nucleation layer, which was deposited by migration-enhanced epitaxy at 370 $^{\circ}\mathrm{C}$ with a low growth rate of 0.1 ML/s. Subsequently, a 25 nm GaAs nucleation layer was grown on top of the AlAs nucleation layer with the same conditions. A 970 nm GaAs buffer layer was then deposited at 580 $^{\circ}\mathrm{C}$ with a growth rate of 0.7 ML/s. After the buffer layer, four repeats of five periods of 10 nm $\mathrm{In_{0.15}Ga_{0.85}As}$/10 nm GaAs SLSs were grown as the DFLs to reduce the dislocation density. Each period of SLS was separated by a 350 nm GaAs spacer. The growth of QDIPs was carried out in the following sequence: 500 nm n-GaAs bottom contact with Si doping density of $2 \times 10^{18}\ \mathrm{cm^{-3}}$, an 80 nm undoped GaAs spacer, 20 periods of $\mathrm{In_{0.5}Ga_{0.5}As}$/GaAs QDs separated by 50 nm GaAs spacers in order to maximise the absorption thickness and minimise the strain accumulation, a 30 nm undoped GaAs spacer and 300 nm n-GaAs top contact with Si doping density of $2 \times 10^{18}\ \mathrm{cm^{-3}}$. The nominal thickness of the $\mathrm{In_{0.5}Ga_{0.5}As}$ QDs was 7 MLs, and the QDs were directly doped with Si to about two electrons per dot (2e/dot) for the electrons to populate the ground state.

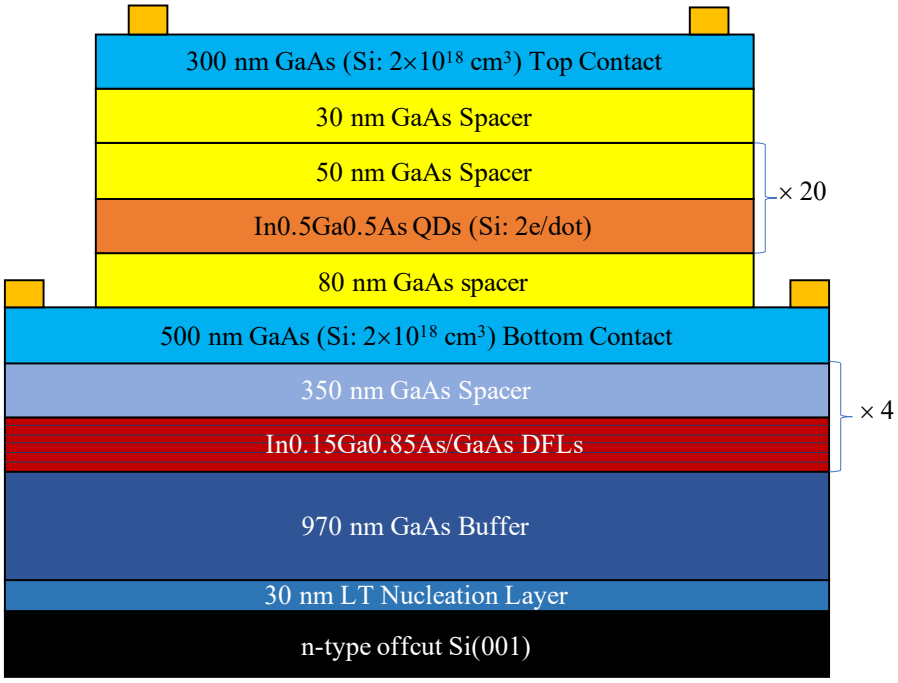

Figure 4.1: Schemtic of the InGaAs QDIP on Si substrate. LT = Low Temperature.

The QDIPs were fabricated in the cleanroom at the London Centre for Nanotechnology. Circular detector mesas with a diameter of 1000 μm were defined by standard photolithography and wet chemical etching. The etchant is a mixture of H_2SO_4:H_2O_2:H_2O with the volume ratio of 1:10:80. The top and bottom contacts were processed by thermal evaporation of Ni/GeAu/Ni/Au (10 nm/100 nm/30 nm/300 nm) and lift-off. The Ohmic contacts were formed by thermal annealing at 380 °C for 60 s.

4.3 Material Characterisations

A cross-sectional transmission electron microscope (TEM) image of the GaAs buffer is shown in Figure 4.2 (a). As can be seen, a large number of TDs were generated at the GaAs/Si interface. Although some of TDs were self-annihilated within the initial 1 μm thick buffer, a high density of TDs $\sim 10^9$ cm^{-2} still can be measured before the DFL1 layer shown in Figure 4.2 (a). As the TDs enter the SLS region, the in-plane strain in-

creases the horizontal movement of the TDs, which reduces the number of vertically propagating TDs. Thus, after DFL4, the TD density is reduced by about 3-4 orders of magnitude to the level of $\sim 10^6$ cm^{-2}, indicating an effective TD reduction with SLS DFLs. Comparing with previous work [1] and [2], the TEM estimated TD density is at the same level.

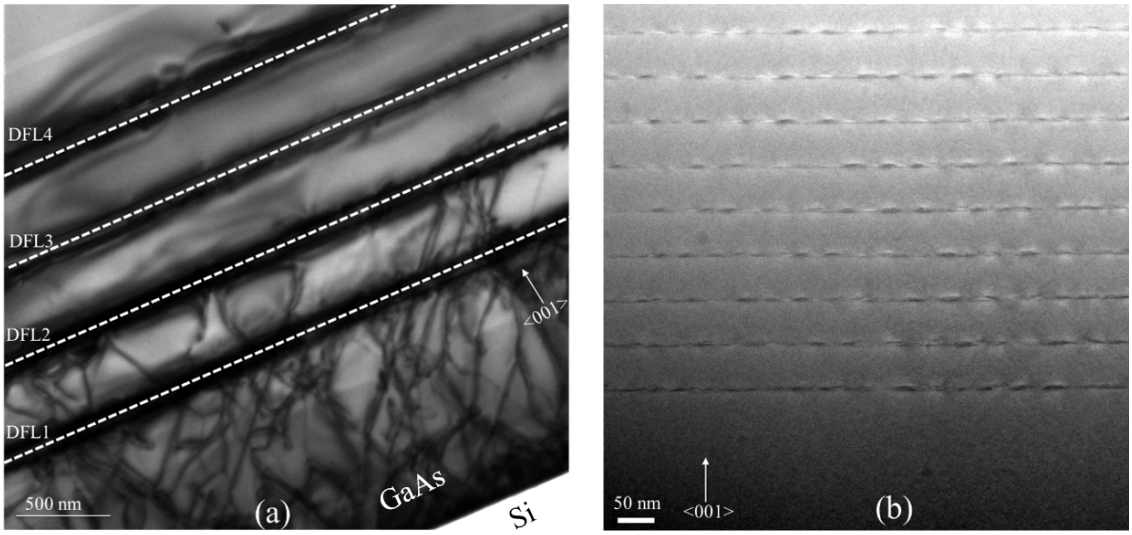

Figure 4.2: Cross-sectional TEM images of (a) the III-V buffer region and (b) the QD region.

Figure 4.2 (b) shows the cross-sectional TEM image of the InGaAs QD region. The formation of QDs is clearly resolved by the TEM and no observable TDs can be found in the image. In order to examine the QD lateral width distribution, the base widths of 84 InGaAs QDs were measured, see Figure 4.3. The dot lateral dimension is widely distributed on the x-axis and does not exhibit a typical Gaussian distribution. The variation indicates a large inhomogeneity in the lateral dimension of the $\mathrm{In_{0.5}Ga_{0.5}As}$ QDs.

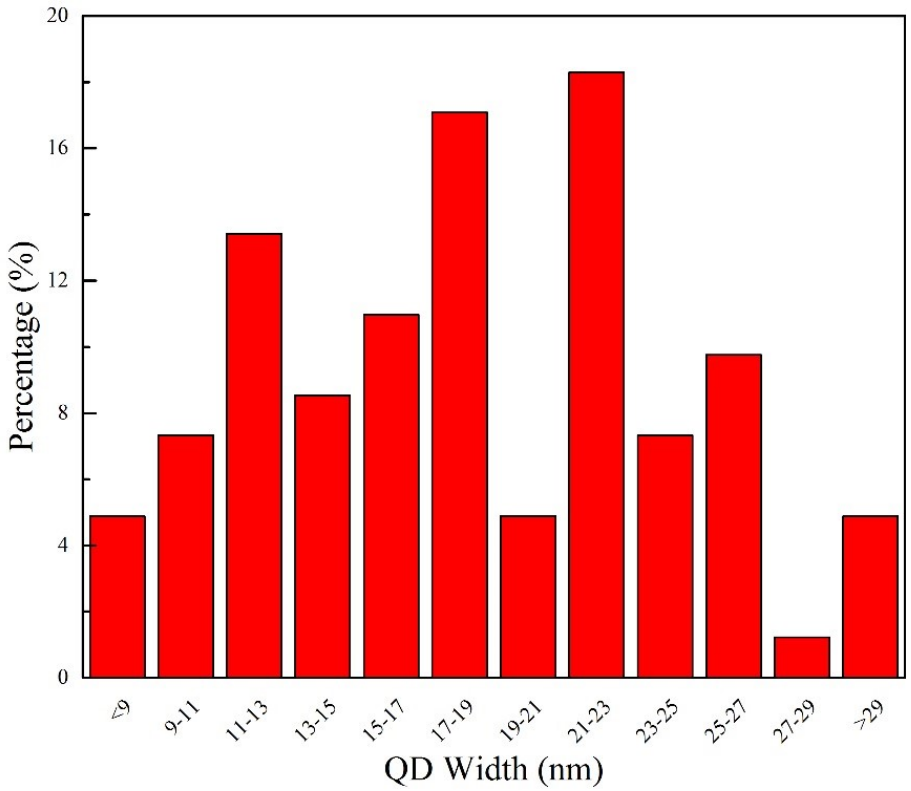

Figure 4.3: Statistics of the base width of the InGaAs QDs measured from the cross-sectional TEM image, Figure 4.2 (b). A total number of 84 QDs were counted.

Power-dependent photoluminescence measurements were performed at 10 K using a frequency-doubled Nd:YAG laser (λ = 532 nm). The results are presented in Figure 4.4. In Figure 4.4 (a), the low excitation power density (3.7×10^{-4} $\mathrm{W/cm^2}$) PL spectrum has been decomposed with three Gaussian functions, labelled group 1, 2, and 3 in the figure. The peak positions for groups 1, 2 and 3 are $\sim$ 1.22 eV, 1.25 eV and 1.27 eV, respectively, and the full width at half maximum (FWHM) values are $\sim$33 meV, 19 meV and 41 meV, respectively. The number of Gaussian functions for fitting the PL spectrum still holds even when the laser power density reaches 29 $\mathrm{W/cm^2}$, Figure 4.4 (b), meaning that all three groups are ground state emissions and none are excited state emission [1]. The origin of each emission peak is not understood at this stage, but it seems clear the QD size distribution is not unimodal. Many papers have reported on bimodal size distribution

QDs [1, 2, 11, 12], which exhibited a double ground state emission peak feature in the PL spectra. The formation of the second size distribution is affected by the indium desorption associated with high growth temperature, the amount of dot material coverage and step edges on the epitaxy surface [13, 14]. However, tri-modal distributed QDs have also been reported [15, 16]. Considering the PL results in this work, the low temperature PL results may suggest the presence of three different size groups of QDs, i.e. large size (group 1), medium size (group 2) and small size (group 3). Under an excitation power density of 5000 $\mathrm{W/cm^2}$, an additional peak at $\sim$ 1.31 eV can be observed, corresponding to the excited state emission, 4.4 (c).

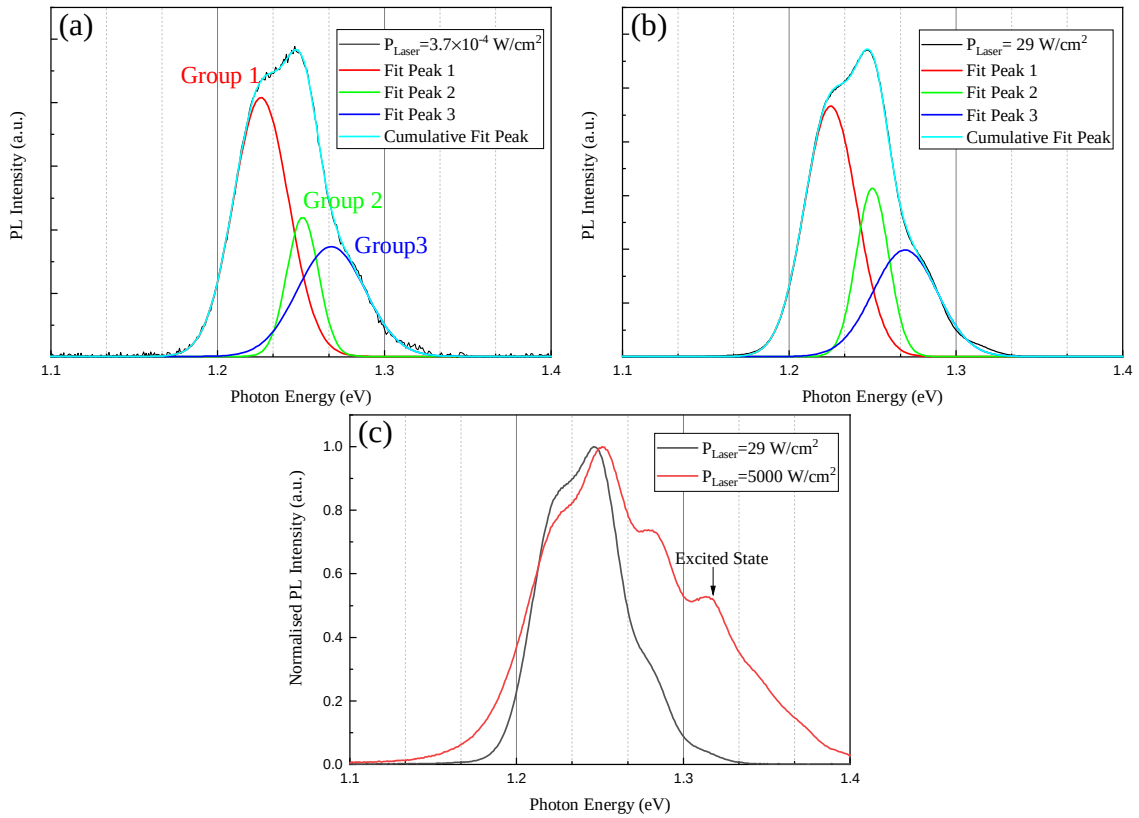

Figure 4.4: Gaussian fittings of the InGaAs QDIP PL spectra with laser power density (a) (3.7 $\times$ 10$-$4 $\mathrm{W/cm^2}$ (b) 29 $\mathrm{W/cm^2}$ and (c) A comparison of the PL spectra measured with laser power densities 29 $\mathrm{W/cm^2}$ and 5000 $\mathrm{W/cm^2}$.

In order to further probe the material quality of the QDIP on Si, a time-resolved PL

decay measurement was performed at 10 K. A mode-locked Ti:sapphire laser with a 2 picosecond (ps) pulse at 750 nm excitation wavelength was used. The excitation density per pulse was 6×10^{11} photons/cm^2 and the repetition rate was 76 MHz. The PL signal was collected by a Hamamatsu Synchroscan C5680 streak camera with infrared enhanced S1 cathode. Four selected emissions are plotted in Figure 4.5 (a). The emissions at 1.22 eV and 1.28 eV can be attributed to the ground state emissions from group 1 QDs and group 3 QDs, respectively. The PL decay time for the ground state emission of group 1 is 1243 ps, which is comparable to the decay time reported for the similar InGaAs QDs grown on native substrates [17], indicating a good material quality of InGaAs QDs on Si. The PL decay time for the group 3 (small dot size) QDs is shorter than the PL decay time of group 1 (large dot size), which may be due to the carriers transferring from the ground state of small QDs into the lower lying ground state of large QDs, resulting in delayed PL of group 1 [18, 19]. The emission at 1.31 eV with PL decay time 475 ps is the emission energy from the excited state. The PL decays for all emission wavelengths are shown in Figure 4.5 (b) with reference to the normalised continuous wave PL signal measured under the excitation power density of 5000 W/cm^2.

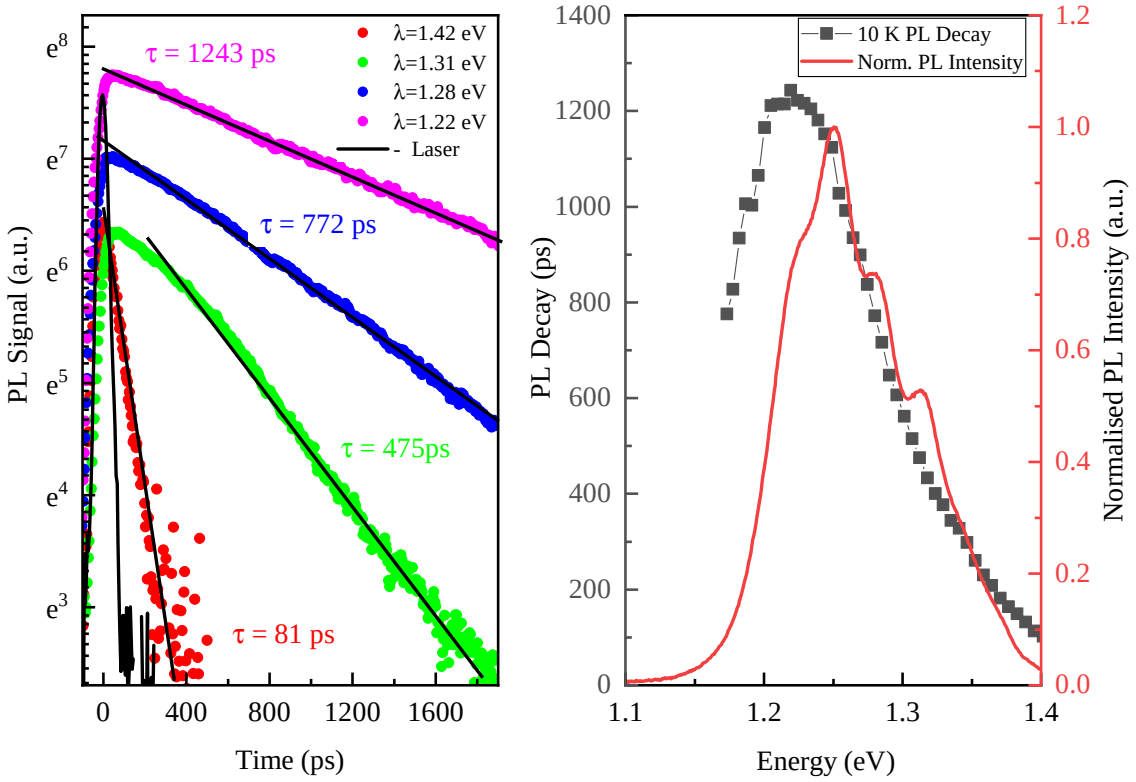

Figure 4.5: (a) Time-resolved PL decay measured at 10 K for the emission wavelengths $\sim$ 1.42 eV, 1.31 eV, 1.28 eV and 1.22 eV corresponding to the wetting layer emission, excited state emission, group 3 ground state emission and group 1 ground state emission, resepectively. (b) PL decay time for all measured emission energies with reference to the continuous wave PL signal measured at 10 K with laser power dneisty 5000 $\mathrm{W/cm^{-2}}$.

4.4 Device Characterisation

4.4.1 Dark Current

The QDIP with diameter of 1000 μm was loaded into a low temperature probe station for dark current measurements. The measurement of positive biased dark current was carried out by connecting the top contact to the positive terminal, and the negative bias were performed by connecting the top contact to the negative terminal. As observed in

Figure 4.6, the dark current increases with bias, as the electric field lowers the height of the barrier and increases the tunnelling current through the barrier [20, 21]. The slight asymmetry of the dark current curves with bias is likely to be due to the asymmetry in potential in the growth direction. It is believed that the lens shaped QDs, wetting layers underneath the QDs, asymmetric heterostructure design and the asymmetric capping, e.g. GaAs (barrier)/InAs (QD)/InGaAs (capping), can be responsible for potential difference along the growth direction [10, 22, 23]. The latter two factors are not applicable in this work, as the design and capping material are identical surrounding the dot layer. Thus, the asymmetry in the dark current profile may possibly be due to the lens shaped QDs as well as the wetting layers underneath the QDs resulting in an asymmetric potential in the growth direction, hence affecting the dark current performance under positive and negative bias conditions [24]. Similar asymmetry profiles for the same magnitude of positive bias and negative bias are also observed in the photoresponse spectra, as will be discussed in the next subsection. The dark current increase with temperature is due to the increased thermionic emission of electrons as well as thermally assisted tunnelling of electrons from the QDs [25].

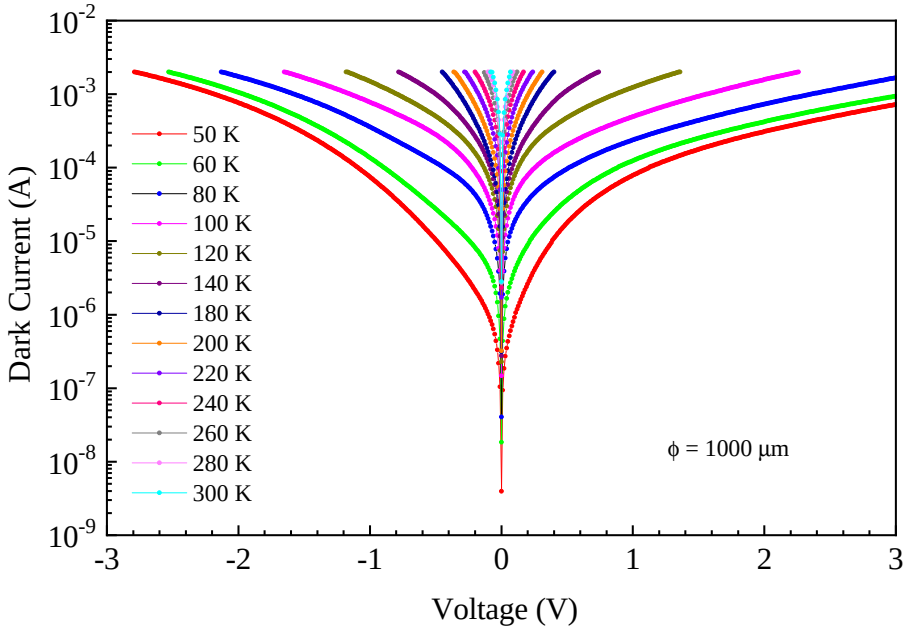

Figure 4.6: Temperature-dependent dark current-voltage measurement for the QDIP with a diameter of 1000 μm.

In order to understand the dark current generation mechanism, the dark current values measured at + 0.1 V were extracted and plotted in Figure 4.7. The y-axis is expressed as the natural logarithm of dark current density and the x-axis takes the form of reciprocal temperature (1/T). The dark current activation energy was obtained by fitting with the Arrhenius equation [26],

$$\ln(J_d) = -\frac{E_a}{k_B}\frac{1}{T} + C \tag{4.1}$$

where J_d is the dark current density, E_a is the dark current activation energy, k_B is the Boltzmann constant and C is a constant. The dark current generation mechanisms in QDIPs include thermal emission of electrons from the bound states and tunnelling currents through the barrier [27], such as field assisted tunnelling, phonon assisted tunnelling, defect assisted tunnelling and sequential assisted tunnelling [10, 28]. At low temperatures, the Arrhenius fitting gives activation energies E_{a1} = 31 meV (red fitting line) for the temperatures from 50-80 K, and E_{a2} = 57 meV (green fitting line) for the temperatures from

80-120 K. These activation energies roughly coincide with the energies of 1LO-phonon and 2LO-phonon, suggesting that the phonon assisted tunnelling current is the dominant source contributing to the dark current [10]. Above 120 K, the dark current activation energy rises to E_{a3}=219 meV (blue fitting line). Since the field assisted tunnelling mechanism expected to have negligible effect on the dark current with a bias voltage as low as 0.1 V, the activation energy is mainly attributable to thermionic emission of electrons from the bound states.

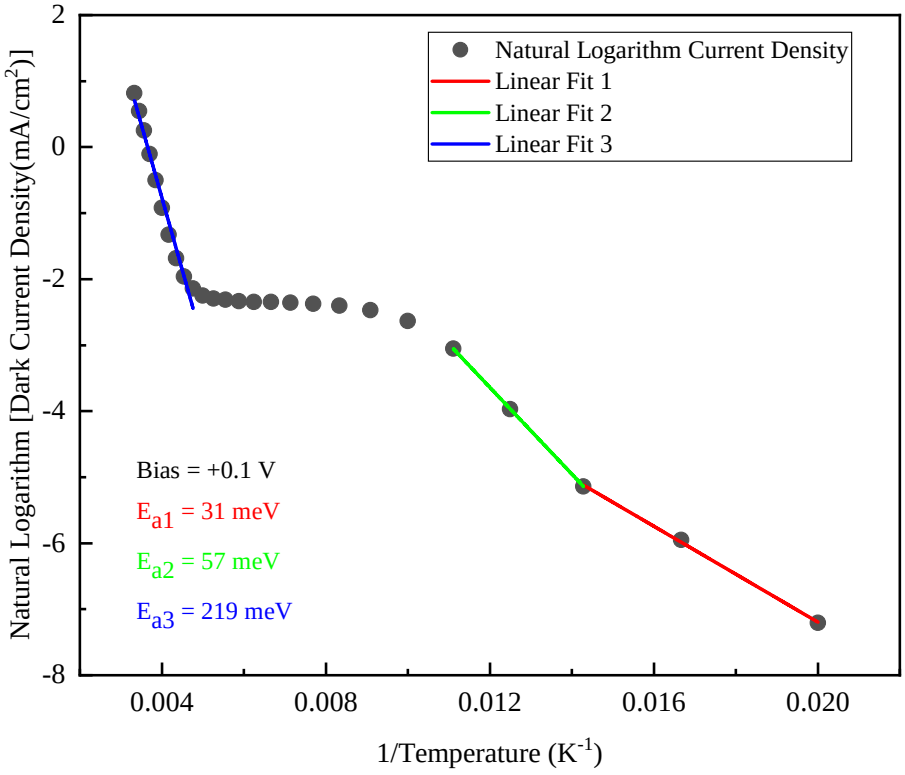

Figure 4.7: Natural logarithm of dark current density measured at +0.1 V as a function of reciprocal temperature (1/T).

4.4.2 Photoresponse

The photoresponse curves were measured by using a Bruker Equinox-55 FTIR spectrometer. The wire-bonded detector was configured 90° to incident infrared beam. The pho-

toresponse curves for bias + 1 V and - 1 V are displayed in Figure 4.8. The slightly lower photoresponse curve under negative bias is due to the asymmetric potential of the QDs, as mentioned previously in the context of dark current characterisation. The high energy peak, centred at 6.1 μm (203 meV), is close to the dark current activation energy fitted in the high temperature region, E_{a3} = 219 meV. Since the QDs are doped with two electrons per dot, with no electron population at the excited states, the transition energy is the energy difference between the QD ground state and the continuum. The broad spectral width ($\Delta\lambda/\lambda_p \sim 40\%$) of the high energy peak suggests a B-C transition corresponding to the energy gap between the QD ground state and the continuum [29]. On the long wavelength side, the photoresponse linewidth is about $\Delta\lambda/\lambda_p \sim$ 10-15%, suggesting the B-B transitions of the InGaAs QDIPs [30].

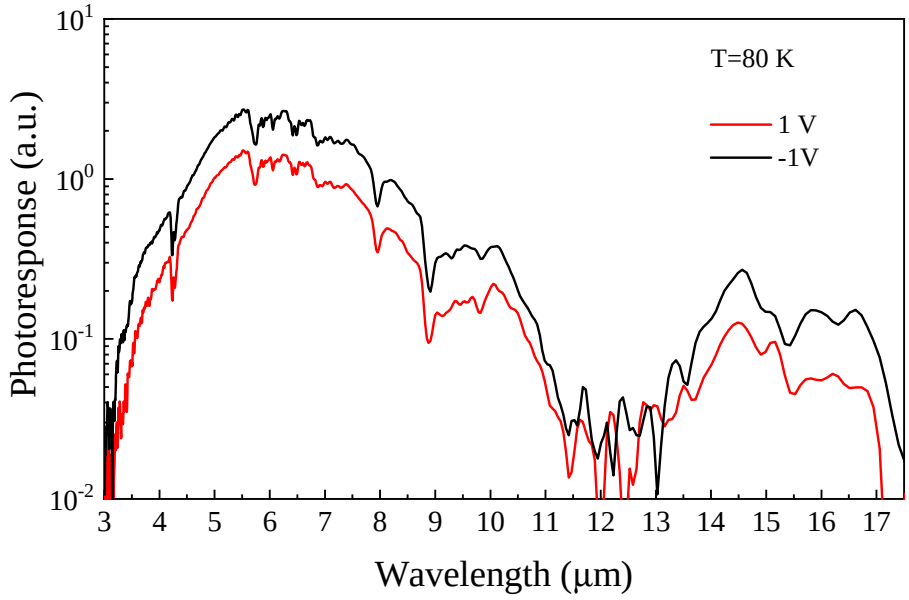

Figure 4.8: Photoresponse spectra measured at 80 K with different bias voltages.

To further investigate the origins of the MWIR and LWIR transitions, voltage-dependent photoresponse measurements were conducted at 80 K, see Figure 4.9. Please note that we have used a slightly extended definition for LWIR in this section (8-18 μm). The intensities of both the MWIR and LWIR transitions rise with the bias voltage, which can be

understood by the capture rate of photoexcited carriers. With increasing electric field, the electron velocity increases and, at the same time, the external field lowers the potential barrier and reduces the capture probability [31]. The photoresponse intensity of the bound-to-continuum transition (MWIR band) is about one order of magnitude higher than the intensity of the bound-to-bound transition (LWIR band). In the bound-to-bound transition, the electrons are excited by photons to a higher bound state inside the QD. To contribute to the photocurrent, these photoexcited electrons must overcome the potential barrier and escape from the QD into the continuum through tunnelling or thermal excitation [32]. Thus, the lower intensity in the LWIR region can be explained by the higher potential barrier and hence the lower rate for the photoexcited electrons to overcome the potential barrier.

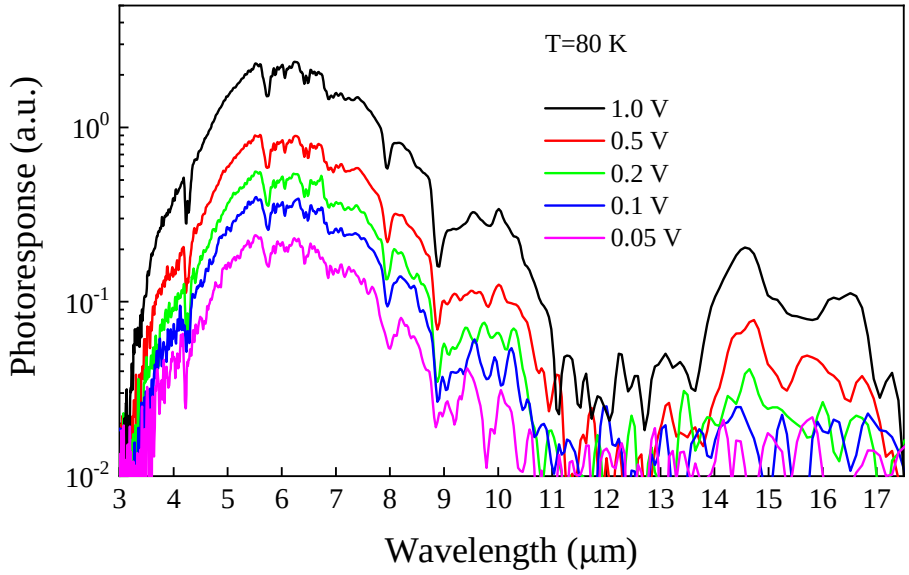

Figure 4.9: Voltage-dependent photoresponse spectra measured at 80 K with different positive bias voltages from 0.05 V to 1 V.[1]

[1]Figure 4.9 provides an overall indication of the response envelope and its variation with bias conditions. The noise level in the measurement, calculated from a measurement at zero bias, where no photoresponse was observed, was 9.3×10^{-3} (RMS) in the same units. This noise level has a significant impact at low bias and long wavelengths, but it is about 0.3% of peak response at MWIR and about 2.5% for the LWIR at 1 V. Some of the rapid variations shown here, e.g. the dip at 4.3 μm, may be due to atmospheric absorption that has not been eliminated completely in the calibration process. The response scale is in arbitrary units and further work will be required to determine the absolute intensities.

Figure 4.10 plots the relation between the integrated photoresponse and the electric field for the MWIR and LWIR bands. The photocurrent density of the QDIP can be determined by the following equation [27],

$$J_p = \frac{\delta q n \rho_{QD} \Phi_S}{p_k} \tag{4.2}$$

where J_p is the photocurrent density, δ is the electron capture cross-section coefficient, q is the electron charge, n is the average number of electrons in QDs, ρ_{QD} is the QD sheet density, Φ_S is the single photon flux and p_k is the capture probability. The relationship between the capture probability and barrier height is [27, 33],

$$p_k \propto \frac{\tau_{trans}}{\tau_{lifetime}} \sim \tau_{trans} \exp\left(-\frac{V_b}{k_B T}\right) \tag{4.3}$$

where τ_{trans} and $\tau_{lifetime}$are the carrier transit time and carrier capture time, V_b is the height of the potential barrier, k_B is the Boltzmann constant and T is the device temperature. The above equations suggest that when the bias voltage is large enough to overcome the potential barrier, the photocurrents of both bands will increase exponentially, which in good agreement with Figure 4.10. In the low electric field region, the photocurrent increase or the collection efficiency increases the electric field, which do not follow the same linear slop as the high electric field region. To increase the LWIR band photoresponse, it is desirable to design the excited states to be as close as the continuum as possible.

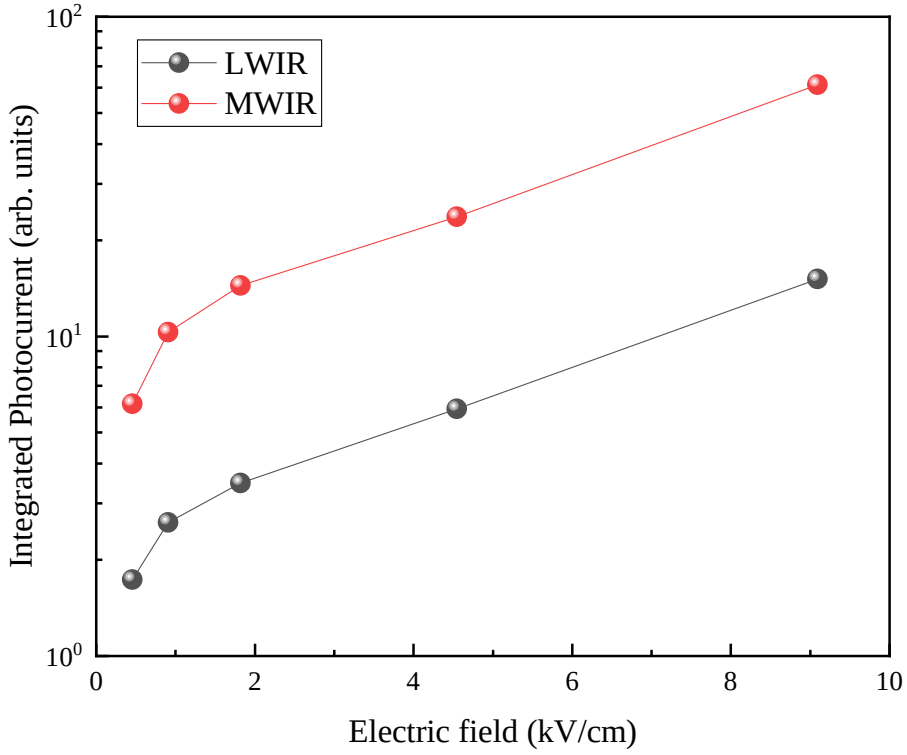

Figure 4.10: Voltage dependent integrated photocurrent for the MWIR (3-8 μm) (red) and the LWIR (8-18 μm) (black).

4.5 Conclusion

Two-band photoresponse InGaAs/GaAs QDIPs have been demonstrated on Si substrates by the direct growth method. TEM imaging on the GaAs buffer has shown that the vertically propagating TDs have been effectively controlled with four sets of DFLs. The low temperature PL results suggest that the QD size is distributed in different size groups. Dark current measurements have shown that the phonon-assisted tunnelling mechanism dominates the generation of dark current for the temperatures below 120 K, while at higher temperatures, the thermionic emission of electrons from the QD becomes the major source of dark current. Intersubband transitions have also been discussed. The MWIR band photoresponse is attributed to the transition between the ground state and the contin-

uum and the LWIR transition corresponds to the transition between the ground state and the excited state inside the QDs. The LWIR band shows a lower photoresponse intensity than the MWIR band, suggesting an optimisation of the QD electronic levels is required in order to increase the LWIR band photoresponse. In addition, future work should focus on improving the QD size homogeneity, as this is related to the absorption efficiency, and optimising the III-V buffer layer to reduce the defect density in the material. Overall, as a proof of concept of buffer technology and device design, this work shows that the InGaAs/GaAs QDIP is capable of operating with the optimised GaAs buffer on Si at 80 K.

4.6 Contribution Statement

The InGaAs/GaAs QDIP on Si was designed and grown by Dr. Jiang Wu, University College London. The TEM images and PL results were provided by Dr. Yuriy I. Mazur, University of Arkansas. The dark current and photoresponse results were provided by Dr. Mykhaylo P. Semtsiv, Humboldt University Berlin.

References

[1] J. Wu *et al.*, "Monolithically integrated InAs/GaAs quantum dot mid-infrared photodetectors on silicon substrates," *ACS Photonics*, vol. 3, no. 5, pp. 749–753, 2016.

[2] W. Chen *et al.*, "Demonstration of InAs/InGaAs/GaAs Quantum Dots-in-a-Well Mid-Wave Infrared Photodetectors Grown on Silicon Substrate," *Journal of Lightwave Technology*, vol. 36, no. 13, pp. 2572–2581, 2018.

[3] A. Barve, S. Lee, S. Noh, and S. Krishna, "Review of current progress in quantum dot infrared photodetectors," *Laser & Photonics Reviews*, vol. 4, no. 6, pp. 738–750, 2009.

[4] S. Nejad, M. Pourmahyabadi, and A. Amidian, "Optimal dark current reduction in quantum well 9 μm GaAs/AlGaAs infrared photodetectors with improved detectivity," in *2006 13th IEEE International Conference on Electronics, Circuits and Systems*, IEEE, 2006.

[5] R. Rehm *et al.*, "Dual-colour thermal imaging with InAs/GaSb superlattices in mid-wavelength infrared spectral range," *Electronics Letters*, vol. 42, no. 10, p. 577, 2006.

[6] J. Wu, S. Chen, A. Seeds, and H. Liu, "Quantum dot optoelectronic devices: lasers, photodetectors and solar cells," *Journal of Physics D: Applied Physics*, vol. 48, no. 36, p. 363001, 2015.

[7] S. Krishna *et al.*, "Three-color ($\lambda_{p1} \sim 3.8\ \mu m$,$\lambda_{p2} \sim 8.5\ \mu m$,$\lambda_{p3} \sim 23.2\ \mu m$) InAs/InGaAs quantum-dots-in-a-well detector," *Applied Physics Letters*, vol. 83, no. 14, pp. 2745–2747, 2003.

[8] S.-Y. Lin *et al.*, "Voltage-tunable two-color quantum-dot infrared photodetectors," *Applied Physics Letters*, vol. 95, no. 12, p. 123504, 2009.

[9] Z. Chen, E.-T. Kim, and A. Madhukar, "Normal-incidence voltage-tunable middle- and long-wavelength infrared photoresponse in self-assembled InAs quantum dots," *Applied Physics Letters*, vol. 80, no. 14, pp. 2490–2492, 2002.

[10] Z. Ye *et al.*, "InAs quantum dot infrared photodetectors with $\mathrm{In_{0.15}Ga_{0.85}As}$ strain-relief cap layers," *Journal of Applied Physics*, vol. 92, no. 12, pp. 7462–7468, 2002.

[11] H. Wang, D. Ning, and S. Feng, "Temperature dependence of the optical properties of InAs/GaAs self-organized quantum dots with bimodal size distribution," *Journal of Crystal Growth*, vol. 209, no. 4, pp. 630–636, 2000.

[12] H. Lee, R. R. Lowe-Webb, W. Yang, and P. C. Sercel, "Formation of InAs/GaAs quantum dots by molecular beam epitaxy: Reversibility of the islanding transition," *Applied Physics Letters*, vol. 71, no. 16, pp. 2325–2327, 1997.

[13] S. Jung *et al.*, "Photoluminescence study on the growth of self-assembled InAs quantum dots: Formation characteristics of bimodal-sized quantum dots," *Physica E: Low-dimensional Systems and Nanostructures*, vol. 33, no. 1, pp. 280–283, 2006.

[14] K. H. Schmidt *et al.*, "Size distribution of coherently strained InAs quantum dots," *Journal of Applied Physics*, vol. 84, no. 8, pp. 4268–4272, 1998.

[15] S. Liang, H. L. Zhu, and W. Wang, "Temperature-dependent bimodal size evolution of InAs quantum dots on vicinal GaAs(100) substrates," *Journal of Applied Physics*, vol. 100, no. 10, p. 103503, 2006.

[16] C.-M. Lee *et al.*, "Three-modal size distribution of self-assembled InAs quantum dots," *Japanese Journal of Applied Physics*, vol. 44, no. 4A, pp. 2037–2040, 2005.

[17] M. Syperek *et al.*, "Time-resolved photoluminescence spectroscopy of an InGaAs/GaAs quantum well-quantum dots tunnel injection structure," *Applied Physics Letters*, vol. 96, no. 1, p. 011901, 2010.

[18] Y. I. Mazur *et al.*, "Interdot carrier transfer in asymmetric bilayer InAs/GaAs quantum dot structures," *Applied Physics Letters*, vol. 86, no. 6, p. 063102, 2005.

[19] J. W. Tomm *et al.*, "Transient luminescence of dense InAs/GaAs quantum dot arrays," *Physical Review B*, vol. 67, no. 4, 2003.

[20] J.-Y. Duboz, H. C. Liu, Z. R. Wasilewski, M. Byloss, and R. Dudek, "Tunnel current in quantum dot infrared photodetectors," *Journal of Applied Physics*, vol. 93, no. 2, pp. 1320–1322, 2003.

[21] A. Stiff-Roberts, X. Su, S. Chakrabarti, and P. Bhattacharya, "Contribution of Field-Assisted Tunneling Emission to Dark Current in InAs/GaAs Quantum Dot Infrared Photodetectors," *IEEE Photonics Technology Letters*, vol. 16, no. 3, pp. 867–869, 2004.

[22] W. Zhang, H. Lim, M. Taguchi, S. Tsao, B. Movaghar, and M. Razeghi, "High-detectivity InAs quantum-dot infrared photodetectors grown on InP by metal-organic chemical-vapor deposition," *Applied Physics Letters*, vol. 86, no. 19, p. 191103, 2005.

[23] W. Q. Ma *et al.*, "Voltage tunable two-color InAs/GaAs quantum dot infrared photodetector," *Applied Physics Letters*, vol. 93, p. 013502, jul 2008.

[24] D. Pal, L. Chen, and E. Towe, "Intersublevel photoresponse of (In,Ga)As/GaAs quantum-dot photodetectors: Polarization and temperature dependence," *Applied Physics Letters*, vol. 83, no. 22, pp. 4634–4636, 2003.

[25] L. Lin *et al.*, "Sequential coupling transport for the dark current of quantum dots-in-well infrared photodetectors," *Applied Physics Letters*, vol. 97, no. 19, p. 193511, 2010.

[26] Y. H. Kang, J. Park, U. H. Lee, and S. Hong, "Effect of the dot size distribution on quantum dot infrared photoresponse and temperature-dependent dark current," *Applied Physics Letters*, vol. 82, no. 7, pp. 1099–1101, 2003.

[27] P. Martyniuk and A. Rogalski, "Insight into performance of quantum dot infrared photodetectors," *Bulletin of the Polish Academy of Sciences: Technical Sciences*, vol. 57, no. 1, 2009.

[28] L. Jiang *et al.*, "$\mathrm{In_{0.6}Ga_{0.4}As}$/GaAs quantum-dot infrared photodetector with operating temperature up to 260 K," *Applied Physics Letters*, vol. 82, no. 12, pp. 1986–1988, 2003.

[29] S. Chakrabarti *et al.*, "High-temperature operation of InAs-GaAs quantum-dot infrared photodetectors with large responsivity and detectivity," *IEEE Photonics Technology Letters*, vol. 16, no. 5, pp. 1361–1363, 2004.

[30] A. D. Stiff, S. Krishna, P. Bhattacharya, and S. Kennerly, "High-detectivity, normal-incidence, mid-infrared ($\lambda \sim 4\mu$m) InAs/GaAs quantum-dot detector operating at 150 K," *Applied Physics Letters*, vol. 79, no. 3, pp. 421–423, 2001.

[31] D. Guo *et al.*, "Two-colour $\mathrm{In_{0.5}Ga_{0.5}As}$ quantum dot infrared photodetectors on silicon," *Semiconductor Science and Technology*, vol. 33, no. 9, p. 094009, 2018.

[32] B. Kochman *et al.*, "Absorption, carrier lifetime, and gain in InAs-GaAs quantum-dot infrared photodetectors," *IEEE Journal of Quantum Electronics*, vol. 39, no. 3, pp. 459–467, 2003.

[33] V. Mitin, A. Sergeev, N. Vagidov, and S. Birner, "Improvement of QDIP performance due to quantum dots with built-in charge," *Infrared Physics & Technology*, vol. 59, pp. 84–88, 2013.

Chapter 5

Sub-monolayer Quantum Dot Quantum Cascade Infrared Photodetectors on GaAs and Si substrates

5.1 Introduction

In the last chapter, we have discussed the growth and characterisation of InGaAs/GaAs QDIPs on Si substrates. The noise of a QDIP is mainly determined by its dark current-related G-R noise. This chapter introduces infrared detectors based on a quantum cascade design, the quantum cascade detector (QCD), which can offer better noise performance [1, 2]. As mentioned in Chapter 2, each period of the quantum cascade structure is made of an active absorber and a series of QWs forming the "LO-phonon stairs or ladders". Since the photoelectrons can flow through the device via the phonon ladders without needing an external voltage, the device dark current and the dark current-related noise are dramatically reduced in comparison with similar QDIPs. QCDs with QW absorbers have been reported for a wide range of wavelengths from the near-IR to the THz regions [3–6]. However, these techniques require careful engineering in order to meet the target wavelength,

hence reducing the flexibility and fault tolerance. Another approach is to replace the QW absorber with a QD absorber. Owing to the 3D carrier confinement, QDs are sensitive to radiation at normal incidence. Moreover, the discrete energy levels reduce the generation of thermionic dark current, which in turn increases the device resistance and decreases the thermal noise. Brave and Krishna reported the first GaAs based Stranski-Krastanov (S-K) QD QCD [7]. In their work, an InAs/InGaAs/GaAs/AlGaAs confinement-enhanced DWELL structure was designed as the absorber. However, the structure is complex and difficult to grow. Huang et al. reported a QCD using sub-monolayer quantum dots (SML QDs) as the absorber [8]. Compare with the S-K QDs, the SML QDs have the advantages of better carrier confinement and higher dot areal density, which in turn lead to lower dark current and higher absorption quantum efficiency [9, 10].

This chapter compares the performances of SML QD QCDs on GaAs and Si substrates. In the following parts, "QCD-GaAs" denotes the SML QD QCDs grown on lattice-matched GaAs substrate, and "QCD-Si" denotes the SML QD QCDs grown on lattice-mismatched Si substrate. As we shall see, the two QCDs show nearly identical photoresponse behaviours with two primary peaks at ~ 6.1 μm and ~ 6.5 μm. The QCD-GaAs has lower thermal noise than the QCD-Si, leading to a 27 times higher Johnson noise-limited detectivity at 77 K. At 160 K, the two detectors perform at the same level in terms of the Johnson noise-limited detectivity.

5.2 Material Growth and Device Fabrication

The SML QD QCDs were grown by a solid-source Veeco Gen-930 molecular beam epitaxy system. The structure of the QCD-Si is shown in Figure 5.1 (a). The growth took place on a Si (001) substrate with a 4° offcut towards the [01-1] plane. Prior to the growth, the substrate was deoxidised in a high vacuum environment at $900\ ^{\circ}\mathrm{C}$ for 30 minutes. The Si substrate was then transferred to the growth chamber for the growth of 5 nm AlAs and

25 nm GaAs nucleation layers by migration-enhanced epitaxy at 370 °C. After the nucleation layer, a 970 nm GaAs buffer was deposited at 610 °C in order to ensure a high quality GaAs buffer and increase the dislocation movement. Two sets of DFLs were grown on top of the GaAs buffer layer. Each DFL contained ten periods of 10 nm $In_{0.15}Ga_{0.85}As$/ 10 nm GaAs superlattices and a 350 nm GaAs spacer.

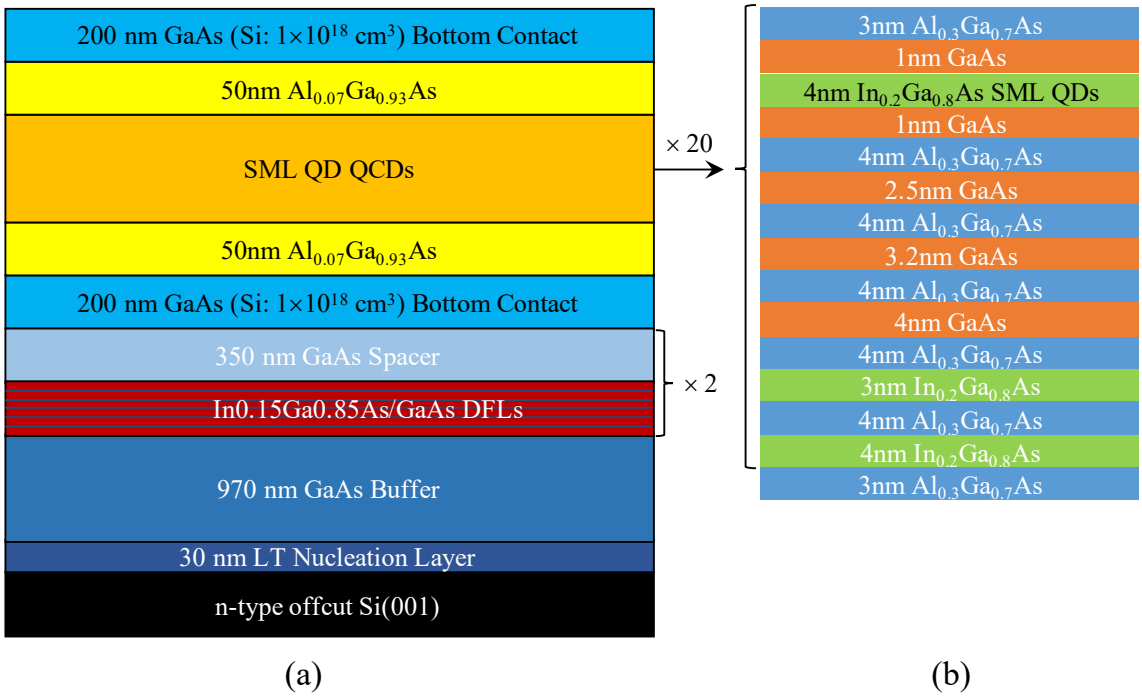

Figure 5.1: Schematic diagram of (a) the QCD-Si and (b) the heterostructure of the QCD active region.

The SML QD QCDs were grown in the following sequence, as shown in Figure 5.1 (b). Underlines highlight the well and SML QD layers: 3 nm $Al_{0.3}Ga_{0.7}As$, 4 nm $In_{0.2}Ga_{0.8}As$, 4 nm $Al_{0.3}Ga_{0.7}As$, 3 nm $In_{0.2}Ga_{0.8}As$, 4 nm $Al_{0.3}Ga_{0.7}As$, 4 nm GaAs, 4 nm $Al_{0.3}Ga_{0.7}As$, 3.2 nm GaAs, 4 nm $Al_{0.3}Ga_{0.7}As$, 2.5 nm GaAs, 4 nm $Al_{0.3}Ga_{0.7}As$, 1 nm GaAs, 4 nm SML QDs and 1 nm GaAs. The SML QD layer, which has an alloy composition equivalent to $In_{0.2}Ga_{0.8}As$, consists of five stacks of alternating deposition of 0.57 ML InAs and 2.26 ML GaAs. The SML QD layer was directly doped with a

Si dopant concentration of 1×10^{17} cm^{-3}. The three GaAs/AlGaAs QWs and the two succeeding InGaAs/AlGaAs QWs were designed to form the LO-phonon stairs for the cascade transport. Figure 5.2 gives a visualisation of the SML QD QCD structure and will be referred to in the following sections.

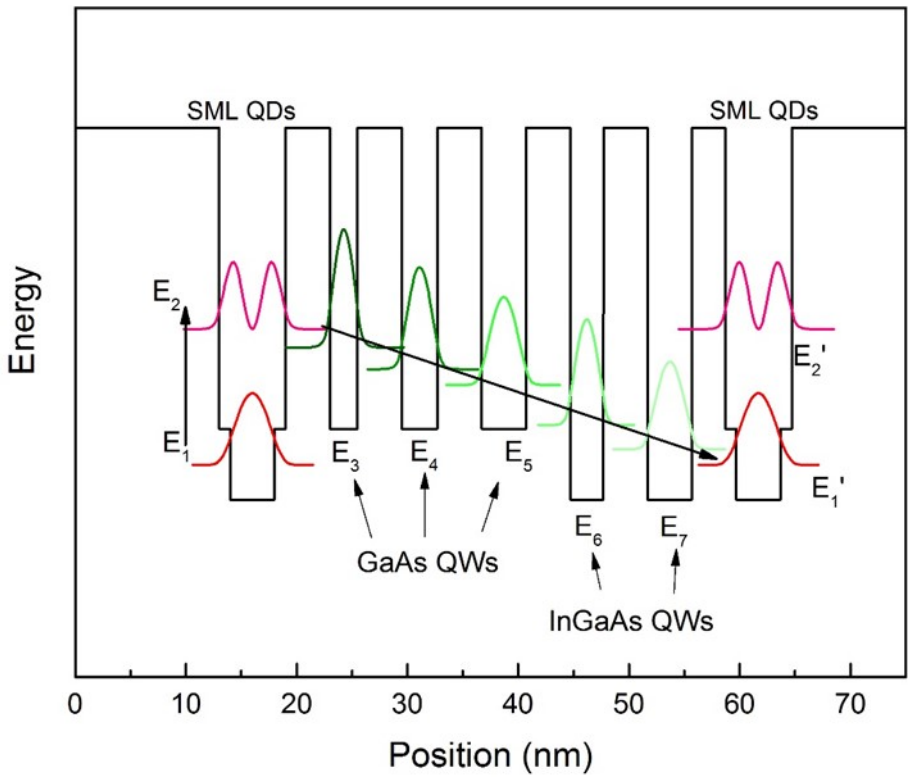

Figure 5.2: Conduction band profile of the SML QD QCD structure.

After the material growth, the detectors were fabricated into circular mesa structures with diameters from 100 μm to 1000 μm. The detector mesa was defined by photolithography and wet chemical etching. The etching solution is a mixture of H_2SO_4:H_2O_2:H_2O = 1:10:80. The top and bottom contacts were deposited by thermal evaporation of Ni/ GeAu/ Ni/ Au (10 nm/100 nm/30 nm/300 nm). The metals/alloy were annealed at 380 °C for 60 s to form the ohmic contact. The detectors were wire-bonded using Au wires on chip carriers for the photoresponse and blackbody measurements.

5.3 Material Characterisations

In the last chapter, the InGaAs QDIPs were grown on a GaAs-on-Si virtual substrate with four sets of DFLs. The number of DFL sets was reduced to two when growing the QCD-Si. Admittedly, reducing the number of DFL sets is likely to worsen the TDD. However, retaining four DFL sets will magnify the thermal mismatch issue and aggravate the thermal crack problem. Therefore, in order to mitigate the thermal crack problem and maintain a relative low TDD, the QCD-Si utilises two sets of DFLs. Figure 5.3 shows the high-resolution cross-sectional TEM image of the virtual substrate of the QCD-Si. The two sets of DFLs are labelled with white dash lines in Figure 5.3. The threading dislocation density (TDD) was reduced by about 100 times when comparing the TDDs before and after the DFL region.

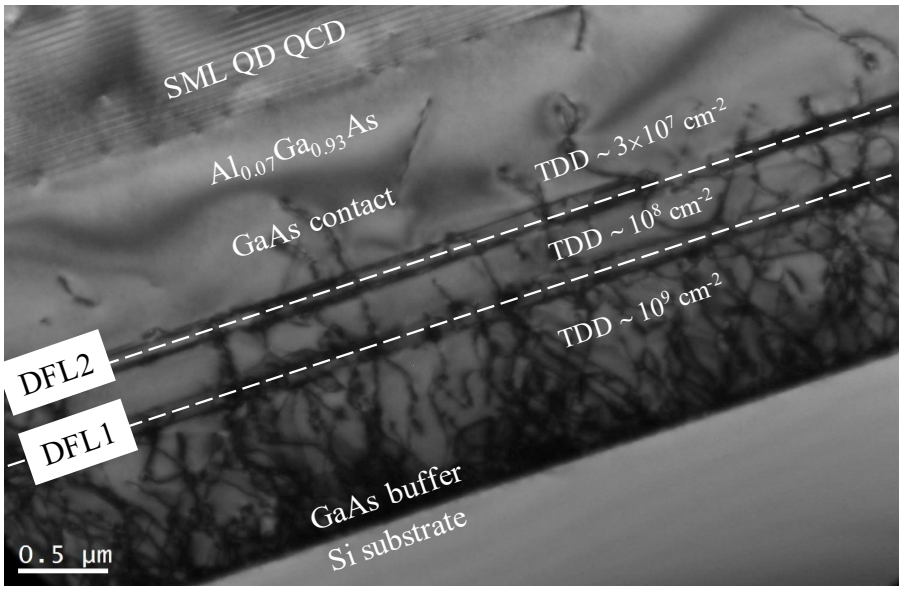

Figure 5.3: Bright field TEM image showing the GaAs-on-Si virtual substrate. The threading dislocation density (TDD) is about 3×10^7 cm^{-2} after the second dislocation filter layer (DFL2).

In order to characterise the optical properties of the samples, power dependent PL measurements were carried out at 10 K. A frequency-doubled Nd:YAG laser (λ = 532 nm)

with various laser power densities from 0.003 $\mathrm{W/cm^2}$ to 5000 $\mathrm{W/cm^2}$ was used as the optical source. The normalised power dependent PL spectra of two samples are shown in Figure 5.4 (a) and (b). For the PL measured under low excitation intensities (0.003 $\mathrm{W/cm^2}$ to 10 $\mathrm{W/cm^2}$), there are four peaks which can easily be distinguished from each figure. The peak at $\sim$1.49 eV for QCD-GaAs and the peak at $\sim$ 1.47 eV for QCD-Si can be attributed to the emission from the bulk GaAs. The bulk GaAs peak for QCD-GaAs is mainly coming from the fully relaxed GaAs substrate, while the peak at $\sim$ 1.47 eV in QCD-Si is the emission from the highly strained GaAs buffer layer. Thus, the redshift of the bulk GaAs energy peak in QCD-Si is due to the strain-induced bandgap shift [12]. With further increase of the excitation power, the SML QDs states are saturated, and the emissions of the cascade QWs dominate the PL emission spectra. Table 5.1 gives the PL information with excitation power density of 0.1 $\mathrm{W/cm^2}$.

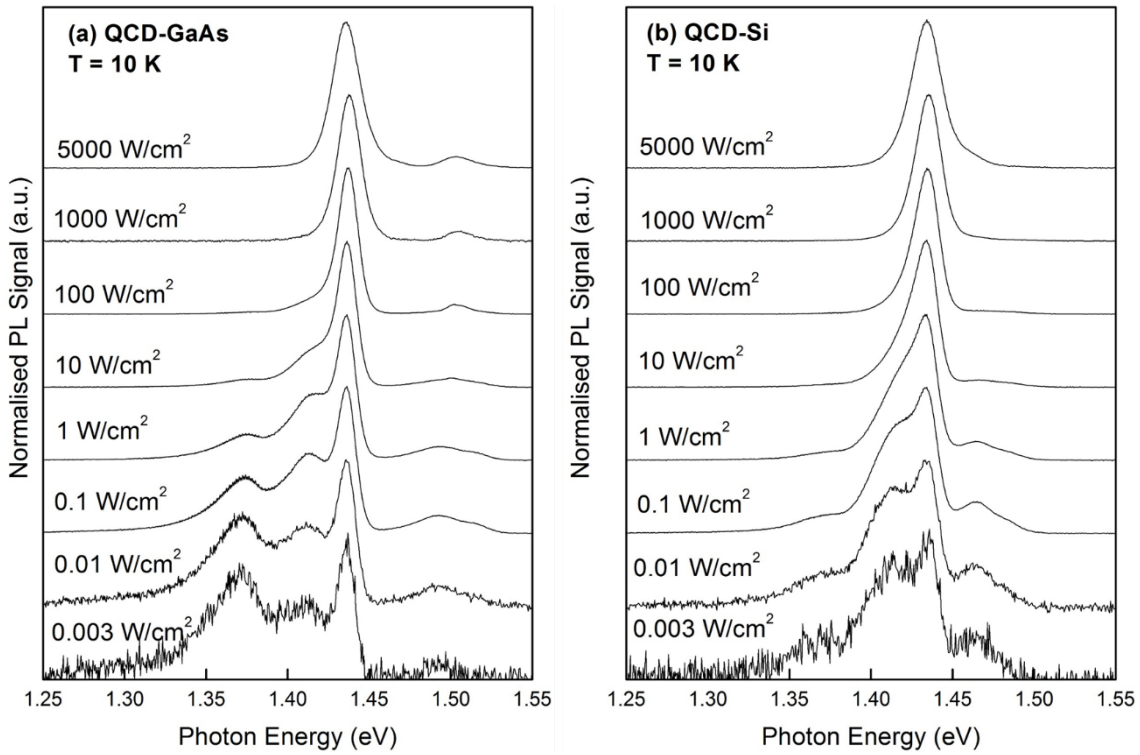

Figure 5.4: Normalised power dependent PL spectra for the samples (a) QCD-GaAs and (b) QCD-Si at 10 K.

Table 5.1: Summarised PL peak information. Peak positions and FWHM values of the PL measured under the excitation power density of 0.1 $\mathrm{W/cm^2}$ at 10 K. Bulk GaAs peaks are not included in the table. The fitting results were extracted by using OriginLab.

QCD-GaAs			
Peak Position (eV)	1.37	1.42	1.44
FWHM (meV)	35	27	10
QCD-Si			
Peak Position (eV)	1.37	1.42	1.44
FWHM (meV)	41	29	12

From the Table 5.1, the peak positions of the two samples are nearly the same and later we will see that the photoresponse results are nearly identical, meaning that the QCD design can be replicated on Si substrates. The lowest peak with photon energy 1.37 eV can be attributed to the ground state emissions of the SML QDs. The high energy peaks, 1.42 eV and 1.44 eV, are the emissions from the cascade QWs. The FWHM values of the QCD-Si are slightly higher than the values of QCD-GaAs, which may due to the residual strain left in the QCD-Si sample or poorer surface roughness.

5.4 Device Characterisations

After the material characterisations, the two samples were processed into circular photodetectors with diameter of 210 μm using photolithography and wet chemical etching to the bottom GaAs contact layer. Ni/AuGe/Ni/Au (10 nm/100 nm/30 nm/300 nm) metallic films were deposited at the top and bottom GaAs contacts and followed by rapid thermal annealing at 380 $^{\circ}\mathrm{C}$ for 60 s to form ohmic contacts. The QCDs were placed in a liquid nitrogen cooled probe station for dark current measurement. A temperature cooling system was used to adjust the measurement temperatures from 77 to 300 K. The positive-biased

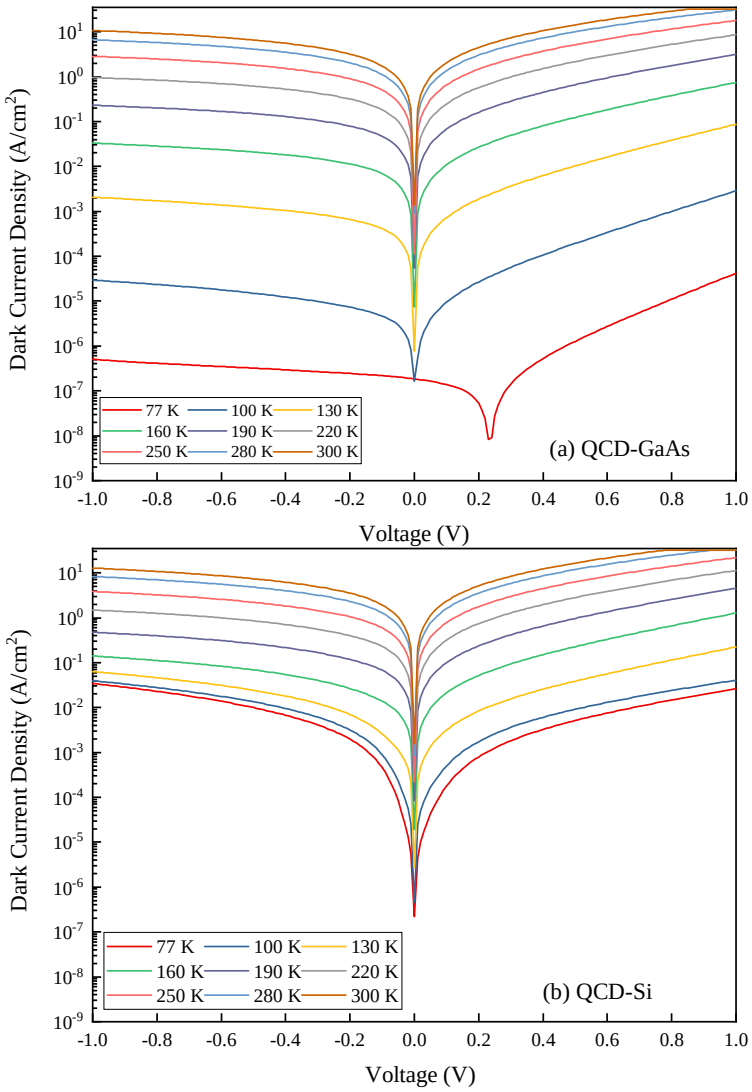

Figure 5.5: Dark current density-voltage results measured at the temperatures from 77 K to 300 K. (a) QCD-GaAs and (b) QCD-Si.

dark current was measured when connecting the positive terminal to the top contact, and the negative-biased dark current was measured when the positive terminal was connected to the bottom contact. Figure 5.5 (a) shows the dark current density-voltage results of the QCD-GaAs measured at different temperatures. At 77 K, the lowest dark current density is 8.3×10^{-9} A/cm^2 at + 0.24 V. The small departure of the lowest dark current value from the zero-volt point may be caused by imperfect shielding of the low temperature

probe station, meaning that the testing environment was not completely dark for the detectors. Referring to Figure 5.1, the potential drops in the contrary direction to the growth direction. A small portion of the infrared leakage will result in the flow of photocurrent following the potential difference, i.e. from top contact to the bottom contact. Under small positive bias voltage condition (0 to + 0.24 V), electrons are injected from the bottom contact to the top contact, which is in the opposite direction to the photocurrent flow, resulting in a gradually reduced net electron flow and hence a lower dark current. When the positive bias exceeds + 0.24 V, the dark current increases with the voltage.

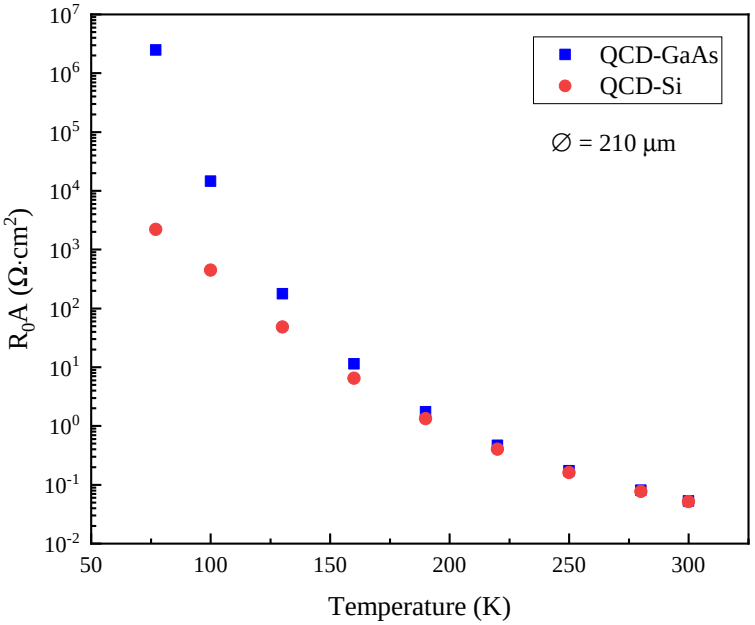

Figure 5.6: Calculated zero bias differential resistance-area products ($\mathrm{R_0A}$) of (a) QCD-GaAs and (b) QCD-Si at the temperatures from 77 to 300 K.

Johnson (or thermal) noise is the major internal noise component of a QCD that operates in PV mode. The Johnson noise depends on the zero-bias resistance, $\mathrm{R_0}$, of the detector according to [13],

$$I_{n,J} = \sqrt{\frac{4k_BT\Delta f}{R_0}} \tag{5.1}$$

where $1/\mathrm{R_0} = \mathrm{dI/dV}$ evaluate at V = 0, k_B is the Boltzmann constant, Δf is the noise

bandwidth and T is the operating temperature. Since the resistance of a detector is inversely proportional to the detector area, the product of zero bias resistance and detector area (R_0A) is often reported. The R_0A values of the two devices are plotted in Figure 5.6. At 77 K, the calculated R_0A products are $2.5 \times 10^9\ \Omega \cdot \mathrm{cm}^2$ and $2.2 \times 10^3\ \Omega \cdot \mathrm{cm}^2$ for QCD-GaAs and QCD-Si, respectively. The 6 orders of magnitude difference can be explained by the different diagonal transitions occurring in the two detectors, see the Arrhenius fitting in Figure 5.8 and related content. As the temperature increased to 160 K, the R_0A products decreased to $11.32\ \Omega \cdot \mathrm{cm}^2$ and $6.45\ \Omega \cdot \mathrm{cm}^2$ for QCD-GaAs and QCD-Si, respectively. Room temperature R_0A products were $0.058\ \Omega \cdot \mathrm{cm}^2$ and $0.051\ \Omega \cdot \mathrm{cm}^2$ for QCD-GaAs and QCD-Si, respectively.

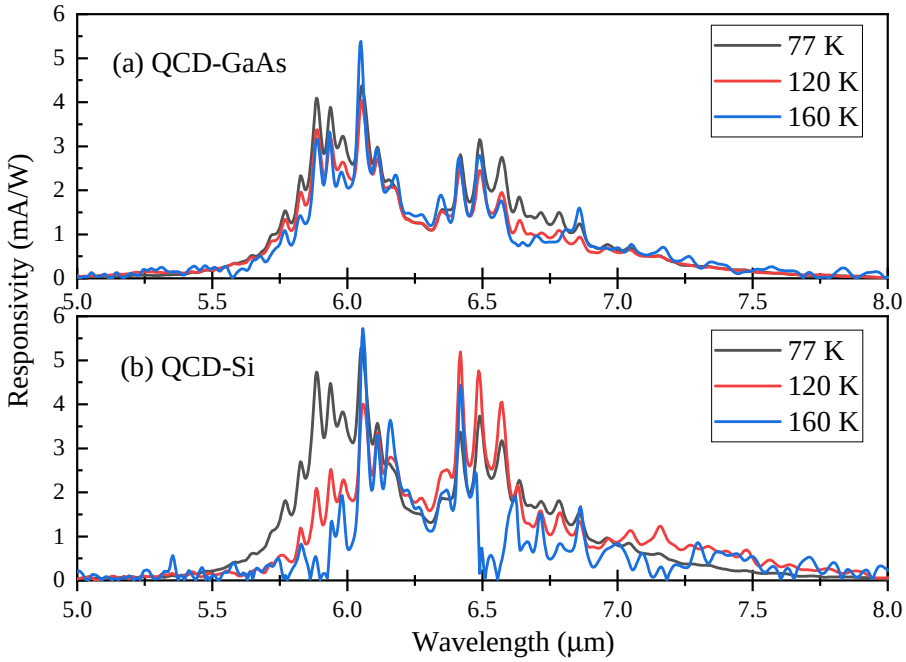

Figure 5.7: Normal-incidence zero-bias absolute responsivities of (a) QCD-GaAs and (b) QCD-Si measured at the temperatures of 77 K, 120 K and 160 K. Device diameter = 210 μm.

The relative photoresponse curves of the two detectors were measured using a Nicolet iS50 Fourier transform spectrometer. A 700 °C blackbody source with modulation

frequency of 140 Hz was used to calibrate the absolute responsivity. The detectors with diameter of 210 μm were tested in normal incidence configuration. Figure 5.7 shows the spectral responsivity results of QCD-GaAs and QCD-Si at the temperatures of 77 K, 120 K and 160 K. The 77K responsivity curves of the two detectors are nearly identical indicating the SML QCD structure is able to mitigate the impact of defects on photocurrent. The broad photoresponse peaks of the QCDs indicate the inhomogeneous size distribution of the SML QDs. The two peaks, centred at $\sim$ 6.1 μm and $\sim$ 6.5 μm, suggest there are two predominate transitions coexisting in the SML QD QCDs [9]. Referring back to Figure 5.2, the high energy peak corresponds to the transition energy between E1 and E2, and the low energy response peak could be attributed to the optical transition energy from E1 to E3. Another possible explanation is the two transitions coexist within the SML QDs region corresponding to the transition energies from the SML QD ground state to two excited states in the GaAs/AlGaAs QWs, i.e. there are two E1 to E2 transitions within the SML QD region. It is worth noting that the responsivities of the QCD-GaAs and QCD-Si are less than 10 mA/W at all temperatures. Such low responsivity may be caused by (i) the low absorption QE associated with the intersubband QD absorber and (ii) low photoconductive gain due to the 20 period of QCDs ($\mathrm{g_{ph}} \propto 1/\mathrm{N}$, where N is the number of cascade periods). One interesting observation is that the photoresponse curves of QCD-Si become narrower as the temperature increases and the intensity subsides around 6.5 μm at 160 K. The origin is unknown, and it is not observed in QCD-GaAs. One possibility can be attributed to the differences between QCD-Si and QCD-GaAs, for example, table 5.1 listed that the FWHM values of QCD-Si are slightly larger than the QCD-GaAs. At 77 K, the photoresponse curves of both detectors are made up of several transitions in the SML QD QCD structure. As the temperature goes up, the transitions in QCD-GaAs are nearly unchanged, while some of the transitions in QCD-Si might be suppressed due to changes in detector structure with temperature (e.g. the differences in strain can be amplified as the temperature rises).

To analyse the dark current generation mechanism, the R_0A products were fitted with the Arrhenius equation as given previously, Equation 4.1. In Figure 5.8 (a), the fitted activation energy is $E_{a,QCD-GaAs}$ = 159.3 meV for QCD-GaAs. This activation energy is smaller than the energy difference of E1 to E2 and E1 to E3, see Figure 5.2. Therefore, the dark current activation energy corresponds to the thermally excited transition energy between E1 and E4 [14]. The R_0A fitting result of QCD-Si is shown in Figure 5.8 (b). The activation energy is $E_{a,QCD-Si}$ is about 120 meV, which roughly equals the transition energy of E1 to E5. The lower dark current activation energy in QCD-Si is responsible for the lower R_0A values as mentioned previously. To increase the activation energy and R_0A of the QCD-Si, the spatial separation of the E1 and the E5 QWs should be increased [15]. One possible approach is to add an E4 QW in between the E4 and E5 QWs. In this design, the R_0A would be increased, due to the reduced E1 to E5 oscillator strength, while the phonon ladder has little effect, so the responsivity could be maintained. In the end, an improvement in detectivity is obtainable with the increased R_0A.

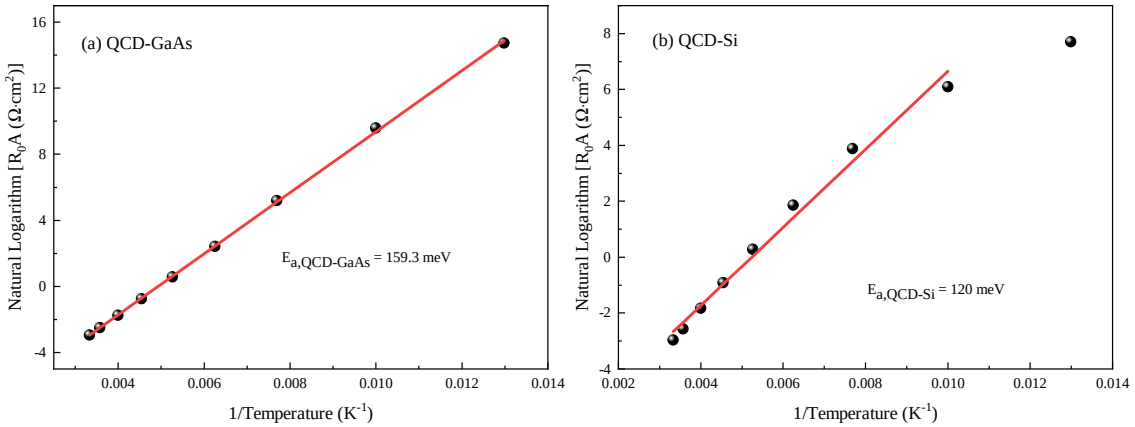

Figure 5.8: Natural logarithm R_0A products versus 1/temperature for (a) QCD-GaAs and (b) QCD-Si. The R_0A activation energies for QCD-GaAs and QCD-SI are fitted as $E_{a,QCD-GaAs} = 159.3$ meV and $E_{a,QCD-Si} = 120$ meV, respectively.

The Johnson noise-limited detectivities for the two detectors at 77 K and 160 K were calculated and plotted in Figure 5.9. The Johnson noise-limited detectivity, (D^*_J), can be

obtained by using equation 5.2[16],

$$D_J^* = R_i \sqrt{\frac{R_0 A}{4 k_B T}} \tag{5.2}$$

where R_i is the current responsivity. The peak Johnson noise-limited detectivity of the

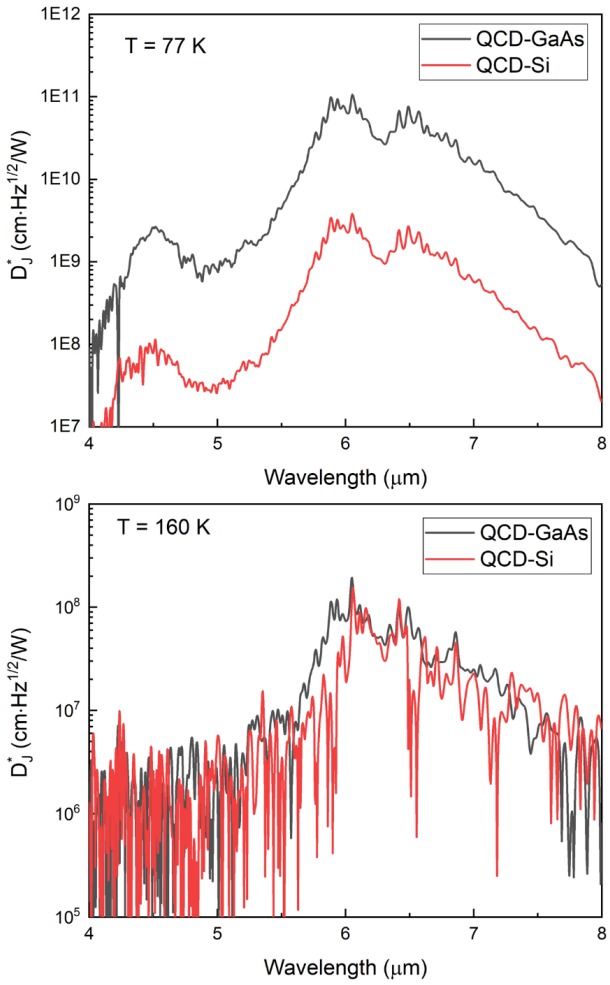

Figure 5.9: Johnson noise-limited detectivity of QCD-GaAs (black line) and QCD-Si (red line) in the detectors measured at 77 K and 160 K.

QCD-GaAs device is 1.06×10^{11} cm $\cdot$ Hz$^{1/2}$/W at 77 K. Due to the low R_0A product, the peak Johnson noise-limited detectivity of QCD-Si is lower at 3.83×10^{9} cm $\cdot$ Hz$^{1/2}$/W. At 160 K, the peak Johnson noise-limited detectivities drop to 1.98×10^{8} cm $\cdot$ Hz$^{1/2}$/W and

1.55×10^8 cm $\cdot$ Hz$^{1/2}$/W for QCD-GaAs and QCD-Si, respectively, due to the increased Johnson noise.

Table 5.2 compares the reported QCDs from other research groups with the work presented in this chapter. The R_0A value of the QCD-GaAs in this work is about two orders of magnitude higher than the R_0A reported in Ref. [17]. This can be attributed to the better carrier confinement of the SML QDs. In Ref. [16], a high value of R_0A is reported based on the GaAs/AlGaAs QW QCD, which could be due to the increased number of cascade periods. Typically, the resistance of a QCD increases with the number of cascade periods. However, the R_0A value reported in Ref.[18] is about two orders of magnitude higher than we measured for the QCD-GaAs. This may be caused by better QCD design and high InGaAs/InAlAs material quality on the InP substrate in Ref. [18].

Table 5.2: Comparison of reported QCDs with the QCDs in this work. N is the number of cascade period and λ_p is the peak response wavelength.

Temperature (K)	N	λ_p (μm)	R_0A ($\Omega \cdot$ cm^2)	D^*_J (cm $\cdot$ Hz$^{1/2}$/W)	Notes	Ref.
78	15	4.5	1.68×10^4	2.43×10^{10}	InGaAs/InAlAs QW QCD on InP	[17]
78	50	8.81	9.7×10^6	2.7×10^{11}	GaAs/AlGaAs QW QCD on GaAs	[16]
80	20	4.3	$> 10^8$	3.64×10^{11}	InGaAs/InAlAs QD QCD on InP	[18]
77	20	6.1&6.5	2.5×10^6	1.06×10^{11}	QCD-GaAs	[this work]
77	20	6.1&6.5	2.21×10^3	3.83×10^9	QCD-Si	[this work]

5.5 Conclusion

SML QD QCDs have been grown on both GaAs and Si substrates with a measurable photoresponse up to 160 K. The high defect density in QCD-Si has a limited impact on detector's photoresponsivity. Dark current measurements and Arrhenius fitting reveal that additional diagonal transitions occur in both the QCD-GaAs and QCD-Si. The dark current activation energy of QCD-Si is smaller than in QCD-GaAs, which leads to the lower $\mathrm{R_0A}$ values in QCD-Si than the QCD-GaAs. The 77 K Johnson noise-limited detectivities are $1.06 \times 10^{11}\ \mathrm{cm \cdot Hz^{1/2}/W}$ and $3.83 \times 10^{9}\ \mathrm{cm \cdot Hz^{1/2}/W}$ for QCD-GaAs and QCD-Si, respectively. The higher detectivity of QCD-GaAs compared with QCD-Si is due to the lower thermal noise. Future work should focus on suppressing the unwanted thermally related diagonal transitions through a better structural design, e.g. increasing spatial separation between the diagonal transition energy states.

5.6 Contribution Statement

The SML QD QCD on Si and GaAs were designed by Dr. Jiang Wu, University College London, and Prof. Baile Chen, ShanghaiTech University. Dr. Jiang Wu carried out the MBE growth. TEM images and PL measurements were provided by Dr. Yuriy Mazur, University of Arkansas.

References

[1] D. Hofstetter, M. Beck, and J. Faist, "Quantum-cascade-laser structures as photodetectors," *Applied Physics Letters*, vol. 81, no. 15, pp. 2683–2685, 2002.

[2] L. Gendron, M. Carras, A. Huynh, V. Ortiz, C. Koeniguer, and V. Berger, "Quantum

cascade photodetector," *Applied Physics Letters*, vol. 85, no. 14, pp. 2824–2826, 2004.

[3] A. Vardi *et al.*, "Near infrared quantum cascade detector in GaN/AlGaN/AlN heterostructures," *Applied Physics Letters*, vol. 92, no. 1, p. 011112, 2008.

[4] F. R. Giorgetta *et al.*, "InGaAs/AlAsSb quantum cascade detectors operating in the near infrared," *Applied Physics Letters*, vol. 91, no. 11, p. 111115, 2007.

[5] F. R. Giorgetta *et al.*, "16.5μm quantum cascade detector using miniband transport," *Applied Physics Letters*, vol. 90, no. 23, p. 231111, 2007.

[6] G. Scalari *et al.*, "A THz quantum cascade detector in a strong perpendicular magnetic field," *Semiconductor Science and Technology*, vol. 21, no. 12, pp. 1743–1746, 2006.

[7] A. V. Barve and S. Krishna, "Photovoltaic quantum dot quantum cascade infrared photodetector," *Applied Physics Letters*, vol. 100, no. 2, p. 021105, 2012.

[8] J. Huang *et al.*, "Sub-monolayer quantum dot quantum cascade mid-infrared photodetector," *Applied Physics Letters*, vol. 111, no. 25, p. 251104, 2017.

[9] Y. Kim, J. O. Kim, S. J. Lee, and S. K. Noh, "Submonolayer quantum dots for optoelectronic devices," *Journal of the Korean Physical Society*, vol. 73, no. 6, pp. 833–840, 2018.

[10] S. Sengupta *et al.*, "Sub-monolayer quantum dots in confinement enhanced dots-in-a-well heterostructure," *Applied Physics Letters*, vol. 100, no. 19, p. 191111, 2012.

[11] S. Chen *et al.*, "Electrically pumped continuous-wave III-V quantum dot lasers on silicon," *Nature Photonics*, vol. 10, no. 5, pp. 307–311, 2016.

[12] M. Akiyama, Y. Kawarada, and K. Kaminishi, "Growth of Single Domain GaAs Layer on (100)-Oriented Si Substrate by MOCVD," *Japanese Journal of Applied Physics*, vol. 23, no. Part 2, No. 11, pp. L843–L845, 1984.

[13] S. Wolde *et al.*, "Noise, gain, and capture probability of p-type InAs-GaAs quantum-dot and quantum dot-in-well infrared photodetectors," *Journal of Applied Physics*, vol. 121, no. 24, p. 244501, 2017.

[14] F.-R. Jasnot *et al.*, "Description of transport mechanisms in a very long wave infrared quantum cascade detector under strong magnetic field," *Journal of Applied Physics*, vol. 112, no. 12, p. 123705, 2012.

[15] L. Li, X. Zhou, T. Lin, N. Li, Z. Zhu, and F. Liu, "Electronic transport in a long wavelength infrared quantum cascade detector under dark condition," *Infrared Physics & Technology*, vol. 78, pp. 72–76, 2016.

[16] J. Liu *et al.*, "High resistance AlGaAs/GaAs quantum cascade detectors grown by solid source molecular beam epitaxy operating above liquid nitrogen temperature," *Semiconductor Science and Technology*, vol. 25, no. 7, p. 075011, 2010.

[17] S. Zhai *et al.*, "Strain-compensated InP-based InGaAs/InAlAs quantum cascade infrared detectors for 3-5μm atmospheric window," in *International Symposium on Photoelectronic Detection and Imaging 2011: Advances in Infrared Imaging and Applications*, SPIE, 2011.

[18] X.-J. Wang and othres, "Quantum dot quantum cascade infrared photodetector," *Applied Physics Letters*, vol. 104, no. 17, p. 171108, 2014.

Chapter 6

InAs/GaSb T2SL Detectors on Si and GaAs Substrates

6.1 Introduction

The incorporation of the QCD with the SML QDs has shown the capability to operate under normal illumination at zero bias up to 160 K. However, the S-K QD and SML QD absorbers are relatively weak in optical absorption. To further improve the performance of infrared detectors on Si, this chapter studies InAs/GaSb T2SL photodetectors directly grown on Si and GaAs substrates. T2SLs have been considered as a promising material system in developing the next generation of infrared imagers owing to high material uniformity, adjustable bandgap, good absorption quantum efficiency, low Auger recombination rate and low tunnelling current. The performance of T2SL detectors has undergone a continuous improvement over the last few decades and T2SL infrared imagers are now commercially available in both the MWIR and LWIR regions. However, the performance of T2SL photodiodes is still inferior to state-of-the-art HgCdTe photodiodes, due to the short minority carrier lifetime as well as the high G-R current associated with the SRH generation mechanism. Several T2SL based heterojunctions were proposed in the past to

reduce the dark current and improve the carrier lifetime, such as nBn [1], pBn [2], and double heterostructures [3]. For example, the T2SL nBn detector acts as a minority carrier device, but without forming a p-n junction, thereby avoiding depletion region-related G-R current. In addition, the nBn structure is often described as a self-passivation detector, since the detector element can be defined by an etch stop at the top contact/barrier interface, where the wide bandgap barrier provides a natural insulation, preventing the exposure of the narrow bandgap absorber layer to the ambient [4].

Apart from the performance improvements, researchers are seeking a solution for low-cost manufacturing of large-format T2SL FPAs. Current T2SLs are mainly grown on native GaSb substrates, which are presently restricted in diameter to 4 inches [5]. As alternatives to the GaSb substrates, GaAs and Si substrates with larger available wafer size and lower cost per unit area are promising solutions for future large-format T2SL FPAs. To accommodate the large lattice mismatch during the heteroepitaxy, either the metamorphic buffer technique or interfacial misfit (IMF) growth technique can be adopted as a solution to reduce the threading dislocations. The metamorphic technique has the shortcoming of requiring a thick buffer layer, leading to low thermal conduction and low electrical conductivity. The IMF growth technique involves nucleation of islands and coalescence of these islands to form a smooth surface. The strain energy is relieved through the formation of periodic 90° and 60° misfit dislocations (MDs) underneath the islands at the heteroepitaxy interface. The formation of 90° MDs is important to realise effective strain relaxation and low threading dislocation density, since the 90° MDs are the pure edge type dislocations spreading laterally along the [110] and [1-10] directions without generating vertical propagated TDs, while the 60° MD can develop into TD threading vertically along the $\{111\}$ planes to the device region [6, 7]. The growth temperature is an important factor in determining whether the epitaxy growth favours the 90° or 60° MD. Kim et al. studied the growth of GaSb on GaAs with substrate temperature ranging from 520-560 °C [8]. They found the strain energy is mainly relieved by the 90° MDs for the

growth temperature of 520 °C, while the 60° MDs are dominated at the GaSb/GaAs interface at 560 °C [8]. Other factors, such as island coalescence and the degree of mismatch between the substrate and epitaxial layer, are also important in determining the formation of 60° MDs at the heteroepitaxy interface [5]. By using the IMF technique, T2SL detectors demonstrated on highly mismatched substrates have shown promising results when compared with detectors on native substrates [9–11].

This chapter first introduces the InAs/GaSb T2SL p-i-n detectors on GaAs and Si substrates. As we will be discussed in more detail, strain relaxation occurs at the AlSb/Si interface, confirmed by the cross-sectional TEM. Measurements reveal that both the GaAs and Si samples exhibit high level of dark current. To improve the material quality, this chapter also introduces T2SL nBp barrier detector on GaAs substrates. The detector has a 50% cutoff wavelength at 6.4 μm (77 K). The dark current analysis shows a G-R limited dark current for the temperature below 130 K, and above 130 K, the dark current is dominated by the diffusion current.

6.2 InAs/GaSb T2SL Photodiode on Si Substrate

The InAs/GaSb SL p-i-n photodiodes were grown on a Si (001) substrate with a 4° offcut towards the [01-1] direction using a Solid-Source Veeco Gen 930 MBE system. The structure of the photodiode is illustrated in Figure 6.1. Prior to the growth the Si substrate was deoxidised at 900 °C for 30 minutes. After the deoxidisation process, the Si substrate was transferred to the MBE growth chamber to grow a 10 nm AlSb nucleation layer at 415 °C. The substrate temperature was then raised to about 515 °C for the growth of the buffer layer. The buffer layer consists of two repeats of 100 nm 10 ML AlSb/10 ML GaSb SLSs and 500 nm GaSb. The device region was grown at 400 °C and started with a 500 nm Si-doped 10 MLs InAs/ 10 MLs GaSb n-contact. The doping concentration was about 1×10^{18} cm^{-3}. A 2000 nm 10 MLs InAs/10 MLs GaSb non-intentionally doped (n.i.d)

absorber was grown after the Si doped bottom contact. The p-doped top contact includes 500 nm of 10 MLs InAs/10 MLs GaSb with a Be dopant concentration of $\sim 1\times10^{18}$ cm^{-3}. One ML of InSb was inserted in between the InAs/GaSb SL interfaces to compensate the strain. Finally, the growth was finished with a heavily p-doped 50 nm GaSb top contact layer. A reference InAs/GaSb photodiode was grown on a GaAs substrate with the same device structure. Before growing the device region, a 200 nm thick GaAs initial layer was grown on the GaAs substrate. The difference between the T2SL on Si and the reference sample is that the reference sample was immediately grown on 1 μm of GaSb buffer layer without the AlSb nucleation layer.

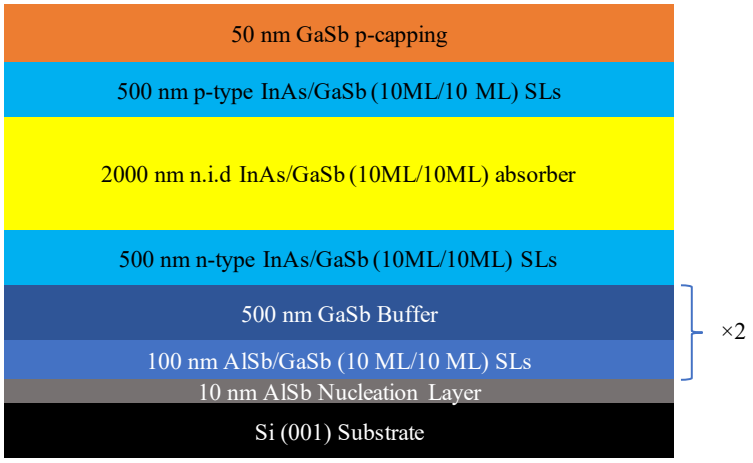

Figure 6.1: Cross-sectional view of the InAs/GaSb SL p-i-n photodiode on Si substrate. n-i-d = non-intentionally doped.

Figure 6.2 shows the (220) bright-field TEM image of the AlSb/Si interface, which displays Moiré fringe patterns at the AlSb/Si interface. The Moiré fringes are the interference patterns that are formed by the overlap of two crystal structures with different orientations or lattice constants, thus providing information on whether the epitaxial layer is strained [12]. The theoretical spacing between the Moiré fringes is [8],

$$d_m = \left(\frac{1}{d_{AlSb}} - \frac{1}{d_{Si}} \right)^{-1} \tag{6.1}$$

where $\mathrm{d_{AlSb}}$ and $\mathrm{d_{Si}}$ is the interplanar spacing of AlSb(220) and Si(220), respectively, which can be calculated by $(1/d_{hkl})^2 = (h^2 + k^2 + l^2)/a^2$, where h, k, and l are the Miller indices and a is the lattice constant. Giving the lattice constants, $a_{AlSb} = 0.6135$ nm and $a_{Si} = 0.543$ nm, the theoretical spacing of the Moiré fringes is about 1.67 nm for 220 reflections. The measured value of the space between Moiré fringes by TEM is about 1.64±0.06 nm, which is close to the the theoretical value, indicating the film is effectively relaxed at the AlSb/Si interface [12].

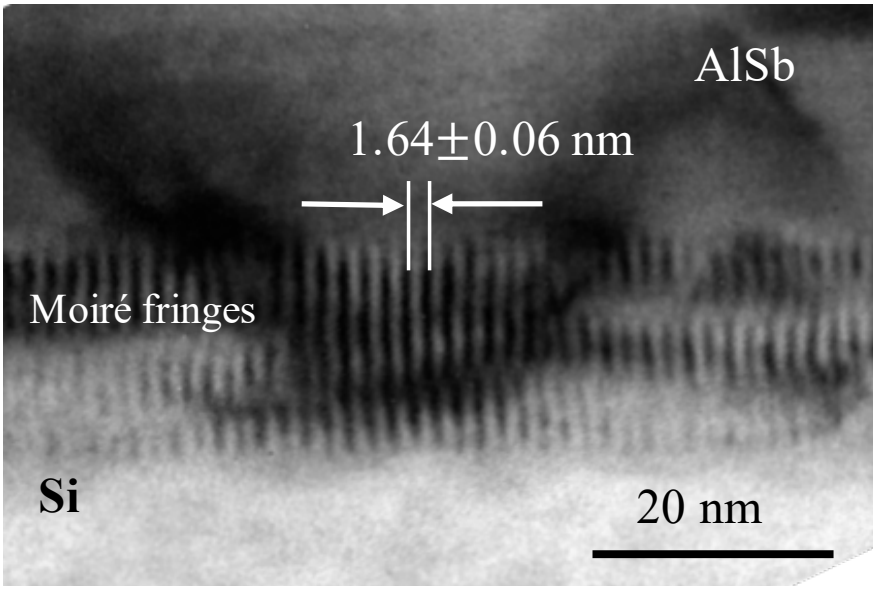

Figure 6.2: Cross-sectional (220) bright-field TEM image of the AlSb/Si interface. The average space between the Moiré fringes is about 1.64±0.06 nm.

To characterise the optical properties of the two samples, power-dependent PL was conducted. A 532 nm laser with different excitation powers from 100 mW to 600 mW was used as the excitation source. The optical signal was recorded by a liquid-nitrogen cooled InSb detector. Figure 6.3 (a) plots the power dependent PL results of the T2SL on GaAs and T2SL on Si. A blue shift is observable for the T2SL on Si with respect to the T2SL on GaAs. This may be attributed to the residual strain caused by the thermal expansion mismatch between the substrates and the epi-layers. The peak positions of both

samples shift to the shorter wavelength side with increased excitation power, which may be due to the filling of lower energy states in the SLs. The integrated PL results have been plotted in Figure 6.3 (b). The integrated PLs of both samples increase with the laser power, and the integrated PL of T2SL on Si is smaller than the T2SL on GaAs.

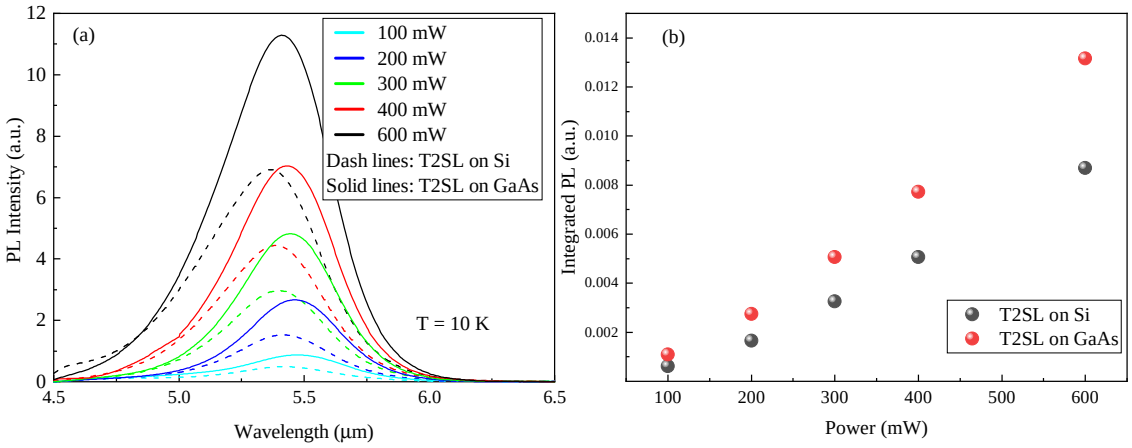

Figure 6.3: (a) Low temperature power dependent PL spectra for the T2SL on GaAs (solid lines) and the T2SL on Si (dash lines). (b) Integrated PL for the T2SL on Si (black) and T2SL on GaAs (red) under different excitation powers at 10 K.

To investigate the device performance, dark current measurements were conducted in a liquid nitrogen-cooled probe station, as shown in Figure 6.4. Under the reverse bias voltage of -0.05 V, the dark current densities were measured as 0.11 $\mathrm{A/cm^2}$ and 0.46 $\mathrm{A/cm^2}$ for the T2SLs on GaAs and Si, respectively. The high values of dark current can be attributed to the high level of G-R current associated with the SRH process and the surface leakage current. In order to improve the dark current performance, an alternative design, the nBp barrier detector, will be explored in the following section.

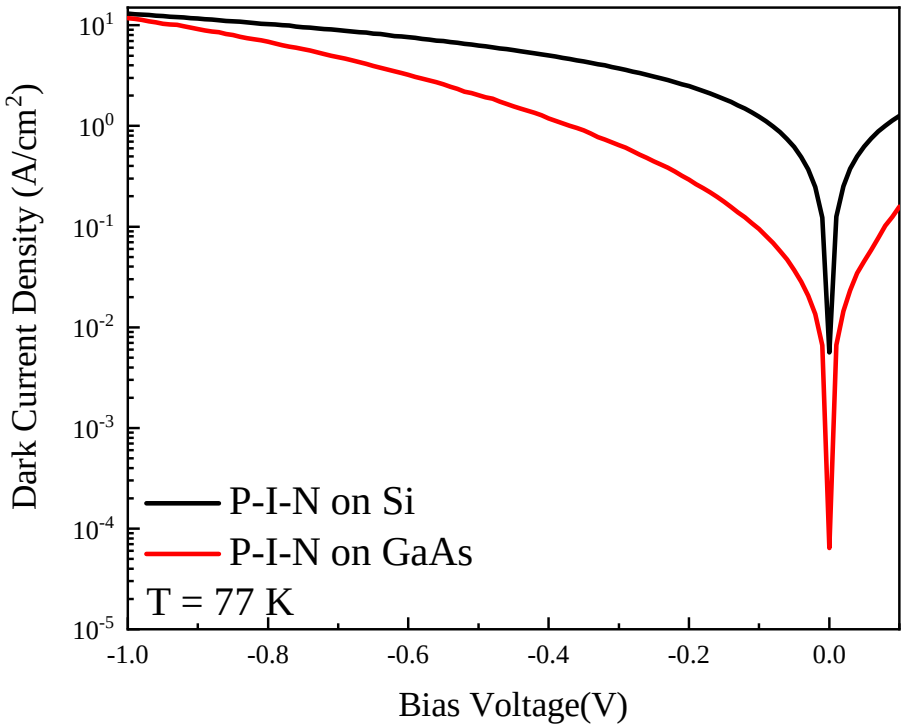

Figure 6.4: Dark current density-voltage characterisations of the T2SL on GaAs and Si measured at 77 K.

6.3 InAs/GaSb T2SL nBp Barrier Detector on GaAs

In this section, we discuss T2SL-based nBp barrier detectors which have been realised on GaAs substrates. The device consists of a n-doped top contact, a n-doped wide bandgap SL hole barrier and a p-doped narrow bandgap absorber. The energy band diagram of the nBp barrier detector is shown in Figure 6.5. In this design, most of the depletion electric field drops across the wide bandgap hole barrier, which reduces the G-R component of the dark current. Moreover, the pn junction formed at the n-doped barrier/p-doped absorber interface enables zero bias operation of the barrier detector.

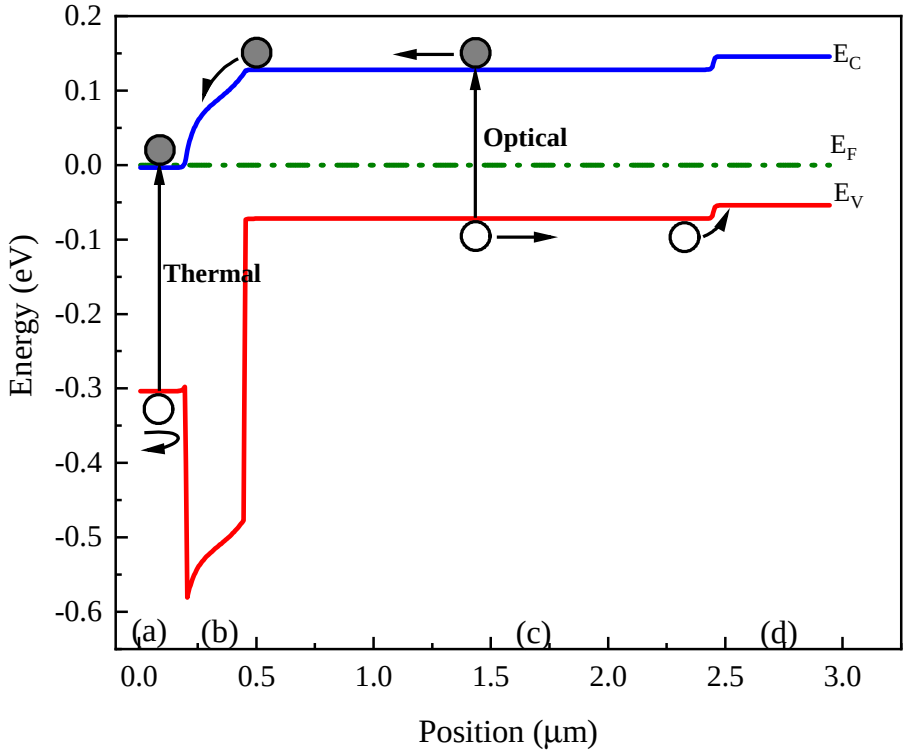

Figure 6.5: Energy band diagram of the nBp barrier detector with zero bias voltage. From left to right, (a) n-type top contact, (b) hole barrier, (c) absorber and (d) bottom contact. E_C, E_F and E_V are the effective conduction band edge, Fermi level and effective valence band edge, respectively.

The InAs/GaSb barrier detectors were grown on a GaAs (001) substrate using a Veeco 930 Solid-Source molecular beam epitaxy system. The cross-sectional view of the nBp device on GaAs is shown in Figure 6.6(a) The GaAs substrate was pre-treated at 590 $^{\circ}\mathrm{C}$ for oxide desorption. After the deoxidisation process, a 200 nm thick GaAs buffer was grown at 590 $^{\circ}\mathrm{C}$ to smooth the epitaxy surface. The substrate temperature was then reduced to 480 $^{\circ}\mathrm{C}$ for growing a 2000 nm GaSb buffer. The SL barrier detector region was grown at $400^{\circ}\mathrm{C}$, starting with a 500 nm heavily p-doped ($\mathrm{Si} : 1.5 \times 10^{18}$ cm^{-3}) 10 ML InAs/ 10 ML GaSb SL bottom contact. The absorber region is made of 2000 nm p-doped 10ML InAs ($\mathrm{Be} : 1 \times 10^{17}$ cm^{-3})/10ML GaSb ($\mathrm{Be} : 5 \times 10^{16}$ cm^{-3}) SLs, which is intended to improve the carrier mobility, thus improving the minority carrier collection

efficiency and QE [13].The hole barrier was formed by alternating deposition of 6 ML AlSb and 12 ML n-doped InAs ($\mathrm{Si} : 1 \times 10^{16}\ \mathrm{cm}^{-3}$). The 200 nm thick top contact was an n-doped SL with 5 ML InAs ($\mathrm{Si} : 1 \times 10^{18}\ \mathrm{cm}^{-3}$)/5 ML GaSb and a 50 nm InAs ($\mathrm{Si} : 1 \times 10^{18}\ \mathrm{cm}^{-3}$) for better contact. One monolayer of InSb was inserted in each SL interface for strain compensation. A pin photodiode without hole barrier was grown on GaAs for reference.

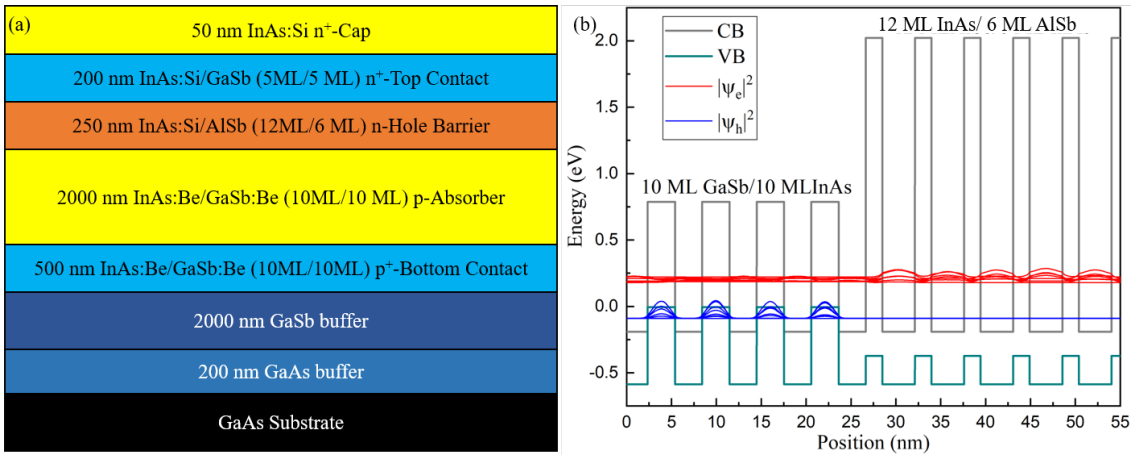

Figure 6.6: (a) Cross-sectional view of the T2SL barrier detector on GaAs substrates and (b) simulation of the an structure with 25 nm 10 ML GaSb/10 ML InAs and 30 nm 12 ML InAs/6 ML AlSb. CB and VB are the conduction band edge and valence band edge, respectively. $|\psi_\mathrm{e}|^2$ and $|\psi_\mathrm{h}|^2$ are the probability density for electrons and holes, respectively.

The simulated energy gap between of the 10 ML GaSb/10 ML InAs is about 248 meV ($\sim 5\ \mu\mathrm{m}$) for 77 K and the probability density of holes drops to zero in the 12 ML InAs/6 ML AlSb hole barrier region, as shown in Figure 6.6 (b). It is worth noting here that the simulation did not consider the effect of the additional InSb strain compensation layer and it assumes the SL interfaces are free of intermixing. Therefore, the measured energy gap of real device may vary from the simulated energy gap.

The as-grown nBp on GaAs was characterised by high-resolution XRD. The broadening of the rocking curve may be caused by defects that are present in the material, such as dislocations, mosaicity and curvature of the film. The TD density, ρ_{TD}, can be estimated

from the rocking curve by the following equation [14, 15],

$$\rho_{TD} = \frac{FWHM^2_{GaSb(004)}}{4.36 \times b^2} \tag{6.2}$$

where the $\mathrm{FWHM}_{\mathrm{GaSb(004)}}$ is the full width at half maximum value of the rocking curve, which is obtained by numerical fitting 0.05° or 8.7×10^{-4} rad, $b = (a/2)\sqrt{1+1}$ is the norm of the Burgers vector, which is 4.31×10^{-8} cm. The calculated defect density is about 9.3×10^7 cm^{-2}, which indicates the defects have been controlled effectively by using the IMF growth technique compared with the non-IMF growth mode ($\sim 10^{10}$ cm^{-2}).

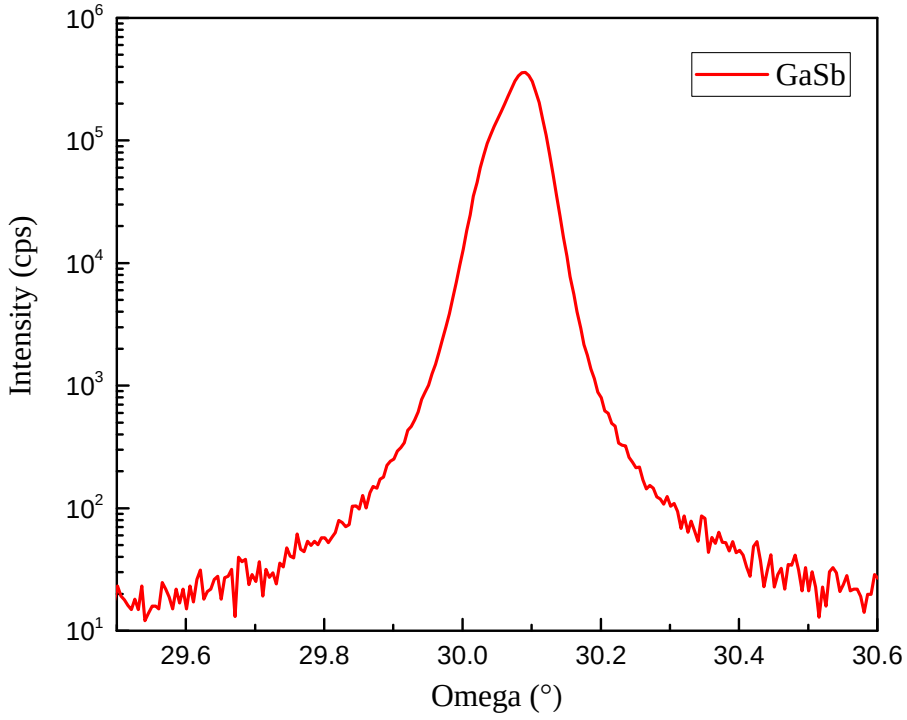

Figure 6.7: High-resolution XRD rocking curve of the nBp detector on GaAs substrate. The fitted FWHM of the rocking curve is 0.05°.

6.4 nBp Barrier Detector Device Characterisation

After material characterisation, the two samples (nBp and pin detectors) were processed into circular detector configurations for device measurements. The mesas were defined by standard photolithography and wet chemical etching. The solution for chemical etching was a mixture of citric acid:H_3PO_4:H_2O_2:H_2O with the volume ratio 1:1:4:16. The detector surface was passivated by SU-8, a polymer-based material, in order to suppress the surface leakage current. Ti/Pt/Au (50 nm/50 nm/300 nm) layers were deposited by an electron-beam evaporator on the top and bottom contacts for metallisation.

6.4.1 Dark Current

Following device fabrication, the nBp and p-i-n photodetectors were transferred to a low temperature probe station for dark current measurements. Dark current density-bias voltage characteristics measured from the T2SL devices at different temperatures are presented in Figure 6.8. The small photovoltaic shifts in the dark current curves for the nBp detector at 77 K and 100 K are due to the imperfections in the cold shield of the low temperature probe station; a similar phenomenon was pointed out and explained in chapter 5, section 5.4. At 77 K, the -0.1 V dark current densities are about 2.9×10^{-5} $\mathrm{A/cm^2}$ and 1.3 $\mathrm{A/cm^2}$ for nBp and p-i-n detectors, respectively. The -0.1 V dark current densities increase to 5.8 $\mathrm{A/cm^2}$ and 58.7 $\mathrm{A/cm^2}$ for the nBp and p-i-n detectors, respectively, at 300 K. The lower dark current in the nBp detector indicates that the barrier design is efficient in reducing the G-R current.

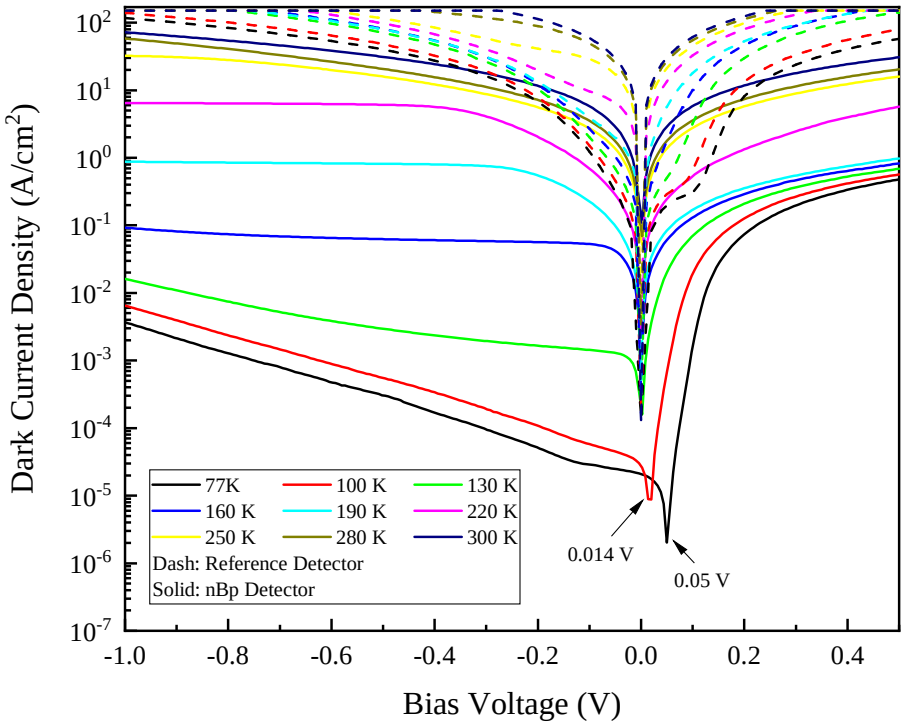

Figure 6.8: Temperature dependent dark current density-voltage characteristics of the nBp barrier detector (solid lines) and the p-i-n reference photodiode (dash lines).

The temperature dependent dark current densities of the nBp detector measured at -0.1 V have been plotted in Figure 6.9. The Arrhenius fit at low temperatures (77-130 K) shows a dark current activation energy of 61.6 meV, while at high temperatures the dark current activation energy increases to 159.8 meV. The energy gap of the T2SL detector various between $\sim$ 184 meV (77 K) and $\sim$ 159 meV (190 K), as estimated from the photoresponse spectra. At low temperatures, the activation energy is about the third of the energy gap, indicating that the dark current is dominated by G-R mechanisms, while at high temperatures, the dark current activation energy is about the same value as the T2SL energy gap, suggesting the device dark current is dominated by diffusion current.

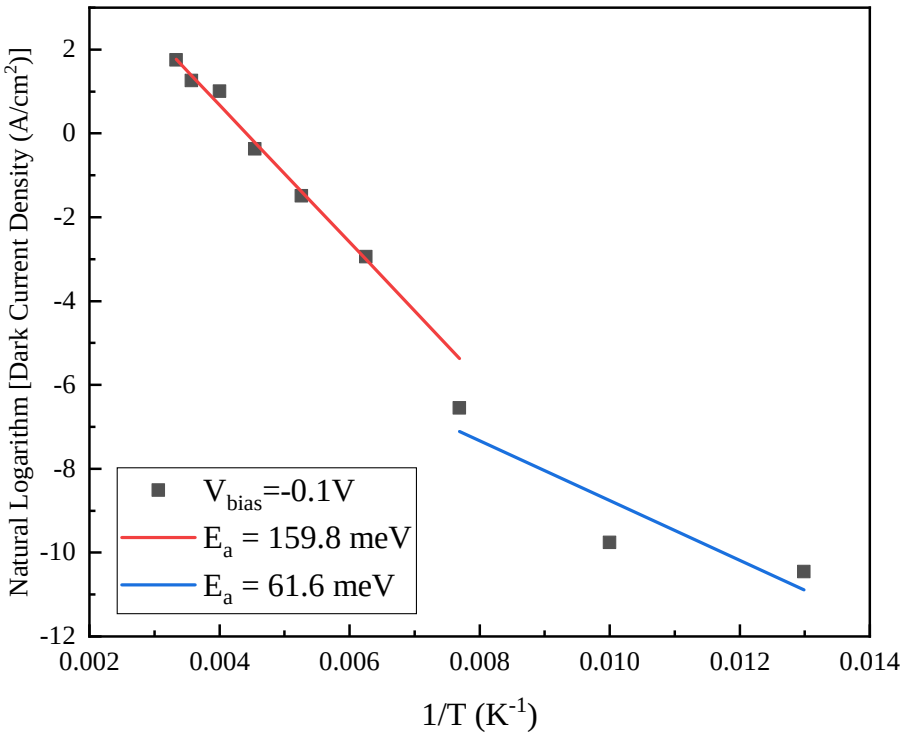

Figure 6.9: Natural logarithm dark current density measured at - 0.1 V as a function of the inverse temperature (1/T).

6.4.2 Photoresponse and Detectivity

The photoresponse spectra of the T2SL device measured at 0 V and different temperatures are shown in Figure 6.10. At 77 K, the 50% cutoff wavelength is about 6.4 μm, with a peak responsivity of 0.56 A/W. At 190 K, the cutoff wavelength extends to $\sim$ 7.3 μm and the peak responsivity drops to 0.35 A/W. The responsivity increases from 77 K to 130 K and drops from 130 K to 190 K. Similar temperature-responsivity relationships have been reported previously, for example in references [16] and [17]. One possible explanation is due to the temperature dependent diffusion length. At low temperatures, the mobility is governed by ionised impurity scattering ($\propto T^{1.5}$) [18], while at high temperatures, the mobility decreases as $\propto T^{-1.5}$ due to the phonon scattering and the carrier lifetime drops rapidly [16, 18]. Thus, the EQE is expected to increase with temperature from 77 K to

130 K due to increased collection efficiency. Another possible explanation is due to the presence of an unwanted electron barrier at the heterojunction interface [19]. When the temperature rises from 77 K to 130 K, the increased electron thermionic emission over the barrier increases the collection efficiency. A further increase of temperature from 130 K onwards leads to a rapid drop in responsivity, due to the decreased minority carrier lifetime as well as carrier mobility, thus, the EQE drops for the temperatures above 130 K.

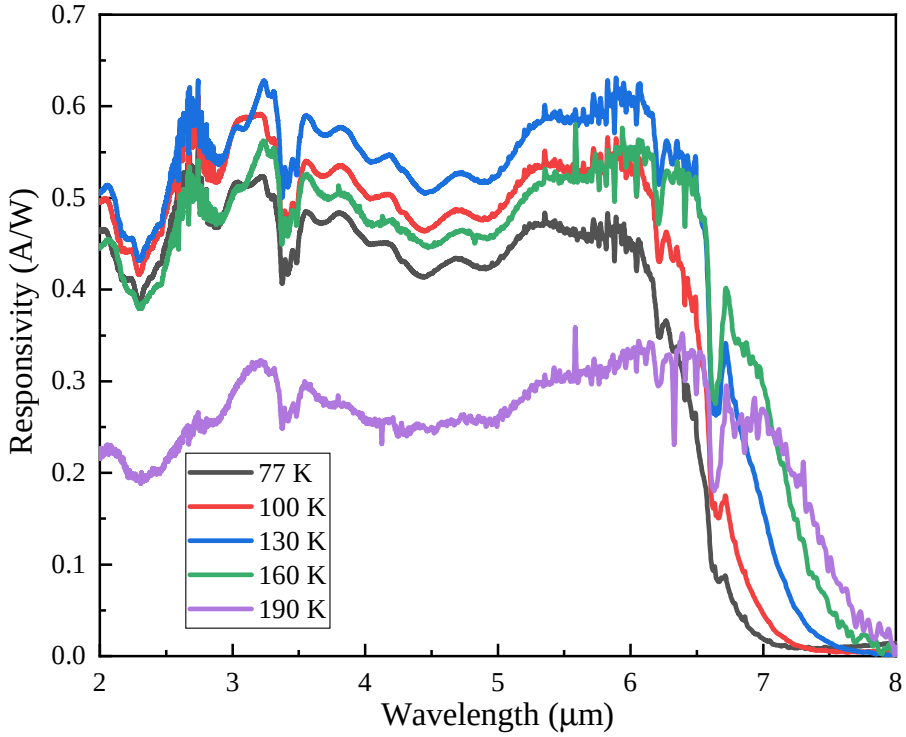

Figure 6.10: Temperature dependent photoresponsivity measurements of a nBp detector with the diameter of 130 μm.[1]

The response curves in Figure 6.10 exhibit complex behaviour. It seems very likely

[1]Figures 6.10 and 6.11 provide an overall indication of the photoresponse and detectivity and their variation with temperature. Absolute calibration is determined by the temperature and emissivity of the blackbody source, together with instrumental factors (optical transmission and geometry), according to equation 3.4. Measurements at different detector temperatures were conducted without change to the instrumental configuration..

that many of the features are associated with the device design and fabrication and should not be viewed as noise. It is notable that the intrinsic noise level observed in the mid-band is much smaller than the systematic fluctuations. Several different mechanisms are probably involved. For example, some of the variations in the 2-4 μm region may be attributable to internal optical reflections from semiconductor/air and semiconductor/semiconductor interfaces [20]. Optical absorption in the SU-8 encapsulation and in the InAs cap layer could also be contributing to the complex behaviour observed. The origin of the dip in response at 6.6 μm is not yet understood theoretically but appears to be a consistent feature, which is not visible in the 77K and 100K results because it lies beyond the cutoff wavelength at those temperatures. Instrumental or environmental factors cannot be ruled out, however, and further experimental work, as well as theoretical insights, will be needed in order to fully understand the results.

The Johnson-noise limited detectivity, D_J^*, of the nBp detector was calculated by equation [21],

$$D_J^* = R_i \sqrt{\frac{R_0 A}{4 k_B T}} \tag{6.3}$$

where $\mathrm{R_0A}$ is the differential resistance-area product under zero bias and R_i is the spectral current responsivity. The calculated specific detectivities for temperatures between 77 K and 190 K are shown in Figure 6.11. The detectivity decreases with temperature due to the rapid increase of thermal noise with temperature. At 77 K, a peak detectivity of $7.6 \times 10^{11} \mathrm{cm \cdot Hz^{1/2}/W}$ is achieved under zero bias. This value is about an order or magnitude higher than the corresponding value for a conventional p-i-n photodiode on GaAs [22], see Table 6.1 below. The detectivity improvement over the conventional p-i-n photodiode can be attributed to the approximately 3 orders of magnitude dark current reduction achieved by implementing the hole barrier. It is worth noting that despite the additional G-R dark current in the junction region, the dark current density is about twenty times lower than the dark current density of the self-passivated nBn detector on GaAs, as in Ref. [9]. This could be attributed to low defect density for III-Sb grown on GaAs

and the application of surface passivation. When compared with a similar nBp design on native GaSb substrates [23], the dark current is about an order or magnitude higher. Thus, future work should focus on optimisation of the III-Sb buffer layer for reducing the material defect density, e.g. optimising the IMF growth technique and using the SLSs dislocation filters.

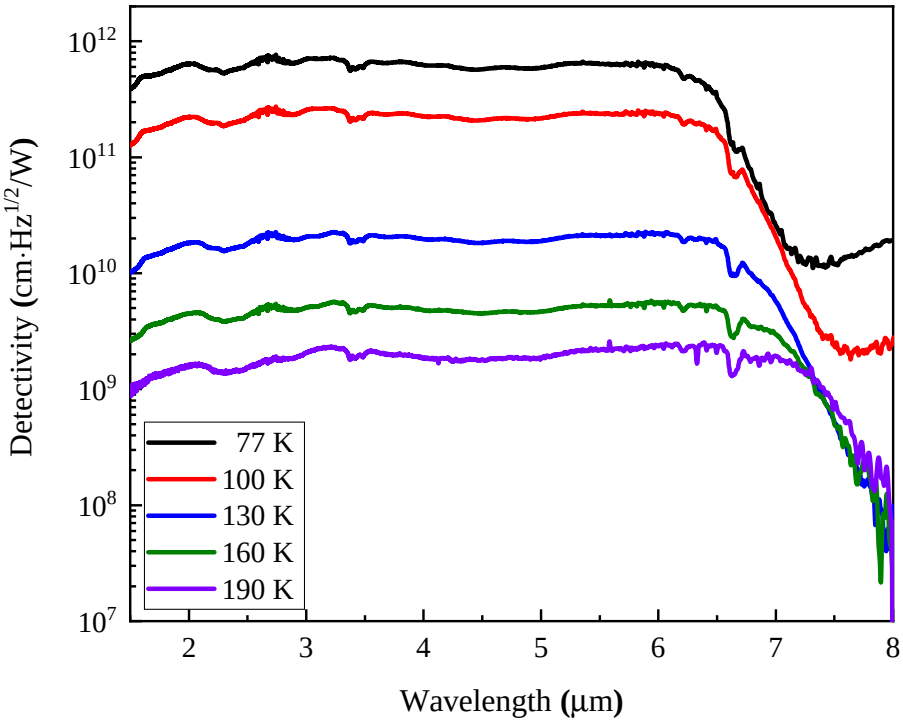

Figure 6.11: Johnson noise-limited detectivity of the nBp detector on GaAs measured at temperatures from 77 K to 190 K.

Table 6.1: Comparisons of the T2SL detectors grown on different substrates with various structural design at liquid nitrogen temperature. λ_{cutoff} is the cutoff wavelength, J_d is the dark current density, and D^* is the peak detectivity.

	nBp on GaAs [this work]	p-i-n on GaAs [22]	nBn on GaAs [9]	nBp on GaSb [23]
50% λ_{cutoff} (μm)	6.4	4.3	4.3 (0.5 V)	5 (0.2 V)
J_d (A/cm^2)	2.9×10^{-5}	1×10^{-2}	6×10^{-4}	4.5×10^{-6}
D^* ($cm \cdot Hz^{1/2}/W$)	7.6×10^{11}	2.3×10^{10}	1.2×10^{11}	-

6.5 Conclusion

In conclusion, T2SL photodetectors have been realised on GaAs and Si substrates. The quality of the materials was investigated by TEM and high resolution XRD. In order to reduce the dark current and increase the device performance, GaAs based nBp barrier detectors were demonstrated. The detector has a 50% cutoff wavelength at 6.4 μm (77 K). The dark current analysis shows a G-R limited dark current for temperatures below 130 K, and above 130 K, the dark current is dominated by the diffusion current. The peak detectivity at 77 K is 7.6×10^{11} cm $\cdot$ Hz$^{1/2}$/W, which is more than an order of magnitude higher than the published conventional p-i-n photodiode on GaAs. The nBp detector also shows an reduced dark current after comparing with the reference photodiode on GaAs. The improvement is due to the reduction of dark current with the nBp design. Future work could focus on optimising the III-Sb buffer layer, e.g. optimising the IMF growth condition and using strained SLs as DFLs, in order to compete with the T2SL detectors on the native GaSb substrates.

6.6 Contribution Statement

The InAs/GaSb nBp and p-i-n detectors were designed and grown by Dr. Jiang Wu, University College London, and Prof. Baile Chen, ShanghaiTech University. nBp detector dark Current and photocurrent measurements were provided by Dr. Zhuo Deng, ShanghaiTech University. TEM image was provided by Dr. Yuriy Mazur, University of Arkansas.

References

[1] J. B. Rodriguez *et al.*, "nBn structure based on InAs-GaSb type-II strained layer superlattices," *Applied Physics Letters*, vol. 91, no. 4, p. 043514, 2007.

[2] A. D. Hood, A. J. Evans, A. Ikhlassi, D. L. Lee, and W. E. Tennant, "LWIR Strained-Layer Superlattice Materials and Devices at Teledyne Imaging Sensors," *Journal of Electronic Materials*, vol. 39, no. 7, pp. 1001–1006, 2010.

[3] D. Z.-Y. Ting *et al.*, "A high-performance long wavelength superlattice complementary barrier infrared detector," *Applied Physics Letters*, vol. 95, no. 2, p. 023508, 2009.

[4] S. Maimon and G. W. Wicks, "nBn detector, an infrared detector with reduced dark current and higher operating temperature," *Applied Physics Letters*, vol. 89, no. 15, p. 151109, 2006.

[5] S. H. Huang *et al.*, "Strain relief by periodic misfit arrays for low defect density GaSb on GaAs," *Applied Physics Letters*, vol. 88, no. 13, p. 131911, 2006.

[6] Y. Kim, Y. Noh, M. Kim, J. Oh, and K. Chung, "Transmission electron microscopy study of the initial growth stage of GaSb grown on Si (001) substrate by molecular beam epitaxy method," *Thin Solid Films*, vol. 518, no. 8, pp. 2280–2284, 2010.

[7] Y. Wang, P. Ruterana, S. Kret, S. E. Kazzi, L. Desplanque, and X. Wallart, "The source of the threading dislocation in GaSb/GaAs hetero-structures and their propagation mechanism," *Applied Physics Letters*, vol. 102, no. 5, p. 052102, 2013.

[8] J.-H. Kim, T.-Y. Seong, N. J. Mason, and P. J. Walker, "Morphology and defect structures of GaSb islands on GaAs grown by metalorganic vapor phase epitaxy," *Journal of Electronic Materials*, vol. 27, no. 5, pp. 466–471, 1998.

[9] E. Plis *et al.*, "Mid-infrared InAs/GaSb strained layer superlattice detectors with nBn design grown on a GaAs substrate," *Semiconductor Science and Technology*, vol. 25, no. 8, p. 085010, 2010.

[10] Z. Deng *et al.*, "Demonstration of Si based InAs/GaSb type-II superlattice p-i-n photodetector," *Infrared Physics & Technology*, vol. 101, pp. 133–137, 2019.

[11] E. Delli *et al.*, "Mid-Infrared InAs/InAsSb Superlattice nBn Photodetector Monolithically Integrated onto Silicon," *ACS Photonics*, vol. 6, no. 2, pp. 538–544, 2019.

[12] A. Jallipalli *et al.*, "Structural analysis of highly relaxed GaSb grown on GaAs substrates with periodic interfacial array of 90° misfit dislocations," *Nanoscale Research Letters*, vol. 4, no. 12, pp. 1458–1462, 2009.

[13] D. Z. Ting *et al.*, "Antimonide-based barrier infrared detectors," in *Infrared Technology and Applications XXXVI* (B. F. Andresen, G. F. Fulop, and P. R. Norton, eds.), SPIE, 2010.

[14] J. Ayers, "The measurement of threading dislocation densities in semiconductor crystals by x-ray diffraction," *Journal of Crystal Growth*, vol. 135, no. 1-2, pp. 71–77, 1994.

[15] X. G. Zhang *et al.*, "Comparison of x-ray diffraction methods for determination

of the critical layer thickness for dislocation multiplication," *Journal of Electronic Materials*, vol. 28, no. 5, pp. 553–558, 1999.

[16] L. Höglund *et al.*, "Manufacturability of type-II InAs/GaSb superlattice detectors for infrared imaging," *Infrared Physics & Technology*, vol. 84, pp. 28–32, 2017.

[17] D. Z. Ting *et al.*, "Mid-wavelength high operating temperature barrier infrared detector and focal plane array," *Applied Physics Letters*, vol. 113, no. 2, p. 021101, 2018.

[18] S. Sze and K. K. Ng, *Physics of Semiconductor Devices*. John Wiley & Sons, Inc., 2006.

[19] P. Klipstein, ""XB n " barrier photodetectors for high sensitivity and high operating temperature infrared sensors," in *Infrared Technology and Applications XXXIV* (B. F. Andresen, G. F. Fulop, and P. R. Norton, eds.), SPIE, 2008.

[20] B.-M. Nguyen *et al.*, "Demonstration of midinfrared type-II InAs/GaSb superlattice photodiodes grown on GaAs substrate," *Applied Physics Letters*, vol. 94, no. 22, p. 223506, 2009.

[21] J. Liu *et al.*, "High resistance AlGaAs/GaAs quantum cascade detectors grown by solid source molecular beam epitaxy operating above liquid nitrogen temperature," *Semiconductor Science and Technology*, vol. 25, no. 7, p. 075011, 2010.

[22] M. Korkmaz *et al.*, "Performance evaluation of InAs/GaSb superlattice photodetector grown on GaAs substrate using AlSb interfacial misfit array," *Semiconductor Science and Technology*, vol. 33, no. 3, p. 035002, 2018.

[23] A. Kazemi *et al.*, "Mid-wavelength infrared unipolar nBp superlattice photodetector," *Infrared Physics & Technology*, vol. 88, pp. 114–118, 2018.

Chapter 7

Summary and Future Work

7.1 Summary

The use of Si substrates provides a way to address the high cost and size limitations of lattice-matched or native substrates for growing III-V infrared photodetectors. Furthermore, direct growth of infrared photodetectors on Si substrates can help to resolve the thermal expansion mismatch problem associated with hybridised sensor chip assemblies, whilst the monolithic integration of infrared photodetectors on to CMOS compatible Si substrates can potentially take advantage of the CMOS foundry for high-volume and low-cost Si readout integrated circuits and photonic integrated circuit manufacturing. Despite the promising benefits offered by the Si substrates, the large dissimilarities between the III-V compounds and Si can cause defects to be generated at the heteroepitaxy interface and in the succeeding epitaxial layers, which are detrimental to the device performance. Several methods have been utilised to minimise the material defects and reduce the impact of material defects on the device performance.

On the material growth aspect, Si (001) substrates with 4° offcut towards the [01-1] direction can be employed to eliminate the formation of APDs, which form during the polar to non-polar epitaxy. SLSs DFLs were used to accelerate the movement and

the self-annihilation of the TDs, which can reduce the requirement of a thick buffer to achieve low TD density, while the IMF growth technique helped the growth of the Sb-based compounds on Si with low TD density by generating less harmful 90° MDs at the heteroepitaxy interface. The material quality has received a considerable improvement with the help of the III-V buffer techniques and has been characterised by TEM and XRD. For example, the TEM analysis in chapter 4 reveals that the TD density is reduced by about 4 orders of magnitude to the level of $\sim 10^6\ \mathrm{cm}^{-2}$.

On the device design aspect, chapter 4 presents the proof of concept of the buffer technology and the direct growth of quantum structured infrared photodetectors on Si substrates. QDIPs are expected to have better defect tolerance than QWIPs and bulk detectors, owing to the strong carrier localisation in the QDs. Time-resolved PL studies show that the PL lifetimes of the QDIPs on Si were comparable to the QDIPs grown on native GaAs substrates. The QDIPs on Si exhibit two colour photoresponse at 80 K in the MWIR and LWIR bands. Phonon-assisted tunnelling and thermionic emission are the main dark current generation mechanisms for the InGaAs QDIPs on Si operating at low and high temperatures, respectively. The demonstration of QDIPs on Si at liquid nitrogen temperature has shown their capability to cope with the high defect density environment.

In order to improve the noise performance of photodetectors on Si, infrared photodetectors employing a quantum cascade design have been explored. For QCDs operating in photovoltaic mode, the internal device noise source is limited to the Johnson noise. Chapter 5 compares SML QD QCDs on native GaAs substrates and Si substrates. Both the QCD-GaAs and QCD-Si operate successfully at 160 K. The 77K responsivity curves of the two detectors are nearly identical, indicating the SML QCD structure is able to mitigate the impact of defects on photocurrent. The incorporation of SML QD absorbers into the QCD provides a low thermionic emission rate and normal incidence operation. The $\mathrm{R_0A}$ value of the QCD-GaAs is about 3 orders of magnitude higher than the QCD-Si at 77 K, meaning the QCD-GaAs has a lower Johnson noise. By fitting the temperature

dependent R_0A values with the Arrhenius equation, the low R_0A value in the QCD-Si is attributed to the lower activation energy of an unwanted diagonal transition. A suggestion has been given in the chapter to improve the detectivity of QCD-Si.

Even though the QDIPs and SML QD QCD on Si substrates have been successfully demonstrated at an operating temperature of 77 K or above, infrared photodetectors using QDs or SML QDs as the absorber still face the limitation of low QE. Chapter 6 studies Sb-based T2SL photodetectors on foreign Si and GaAs substrates. The Sb-based T2SL is a versatile material system and detectors that have been made from T2SL absorbers had a better reported QE than with the QD absorber. T2SL p-i-n photodiodes on Si and GaAs are first studied in chapter 6. High values of dark current are observed in both photodiodes, which may be due to the G-R current in the depletion region and surface current. Chapter 6 then discusses surface-passivated nBp barrier detectors on GaAs substrates in order to suppress the surface current and G-R current. The insertion of a large bandgap barrier in between the heavily n-doped SLs and p-absorber is helpful to reduce the G-R current. At temperatures between 80 K and 130 K, the dark current is determined by the G-R current, and for the temperatures above 130 K, the detector shows diffusion limited dark current performance. In comparison with the previously published results, the nBp on GaAs shows a better dark current performance than MWIR T2SL photodiodes on GaAs and nBn on GaAs at liquid nitrogen temperature. The dark current performance of the nBp detector is also better than the reference p-i-n photodiode on GaAs at all temperatures, which shows the nBp structure is able to reduce the impact of defects on dark current. As expected, the dark current value is still 15 times higher than the similar nBp on GaSb substrate, meaning that the presence of high defect density is an important factor that is limiting the device performance.

Table 7.1 summarises the key information of the experimental sections. The detectivity of the QDIP on Si was not obtained due to the capability of the experimental setup. Within the obtained results, nBp on GaAs has higher device performance than the two

QCDs.

Table 7.1: Summary of the experimental sections. Est. TDD = Estimated Threading Dislocation Density, LN = Liquid Nitrogen, Max. Temp = Maximum Operating Temperature.

		LN Temperature		
	Est. TDD	λ_P	D^*_{max}	Max. Temp
	(cm^{-2})	(μm)	($\mathrm{cm} \cdot \mathrm{Hz}^{1/2}/\mathrm{W}$)	(Bias)
QDIP on Si	$\sim 10^6$(TEM)	6.1	N/A	80 K (>0.05V)
QCD on GaAs	Homoepitaxy	6.1 and 6.5	1.06×10^{11}	160 K (0V)
QCD on Si	3×10^7(TEM)	6.1 and 6.5	3.83×10^9	160 K (0V)
nBp on GaAs	9.3×10^7(XRD)	6.4(50%cutoff)	7.6×10^{11}	190 K (0V)

Since this work only explored a small number of potential candidates, apart from optimising the current designs, it may be anticipated that more designs will be proposed in the future. For example, Ga-free nBn designs, which will be suggested in the next section, may also have a good defect tolerance characteristic.

In conclusion, this thesis aims to use III-V quantum structured infrared photodetector designs to have high defect tolerance that can sustain the high defect density generated by III-V on Si epitaxy. The QDIPs and SML QD QCD have shown good defect tolerance characteristics. The nBp barrier detector has demonstrated its designed dark current reduction characteristics. Although, at present, the photodetectors on foreign substrates do not perform as well as the photodetectors on native or lattice-matched substrates, it is plausible that further improvements can be achieved by optimising device design. I believe this thesis will bring useful insights to the future development of low-cost infrared detectors and imagers for civil applications.

7.2 Future Work

7.2.1 Surface Plasmons

The QD based infrared detectors demonstrated previously have generally suffered from low absorption coefficients. This could be partially attributed to the low dot areal density and wide dot size distribution associated with the QD fabrication methods. Improving the uniformity and density of the QDs will improve the absorption QE. Further performance improvement can be obtained through the application of surface plasmons. Surface plasmons are resonantly excited by the interaction of incident electromagnetic field with the free electrons at metal/dielectric interface [1]. Metallic 2D subwavelength hole/polygon arrays are commonly used surface plasmonic structures. The transmission efficient can exceed one at selected wavelength after normalising to the area occupied by the holes [2] and experimental verifications have shown that the photoresponsivity can be increased by a factor of several in QDIPs with surface plasmonic structures [3, 4]. Based on the QD based detectors shown in chapter 4 and chapter 5, surface plasmonic design should focus on matching the transmission spectrum and the detector's absorption spectrum, maximizing the transmission efficient, and maximizing the interaction between the QD region and the surface plasmonic field [3].

7.2.2 nBp Barrier Detector Growth and Simulation Optimisations

As mentioned in the chapter 6, there is a big difference between the calculated energy gap (248 meV, 77 K) and measured energy gap (193 meV, 77 K) for the 10 ML InAs/ 10 ML GaSb SL absorber. This difference could be attributed to the combination of low SL quality and the omission of some practical details, such as the InSb strain compensation layer, in the simulation. It is important for heterojunction detectors to have consistency between the simulation and measurement results as, if not, it can lead to unwanted band offset, which could result in inefficient collection efficiency. Future work should involve

both growth and simulation optimisations.

7.2.3 Ga-free T2SL Barrier Detectors

For T2SL based infrared photodetectors on Si, the InAs/InAsSb SLs nBn detector on Si recently demonstrated by researchers from Lancaster University and Coventry University has shown a promising result in the development of Si based infrared detectors, offering the prospect of higher operating temperature [5]. This Ga-free InAs/InAsSb SLs material not only offers an improved minority carrier lifetime, but it is also less sensitive to material defects [6, 7]. The downside of the Ga-free T2SL barrier detectors is that they are generally lower in QE, which may be attributed to the low absorption coefficient and the lack of hole barrier material for minority electron operation [7, 8]. Investigation of thermoelectrically cooled InAs/InAsSb SLs nBn detectors on Si substrates would be an interesting new device design in the future.

7.2.4 CMOS Compatible Si (001) Substrates

In this thesis, we use the Si (001) substrates with 4° offcut towards the [01-1] direction to avoid the antiphase disorder. Substrates with such high degree of intentional offcut angle are incompatible with the CMOS manufacturing processes [9]. In order to take the benefits of the low-cost and high-volume production of the CMOS industry for making the Si based readout circuitry as well as realising the mid-infrared photonic circuits on Si platform, growing infrared detectors on nominal Si (001) substrates is essential. In recent years, several groups have successfully demonstrated APD free near-infrared III-V lasers and detectors on CMOS compatible Si substrates, for example GaAs on patterned Si [10], GaP on Si [11], and GaAs on Si [12]. Although some problems still exist, such as the Si substrate generally requiring a high temperature treatment before epitaxy, these pioneering works are encouraging. Future work could focus on transferring the existing

device structures from offcut Si (001) substrates to the on-axis Si (001) substrates.

References

[1] C. Genet and T. W. Ebbesen, "Light in tiny holes," *Nature*, vol. 445, no. 7123, pp. 39–46, 2007.

[2] H. F. Ghaemi, T. Thio, D. E. Grupp, T. W. Ebbesen, and H. J. Lezec, "Surface plasmons enhance optical transmission through subwavelength holes," *Physical Review B*, vol. 58, no. 11, pp. 6779–6782, 1998.

[3] C.-C. Chang, Y. D. Sharma, Y.-S. Kim, J. A. Bur, R. V. Shenoi, S. Krishna, D. Huang, and S.-Y. Lin, "A surface plasmon enhanced infrared photodetector based on InAs quantum dots," *Nano Letters*, vol. 10, pp. 1704–1709, may 2010.

[4] G. Gu, N. Mojaverian, J. Vaillancourt, and X. Lu, "Surface plasmonic resonance induced near-field vectors and their contribution to quantum dot infrared photodetector enhancement," *Journal of Physics D: Applied Physics*, vol. 47, no. 43, p. 435106, 2014.

[5] E. Delli *et al.*, "Mid-infrared InAs/InAsSb superlattice nBn photodetector monolithically integrated onto silicon," *ACS Photonics*, vol. 6, no. 2, pp. 538–544, 2019.

[6] D. Z. Ting *et al.*, "Mid-wavelength high operating temperature barrier infrared detector and focal plane array," *Applied Physics Letters*, vol. 113, no. 2, p. 021101, 2018.

[7] T. Schuler-Sandy *et al.*, "Gallium free type-II $\mathrm{InAs/InAs_xSb_{1-x}}$ superlattice photodetectors," *Applied Physics Letters*, vol. 101, no. 7, p. 071111, 2012.

[8] P. C. Klipstein *et al.*, "Modeling InAs/GaSb and InAs/InAsSb superlattice infrared detectors," *Journal of Electronic Materials*, vol. 43, no. 8, pp. 2984–2990, 2014.

[9] A. Ren, L. Yuan, H. Xu, J. Wu, and Z. Wang, "Recent progress of III-V quantum dot infrared photodetectors on silicon," *Journal of Materials Chemistry C*, 2019.

[10] Y. Wan *et al.*, "Optically pumped 1.3 μm room-temperature InAs quantum-dot micro-disk lasers directly grown on (001) silicon," *Optics Letters*, vol. 41, no. 7, p. 1664, 2016.

[11] A. Y. Liu *et al.*, "Electrically pumped continuous-wave 1.3 μm quantum-dot lasers epitaxially grown on on-axis (001) GaP/Si," *Optics Letters*, vol. 42, no. 2, p. 338, 2017.

[12] S. Chen *et al.*, "Electrically pumped continuous-wave 1.3 μm InAs/GaAs quantum dot lasers monolithically grown on on-axis Si (001) substrates," *Optics Express*, vol. 25, no. 5, p. 4632, 2017.